SAND REPORT

SAND2004-1118
Unlimited Release
Printed March 2004

Determination of Critical Length Scales for Corrosion Processes using Microelectroanalytical Techniques

Kevin R. Zavadil and Frederick D. Wall

Prepared by
Sandia National Laboratories
Albuquerque, New Mexico 87185 and Livermore, California 94550

Sandia is a multiprogram laboratory operated by Sandia Corporation,
a Lockheed Martin Company, for the United States Department of Energy's
National Nuclear Security Administration under Contract DE-AC04-94-AL85000.

Issued by Sandia National Laboratories, operated for the United States Department of Energy by Sandia Corporation.

Available to DOE and DOE contractors from
U.S. Department of Energy
Office of Scientific and Technical Information
P.O. Box 62
Oak Ridge, TN 37831

Telephone: (865)576-8401
Facsimile: (865)576-5728
E-Mail: reports@adonis.osti.gov
Online ordering: http://www.doe.gov/bridge

Available to the public from
U.S. Department of Commerce
National Technical Information Service
5285 Port Royal Rd
Springfield, VA 22161

Telephone: (800)553-6847
Facsimile: (703)605-6900
E-Mail: orders@ntis.fedworld.gov
Online order: http://www.ntis.gov/help/ordermethods.asp?loc=7-4-0#online

SAND2004-1118
Unlimited Release
Printed March 2004

Determination of Critical Length Scales for Corrosion Processes using Microelectroanalytical Techniques

Kevin R. Zavadil and Frederick D. Wall
Corrosion & Surface Sciences

Sandia National Laboratories
P.O. Box 5800
Albuquerque, New Mexico 87185-0888

Abstract

A key factor in our ability to produce and predict the stability of metal-based macro- to nano-scale structures and devices is a fundamental understanding of the localized nature of corrosion. Corrosion processes where physical dimensions become critical in the degradation process include localized corrosion initiation in passivated metals, micro-galvanic interactions in metal alloys, and localized corrosion in structurally complex materials like nanocrystalline metal films under atmospheric and inundated conditions. This project focuses on two areas of corrosion science where a fundamental understanding of processes occurring at critical dimensions is not currently available. Sandia will study the critical length scales necessary for passive film breakdown in the inundated aluminum (Al) system and the chemical processes and transport in ultra-thin water films relevant to the atmospheric corrosion of nanocrystalline tungsten (W) films. Techniques are required that provide spatial information without significantly perturbing or masking the underlying relationships. Al passive film breakdown is governed by the relationship between area of the film sampled and its defect structure. We will combine low current measurements with microelectrodes to study the size scale required to observe a single initiation event and record electrochemical breakdown events. The resulting quantitative measure of stability will be correlated with metal grain size, secondary phase size and distribution to understand which metal properties control stability at the macro- and nano-scale. Mechanisms of atmospheric corrosion on W are dependent on the physical dimensions and continuity of adsorbed water layers as well as the chemical reactions that take place in this layer. We will combine electrochemical and scanning probe microscopic techniques to monitor the chemistry and resulting material transport in these thin surface layers. A description of the length scales responsible for driving the corrosion of the nanocrystalline metal films will be developed. The techniques developed and information derived from this work will be used to understand and predict degradation processes in microelectronic and microsystem devices critical to Sandia's mission.

Section A:
Critical Length Scales and Chemical Processes in the Corrosion Mechanism of Two Passive Metals as Nanocrystalline Thin Films

A1.0 Introduction

A growing interest exists in incorporating new materials into microelectronic and microsystem platforms. Functional devices that can be integrated into sensing, microfluidic, and biotechnological applications, as examples, require greater flexibility in the materials used for the various structural and active components. Low temperature deposition techniques including reactive sputtering, chemical vapor deposition (CVD) and atomic layer deposition (ALD) offer potential routes for tuning the electrical, compositional, mechanical (stress state), tribological (hardness and wear resistance) properties within a given materials system and within specific dimensional constraints that conform to device design. An understanding of the stability of these materials is essential in order to guarantee eventual device reliability.

Tungsten represents a particularly good example of a material whose composition and properties can be tailored for a wide range of applications. Chemical vapor deposition has long been used for W deposition in CMOS technology. Early efforts in CVD W chemistry led to a demonstrated ability to generate self-limiting, thin films of W directly on Si (A1,A2). This approach, termed selective CVD deposition, demonstrated that W could be intrinsically patterned using preferential or selective deposition on Si, as opposed to SiO_2 or Si_3N_4 regions. Sandia developed this deposition technology, in part, for the non-line-of-sight and conformal coating of polycrystalline Si surfaces in microelectromechanical (MEMS) devices (A3). More recently, processes have been worked out to conduct lower temperature, sequential CVD reactions termed atomic layer deposition (ALD) (A4). Like the selective CVD chemistry, ALD is a non-line-of-sight approach but is not limited in terms of the thickness of the deposit layer. The ultrathin dimensions of these films lead to nanocrystalline structure while reduction in deposition temperature produce structures approaching the amorphous state. These types of W films are one material of choice for controlling the surface termination in Si-based MEMS devices.

A minimal amount of work has been reported to date on the corrosion properties of these films (A5). Corrosion becomes a potential concern in MEMS devices where closed spaced geometries and potentially high relative humidity atmospheres could lead to capillary condensation of water at a W terminated surface. In this report, we describe initial efforts to understand how water interacts with Sandia developed selective CVD W films on Si. We compare the behavior of selective films with true metallic W films produced at Sandia using standard CMOS technology. An electrochemical scanning force microscope has been used in conjunction with electrochemical and surface spectroscopic techniques to develop an understanding of the critical length scales that define film stability. We demonstrate that this concept of a critical length scale for corrosion in nanocrystalline W films relates to structural heterogeneity in the selective films and wetting dynamics for condensed water layers in the metallic W films. As a further study of the extent of our current ability to determine a critical length scale, we include a description of void-to-pore transitions in the nanocrystalline Al system as measured by surface force microscopy.

A2.0 Deposition of Nanocrystalline Tungsten Films

The deposition process for selective CVD W films has been previously described (A3). The chemistry is an interfacially mediated solid state reduction of WF_6 to form W^0 and the oxidation of the substrate Si to form either volatile silicon difluoride or silicon tetrafluoride. Deposition is typically conducted at 450ºC and preceded by a vapor phase NF_3 removal of any residual oxide. This cleaning step has also been identified as essential in producing a uniform, conformal and adherent W film. The substrates used in this study were Si(100) wafers used as process monitor substrates for the Genus 8720 system described by Mani et al. (A3). The resulting film thickness have been determined using Rutherford Back Scattering (RBS) by Mani and Transmission Electron Microscopy (TEM by Headley and Kotula for deposition on both Si(100) and polycrystalline Si used in the SUMMiT process (A3,A6).

The deposition CVD W films is essentially a variant of standard CMOS based processes. Deposition of 10 to 100 nm was carried out in an Applied Materials (AMAT) WxZ chamber mounted on an AMAT Centura 5200 platform. CVD tungsten films were produced at 450°C by flowing a 1:1 ratio of WF_6 to SiH_4 at a pressure of 4.5 torr. Films were deposited on top of 150 mm diameter Si wafers (MEMC) that were 670 μm thick with a 50 nm coating of TiN deposited in an Endura PVD tool (AMAT) via DC magnetron reactive sputtering from a Ti target in the poisoned mode. W film thickness control was achieved by adjusting the deposition time to obtain the desired thickness based on a deposition rate of 2.2 $nm \cdot s^{-1}$. This rate was determined via least squares fit of SEM cross-section and deposition time data obtained over a range of 35 to 150 nm.

A3.0 Corrosion of Nanocrystalline Metallic Tungsten Films

Corrosion is an expected consequence for tungsten when exposed to both H_2O and O_2 (A7-A9). The net electrochemical equations for W oxidation and O_2 reduction are as follows:

$W + 8OH^- \rightarrow WO_4^{2-} + 4H_2O + 6e^-$	anodic reaction	(A1)
$O_2 + 2H_2O + 4e^- \rightarrow 4OH^-$	cathodic reaction	(A2)
$2W + 3O_2 + 4OH^- \rightarrow 2WO_4^{2-} + 2H_2O$	net reaction	(A3)

This electrochemical instability is primarily driven by the instability of a passive film at near neutral pH. The passive oxide WO_3 becomes soluble at a pH of approximately 4.6 assuming a micromolar quantity is sufficient to define an acceptable dissolution rate within the system of interest. Corrosion rates have been measured for bulk W using electrochemical linear polarization techniques at high basic pH (A10). Phosphate solutions have traditionally been used for these studies to avoid the effects of surface complexes as intermediates in the dissolution kinetics (A11-A13). Data from these studies can be used as a starting point for estimating expected rates and lifetimes for thin W films. An example is shown in Figure A1 where published data has been analyzed in a Tafel format to extract the exchange current density dependence on pH and temperature. This analysis shows that rates within the 3 to 4 $nm \cdot hr^{-1}$ range would be expected for film immersion. At issue is whether these values are valid for nanocrystalline films. In addition, we need to measure these values in solution in order to understand what an upper limit might be for H_2O condensed on the W surface.

Corrosion rates in an inundated aqueous environment can be measured directly using impedance techniques. For thin films, this measurement simplifies to a breakthrough type of experiment. The thin film will exhibit a characteristic impedance and phase angle at sufficiently low frequency that is dependent on the kinetics of the reactions (equations A1 and A2) that define its open circuit potential. These values are different for the substrate material. The thin film can therefore be allowed to corrode through to the substrate producing a characteristic change in these values. An example of a sputter deposited 7 nm thick W film is shown in Figure A2a. This figure shows the characteristic time-dependence of the impedance and phase angle as the film undergoes uniform corrosion in an oxygenated 50 mM phosphate electrolyte at neutral pH. The impedance at 10 mHz is constant at 2 kΩ for 2000 seconds after which it starts to rise to a new limiting value of 500 kΩ. The phase angle decreases (current lags excitation potential) in tandem with this impedance rise from an initial value of near 0º to a final value of 20º. This sharp transition signals a uniform breakthrough of the film. The higher impedance and lagging current response with respect to the 10 mV excitation potential used are indicative of the underlying Si substrate with kinetics now controlled by its passive oxide. We note that the presence of a thermal oxide below the sputtered W film (vs. W deposited onto H-terminated Si(100)) has minimal effect on the time required to fully penetrate the film and only moderate effects on the final impedance and phase angle values. The fact this breakthrough occurs in a uniform fashion was confirmed using scanning Auger electron spectroscopy and AFM to establish the lack of significant remnant tungsten on the solution exposed surface. From this experiment, we find that corrosion rates for nanocrystalline W films can be as high as 13 $nm \cdot hr^{-1}$ with aqueous immersion. This value is a factor of four larger than the extrapolated value expected for bulk W and appears to contain the effects of the deposition technique.

The corrosion rate for a metallic CVD derived W film is measured to be substantially slower than that of sputtered films. Figure A2b shows the time profiles for a 10 nm thick film for the same electrolyte, pH, temperature and O_2 content. The same initial material system dictates comparable initial values for impedance and phase angle with respect to sputtered W and this is what is observed. Final values for this CVD film are different because they are defined by a TiN barrier layer as opposed to Si. The impedance and phase angle transitions occur at $2x10^4$ seconds signaling the corrosion rate of 1.7 $nm \cdot hr^{-1}$. This value is slightly less than the 2 to 3 $nm \cdot hr^{-1}$ rate based on extrapolated bulk corrosion rates and is approximately an order of magnitude lower than the rate of the sputtered film. We measure comparable values for 0.5, 5, and 50 mM solutions of PO_4^{4-}, BO_3^{3-} and WO_4^{2-} indicating that potential anion effects in solution (anion-surface interactions) are not a dominant determinant of corrosion rate. However, we note that significant variation in corrosion rate has been observed for a single anion and concentration for multiple CVD W samples from a given wafer. What is learned form these results is that corrosion proceeding at an appreciable rate is a potential process even under atmospheric conditions, where dissolution will lead to WO_4^{2-} as the predominant anion present in the surface water layers.

The origin of this difference in corrosion rate for sputtered and CVD films is most likely a combination of differences in grain size and possible stress state of the film. We can rule out compositional effects or errors in actual film thickness because time-of-flight mass spectrometry (TOF-SIMS) was used to characterize both types of films. The

relative thickness difference was confirmed using SIMS in a sputter depth profiling mode. No measurable secondary constituents (i.e. Si in the CVD W) at levels of 0.01 atomic percent were identified confirming their compositional similarity. This leaves the possibility of either grain size or possibly stress state of the W film as the source of the rate difference. Contact mode AFM measurements showed a smaller grain size for the sputtered films on average the size of the film thickness or 7 nm in diameter while the CVD W possess a slightly larger average grain size in the 20 nm range. The CVD W also shows a characteristics low density of large diameter grains that extend nominally 4 nm above the mean plane of the surface. The CVD deposition was conducted at 450ºC while sputter deposition was completed on an unheated Si substrate allowing for a greater degree of stress relaxation in the CVD case.

A4.0 Stability and Related Corrosion Processes for Selective CVD Tungsten Deposited on Silicon

The initial stability of selective W films is dictated by dissolution kinetics of the film in condensed water layer. This sensitivity to dissolution is driven by the fact that the as-deposited film is not a metallic film but instead a tungsten oxynitride film. This finding was originally alluded to in the TEM work of Headley and Kotula (A6) and the x-ray photoelectron spectroscopic (XPS) work of Dugger and Peebles (A14). Energy filtered electron energy loss measurements conducted on a TEM showed both N and O distributed throughout the 10 and 20 nm thick films deposited on polycrystalline Si and Si(100), respectively (A6). Dugger and Peebles conducted X-ray Photoelectron Spectroscopy on freshly deposited films and tracked compositional changes over a 14 day period (A14). Their results showed a complete absence of detected metallic tungsten based on the W(4f) transition. Given the energy of these photoelectrons and electron scattering models, the depth from which this information is being obtained can be estimate to be approximately 9 nm or 90% of the film thickness for thinner deposits on Si(100).

Our measurements confirm the lack of metallic W in these films. Figure A3 shows a comparison of W(4f) photoelectron emission for an as-deposited 10 nm thick selective W film on Si(100) and an as-deposited 10 nm thick metallic CVD CMOS W film on TiN. The W(4f) lineshape is comprised of two discrete emission features owing to spin orbit splitting of the 4f electrons – a lower binding energy $4f_{7/2}$ and a higher binding energy $4f_{5/2}$. Multiple valence states of W will each exhibit these two peaks, but they will be shifted in binding energy based on the degree to which the valence charge alters the coulombic screening of the 4f electrons. Higher valence cations of +4 or +6 charge will exhibit higher binding energy 4f peaks relative to the metallic W atoms. This effect of multiple, energy shifted peaks is shown by the dashed traces of Figure 3A that arise from a film comprised of 40% metallic W (W^0), 15% WN_x or WO_2 (W^{4+}) and 45% WO_3 (W^{6+}). The spectra in Figure A3 show that the principle forms of W in the selective film are W^{6+} presumably as WO_3 and W^{4+} as either WN_x, WO_2 or as an oxynitride. A mixed valence oxide with W^{5+} is also a possibility, but XPS as applied in this study is not capable of resolving its presence. These results contrast with the metallic CVD derived W film deposited at a comparable temperature (450ºC) using SiH_4 as a reducing agent onto a sputtered TiN barrier layer. Figure A3 shows that the film is predominantly composed of metallic W with an approximate 1 nm thick WO_3 layer on its surface. These films were

analyzed at comparable times (several weeks) after deposition with storage under dry conditions to allow for a fair comparison.

The lack of metallic W observed by Dugger and Peebles for films analyzed within hours after deposition clearly indicates that the source of N is the deposition process itself (A14). We postulate that N arises from the NF_3 used to clean the Si surface prior to deposition and that has been identified as critical to the nucleation and subsequent growth of the self-limiting W film. Atomic N present during deposition would be reactive toward W. Atomic N would also be expected to undergo recombinant desorption on the deposition chamber walls forming N_2. However, di-atomic nitrogen could still serve as a N source for these films because N_2 is known to dissociate on W below the 450ºC temperature used to deposit the selective film (A15). We also note that these W films have an ability to slowing uptake O from the ambient atmosphere, an effect that shows up to a much lesser extent in the reported work of Dugger and Peebles. We have found that longer periods of storage (months) show larger relative O and W^{6+} content and decreased N and W^{4+} content. Exposure of the film to selective oxidants like O_3 using an ultraviolet source will also increase O and reduce N content in the film.

Our focus on the corrosion properties of selective W then begin with the recognition that this film is actually an oxynitride. It is the oxide sub-phase in this material that is subject to degradation. This effect can be seen by comparing photoemission data from air aged films versus those that have been immersed for long periods of time in de-ionized water or very short periods in 1M KOH. Figure A4 shows the impact of aqueous immersion on the chemical state of tungsten in the film. Increased water immersion time leads to an increase in the relative W^{4+} intensity. Exposure to a highly basic solution produces a comparable effect on a much shorter time frame. As discussed previously, the solid oxide phases of W should undergo dissolution with stability of the solid phase decreasing with increasing pH. The long term effects of water exposure are more clearly delineated in the relative composition versus immersion time plot of Figure A5. We find that a relatively rapid selective dissolution of oxide takes place with water immersion leading to a relative increase in both W^{4+} and N content. The film does maintain a residual oxide content as it does even with more aggressive KOH etching.

Selective oxide dissolution raises several concerns about eventual stability and properties of these films. One concern is how the oxide sub-phase is distributed in the film and can this lead to nanoporosity once the oxide is removed. TOF-SIMS analysis was conducted in a sputter depth profiling mode to get an idea of the depth distribution of species. The results are shown in Figure A6 and demonstrate that O and N appear to be uniformly distributed throughout the depth of the film. Several anomalous features show up in this profile. The first feature is the presence of Si in the near surface of the film. Profiles on sputtered W and metallic CVD W show only traces of Si at the film surface that can be associated with silicone-based surface contaminants. The depth of penetration shown in Figure A6 indicates that Si from the deposition reaction may still reside in the near surface. However, XPS does not produce a measurable Si(2p) intensity indicating that the near-surface Si concentration is < 1 atomic percent. The fact that the secondary ion signal is enhanced in the SIMS measurement is a result of the presence of the electronegative O species which is known to produce orders of magnitude enhancement in ion yields. This same ion yield enhancement is most likely what produces the high Si signal at the W oxynitride/Si interface. Headley and Kotula showed that the Si interface

is decorated with a very thin oxide layer underneath the selective W film with using EELS (A6). They also showed that the grain size is larger at the W oxynitride/Si interface averaging 5 nm versus 2 nm at the outer surface. The SIMS data indicates that although structure is not homogeneous, the composition is. If composition plays a role, heterogeneity must exist on a lateral length scale and, given the grain size, determining this variation will be very challenging.

Concerns of eventual stability of these selective films are also reflected in post-immersion analysis. We have used a combination of post-immersion atomic force microscopy (AFM), field emission secondary electron microscopy (FE-SEM) and scanning Auger mapping (30 nm beam diameter) to determine the morphological consequence of selective dissolution of the oxide. A number of morphological changes are produced with aqueous immersion. FE-SEM analysis (Figure A7a and c) shows evidence of roughening with immersion producing what appear to be small pores in the film. AFM (Figure A7b and d) shows these same structures only at high resolution. The rms roughness increases from a value of 0.44 nm for the as-deposited film to 0.97 nm for the immersed film. Further evidence of pore formation comes from the appearance of hydrous silica particles on the surface. Figure A8a shows a number of these spherical particles sitting on the surface. Particle diameters range from 30 to 100 nm. We also find evidence of elongated, silica-based structures that have grown on top of the W film, as seen in Figure A8b. All of these results indicate that the W film has been permeated by solution with time leading to eventual local exposure of the Si substrate. The appearance of the silica particles indicates that the underlying substrate is undergoing corrosion most likely because the remaining oxynitride can support the oxygen reduction reaction. The silica is a consequence of Si oxidation and re-precipitation at the surface as a hydrous form of silica. It is unlikely that the source of the Si is dissolution of the outer layer of the film because XPS results show the presence of Si at several atomic percent after solution exposure when no Si is detected prior to immersion. The results point to a greater source of Si as in the case of the underlying substrate.

Attempts to monitor this porosity development through the film with in situ AFM imaging have proven to be quite difficult. The principle problem is that tip assisted dissolution of the near-surface of the film takes place. We have conducted numerous experiments using 0.06 $N \cdot m^{-1}$ force constant Si_3N_4 probes and have found that as much as 5 nm of the film can be etched away after prolonged periods of imaging. We learn that nN forces are sufficient to stimulate accentuated dissolution of the outer half of the film. Interestingly, attempts to completely breach the film are never successful. It is possible that the large grains at the inner interface of the films as found by Headley and Kotula (A6) are more chemo-mechanically stable at these force levels. Not surprisingly, if these same measurements are conducted in pH 2 phosphoric acid, we typically observe less than half or 2 nm of maximum film dissolution. Clearly, the oxide sub-phase is the de-stabilizing constituent in these films. This potential for a tribological component to material loss is addressed further in the following water condensation studies.

A5.0 Processes in Condensed Water Layers

A5.1 Processes on Selective CVD Tungsten Surfaces

The results at this stage are focused on understanding the types of processes that can occur at a W thin film surface given ample time and a sufficiently large reservoir of water. Atmospheric-based corrosion should result in condensed water layers with limits on layer thickness and the capacity for dissolution pinned by the solubility product of the dissoluted species. From the perspective of material use in microsystems, the focus is less on the extent of damage via dissolution and more on the possibility of significant local effects due to dissolution. A soluble species coupled with capillary condensation creates the possibility for particle generation during wet-dry cycles or possibly chemical fusing of closely spaced surfaces where capillary condensation is most likely to occur. A need exists to gain some understanding of what processes are likely to occur in thin water layers

Water condensation on selective CVD W films produces a morphology consistent with early stages of oxide dissolution. Figure A9a and A9b show a set of contact mode AFM images acquired under flowing N_2 of the as-deposited film and a film following 16 hours of exposure to purified air at a controlled RH of 80%. The as-deposited film shows the typical fine grained morphology with grain diameters ranging from 10 to 20 nm, grain height above the mean plane of the surface at 2 nm and a root mean square roughness of 0.4 nm. Definition of the smaller diameter grains is lost after water condensation yielding a surface with only the 20 nm or larger grain diameters, grain height above the mean plane of the surface at 1 nm and a root mean square roughness of 0.2 nm. This variation is consistent for numerous 0.5x0.5 μm^2 regions probed on the sample surface. The effect of the water layer appears to be the initial dissolution of the oxide sub-phase at the surface and its redistribution. XPS measurements show a 2 to 3 fold decrease in the relative N content after exposure with a predominant hexavalent W signal consistent with oxide redistribution over the surface. No larger scale morphology has been detected on these surfaces indicating uniform dissolution. In turn, uniform dissolution suggests that the rates of water condensation and wetting dynamics must be reasonably balanced with the dissolution rate of the oxide, otherwise we might expect to see a morphological difference in regions where water condensed first. An alternative explanation is the wetting by water is heterogeneous but the dissolution assists in driving the uniform wetting by altering the free energy of the W/water interface or the surface free energy of the water domain. We also note that even with extended condensation exposures up to 72 hours silica particles or local regions of accentuated dissolution have not been detected on this selective CVD W film.

A more striking effect of water condensation on the selective CVD W surface is a measurable change in the local mechanical properties of the film. Figure A10a and A10b shows a 2x2 μm^2 scan region imaged under 80% RH using a 0.6 $N \cdot m^{-1}$ Si_3N_4 tip. This region had been previously repetitively scanned in two adjacent 1x1 μm^2 areas. The imaging cantilever detects the location of these two previously scanned regions showing topographic rises at the edges of the original scan areas. These features have a sharp rising edge at the scan region perimeter and a gradual descent outward. They appear as berms of oxide that have been mechanically displaced by the scanning tip. Average height difference between the inner scan plane and the sloping outward berm edge relative to the berm crest are 1.2 and 0.4 nm, respectively. Two additional scanned regions are visible in this image, including the lower portion of a 0.5x0.5 μm^2 region slightly left of center in the top 1x1 μm^2 region and a second, smaller 0.25x0.25 μm^2 area

close to the center of the bottom 1x1 μm^2 area. These areas were scanned first using a fixed line rate for all regions shown. So, the smaller the area scanned the longer the time the local pressure is applied with tip contact at the surface. Nominal 1.6 nm and 0.8 nm recess depths are measured for the 0.25x0.25 μm^2 and 0.5x0.5 μm^2 areas, respectively, qualitatively consistent with the 2-fold increase in contact pressure·time product for the fixed line scan rate. What we have demonstrated is that a moderate force contact, on the order of what would be present in a microsystem, is sufficient to facilitate the dissolution of the surface oxide sub-phase for this material. The presence of the berm structure indicates that dissoluted material is likely to remain in the contact region contributing to the possibility of solid bridging with a subsequent drying cycle.

A5.1 Processes on Metallic CVD Tungsten Surfaces

Water condensation on a nanocrystalline metallic W surface provides a sufficient dissolution reservoir to allow for corrosion with the presence of O_2. The initial stage of corrosion is manifest in a change in surface morphology for these films. Figure A11a and A11b shows contact mode AFM images of the as-deposited film and a film exposed to purified air at 80% RH at 23ºC for 16 hours. The as-deposited film shows a fine grained morphology with two distributions of grain sizes: the base layer of 10 to 20 nm diameter grains with a low density of larger > 30 nm diameter grains that protrude well above the surface plane. These larger grains protrude as much as 6 nm above the mean surface plane and contribute to a larger root mean square surface roughness of 0.6 nm. Water condensation on the surface produces a similar effect to that observed with the selective W films. Imaging after re-drying the surface shows that resolution of the finer grains is lost, the average grain height above the mean surface plane is reduced, and the rms roughness decreases to 0.3 nm. The larger protruding grains are still visible after water condensation as evidenced by the two grains that appear in the upper corner of Figure A9b.

The fact that these changes are being produced by oxidation and dissolution of W in a condensed water layer are demonstrated using surface spectroscopy. Figure A12 shows the W(4f) photoelectron spectra for the as-deposited and the exposed films. As discussed previously, this film is predominantly metallic tungsten capped with an approximate 1 nm thick WO_3 layer. Exposure to 80% RH air results in a relative increase in W^{6+} emission demonstrating that a thicker oxide layer has formed on the surface. We estimate this resulting oxide layer thickness to be 7 nm indicating that the oxide has grown an additional 6 nm due to surface corrosion. Reasonable estimates of the depth from which we acquire chemical information are 6 nm for metallic tungsten and 9 nm for the oxide. Given the large specific volume ratio for WO_3 relative to W of 3.4, it is possible to generate this thicker oxide by oxidizing at a minimum 2 nm or 20% of the original thickness of the CVD film. We learn that a considerable depth fraction of the film has been impacted by exposure to H_2O and O_2.

The exact composition of this oxide can not be determined using XPS. The peaks observed for W^{6+} are sufficiently broad and those for W^0 of low intensity, that the presence of W^{4+} and W^{5+}, stable valence states for W, cannot be ruled out. In addition, the exposed film surface experienced dehydration once it was removed from the humid atmosphere and placed in the vacuum environment necessary to conduct electron spectroscopy. As a result, we can only speculate on the origin of the chemical species that

give rise to the W^{6+} signal. Likely constituents include tungstic acid (H_2WO_4), a polytungstate species like $H_{10}W_{12}O_{41}$ or a hydrated tungsten hydroxide ($WO_3 \cdot nH_2O$) (A16).

The early stages of corrosion appear to be controlled by wetting of the surface by condensed water, oxidation of W and redistribution of the dissoluted oxide. More dramatic changes are observed for longer term exposures. Figure A13a shows a contact mode AFM image of a surface exposed to a continual flow of purified air controlled at a humidity of 80% RH at 23°C for 18 hours. A set of five large pores are visible in this 2x2 μm^2 tilted projection image: two pores along the bottom, one pore along the left, and one pore along the top edges of the scan region plus one elongated pore in the center. The center feature is actually two closely spaced pores and is better viewed in the plan view image shown in Figure A13b. The plan view also shows that the left pore appears to be a cluster of three closely spaced pores while several smaller pores also appear in this view. Sampling of additional area of the surface shows that these pores are a common feature yielding surface densities of 10^8 pores$\cdot cm^{-2}$. The larger pore diameters average from 100 to 300 nm and depths are in excess of 3 nm, the geometric limit of the depth that can be measured given the shapes of the cantilever probe and pore opening. Smaller individual pores or small pores in clusters have diameters 30 to 50 nm. The presence of these pores indicates that corrosion of the thin film becomes localized as some point producing regions of accentuated dissolution. The film surface around these pores possesses a smooth texture with an rms roughness of less than 0.2 nm with minimal resolution of remnant grain structure. We interpret this smoothing to be a direct result of the re-distribution of dissoluted oxide at the surface.

Longer term exposure of these metallic films to this condensed, corrosive environment leads to more pronounced pore formation. Figure A14 shows AFM images of the previously discussed ample exposed for 18 hours and a second film exposed to 42 hours at 80% RH. The 8x8 μm^2 images show that the longer term exposure yields a comparable density of larger pores. Image analysis of these two images shows that the area fraction occupied by pores has increased by 50% from 8% at 18 hours to 12% at 42 hours. The implication is that pore formation propagates with the time. This data taken as a whole suggests that early in the condensation process a mechanism or combination of mechanisms localize the corrosion and dissolution events. This localization process is unique to the adsorbed layer of water as opposed to the film itself because we do not observe pores in immersed and partially corroded films. The late stage appearance of the pores indicates that localization is most likely not related to the wetting characteristics of the surface that drive the initial nucleation and growth of water layers. Supporting this argument is the fact that we do not observe domains exhibiting original grain morphology and smoother, dissolution morphology. Instead, the pores appear to be driven by later stage forces possibly altered surface wetting dynamics and repassivation of local regions due to precipitation of the dissolution byproducts. A process of precipitation could have a propagating effect as density gradients in the liquid layer might drive material away form an evolving pore resulting in deposition at the pore perimeter, shutting down corrosion in this perimeter region and further concentrating oxidation and dissolution within the pore. The pore environment would also be expected to have a unique pH as the hydrolysis of the W cation is a proton generating reaction. Note that equation A1 is written as a hydroxide consuming reaction to conform to the anticipated near neutral environments

expected in a condensed water layer. So, local chemistry changes may also contribute to a propagating attack of the W film.

A number key issues can be identified based on the metallic W work reported up to this point. We have demonstrated that nanocrystalline W films exhibit appreciable corrosion rates and, despite variability in magnitude, these rates warrant concern at relative humidities and closed spaced geometries where capillary condensation is favored. Our work demonstrates that corrosion can take place in condensed water layers and is not significantly impeded by limits of mass transport. The efficiency for this process may reflect the wetting dynamics of water films that are near saturation in their tungstate anion content. The tip assisted dissolution processes identified in this work raise interesting possibilities when considering the tribological properties of the selective W oxynitride films. It may be possible that these films are essentially self-lubricating when hydrated. This potential property might contribute to the favorable wear characteristics as reported by Dugger (A17). The ability of the film to slowly take up oxygen, apparently from the ambient atmosphere with time suggests a potential self-lubricating property could be sustained under controlled atmosphere conditions.

A6.0 Critical Length Scales for Corrosion Processes in Aluminum – Void and Pore Formation

Aluminum represents another passive metal, like W, than is protected by an ultrathin oxide layer. Little information is known as to how the structure and composition of this oxide evolves with water exposure or when it is chemically stressed. Application of AFM techniques represents an opportunity to answer some critical outstanding questions concerning length scale issues in localized Al corrosion. One specific issue involves a description of the physical size dimensions of the localized corrosion or pit precursor site. All current pitting models in the literature require some catastrophic rupture of the passive oxide through mechanical stresses amplified by dissolution-based thinning, stresses generated by electrostrictive pressures, or stresses in the oxide over void-like structures (A18,A19). To date, no casual relationship has been established between a potential pit precursor site and the pitting event itself. This lack of validation for existing pit initiation models is largely a result of the fact that the nanoscale structure of passive oxides has only recently become accessible to investigation due to analytical technique development and of interest to the materials science community.

We have recently demonstrated that a nanostructural feature forms within the passive oxide on Al under benign electrochemical conditions (A20,A21). This feature is a nanometer sized void that nucleates at the Al – aluminum oxide interface and grows into the oxide. The driving force for void formation appears to be the growth of the oxide itself under the electrochemical potentials that are typical for the study of pitting in aqueous Cl^- electrolytes, where Cl^- is one of a class of aggressive anions known to initiate pitting. Figure A15 shows a transmission electron micrograph (TEM) image of a cross-section of the passive oxide from an Al(110) crystal after polarization to the pitting potential. The cross-section was generate using a standard 15 keV Ga^+ ion beam to conduct a focused ion beam cutting of a 10 μm wide, 4 μm tall, and 0.1 μm thick sample from the crystal surface. The oxide layer shows up as the grey center band with a slightly darker Al layer below it and a darker, mottled carbon layer on top of it. Of interest is the oblate hemispherical structures (marked by arrows in the image) that can be seen

extending from the Al interface and into the oxide. The transmitted electron beam generates a set of darker Fresnel contrast fringes that mark the perimeter of the void. We have confirmed the fact that these structures are indeed voids, the encapsulated absence of matter, using a combination of energy dispersive x-ray fluorescence and electron energy loss spectroscopy on the TEM. The presence of these voids creates an opportunity to explore the role of the suspended oxide layer as a potential mechanical flaw responsible for initiating pitting. The voids also provide opportunities for testing whether a void alone is sufficient for initiating pitting as invoked by several leading initiation models (22,23).

AFM techniques provide a way to evaluate the fate of these voids with increasing electrochemical stress. One question that a scanning probe can readily answer is whether a void has transitioned to a pore at some particular, critical time. This determination requires some knowledge of the void population and how it develops with electrochemical conditions. A void population can be characterized in an *ex situ* or outside of solution manner by using FE-SEM to image voids as a function of the variation in time, potential and polarization rate for a given oxide. Our experiment takes the form of a single sample that is probed using a capillary electrochemical cell. Up to 50 individual experiments can be conducted at unique locations on an Al sample surface, each one subjected to a variety of *ex situ* characterization techniques like FE_SEM and AFM.

Voids can be readily imaged using field emission secondary electron microscopy. Figure A16 shows a representative micrograph of an Al film polarized to pitting at –330 mV versus the saturated calomel electrode (SCE, a standard reference electrode) at a scan rate of 0.167 $mV \cdot s^{-1}$ in de-aerated, 50 mM NaCl. This polarization produced 5.5 $mC \cdot cm^{-2}$ of faradaic charge density from open circuit up to the transition to stable pitting. Voids appear as the dark spots or regions of attenuated electron emission in this image. The average void density measured for a number of sites on this sample is found to be $9(\pm1)x10^{10}$ cm^{-2}. The void population, as shown in Figure A17, exhibits a wide range of void sizes from 4 to 30 nm with the largest density of voids at a 6 nm diameter. At the 5 keV incident energy used, SEM is not sensitive to whether the oxide cap is still intact over the original void and the larger size voids are the most likely structures to have opened up with continued three dimensional growth.

The possibility of a void-to-pore transition can be explored using scanning probe microscopy. Figure A18 shows a topographic image of a site on this same sample using contact mode AFM. Imaging was conducted in N_2 using a Si_3N_4 cantilever with a force constant of 0.6 $N \cdot m^{-1}$ and a tip radius of nominally < 20 nm. The image shown is a 1x1 μm^2 region compared to the slightly smaller 0.6x0.6 μm^2 region in the SEM image of Figure A16. Grey scale is used to represent a total span of 23 nm in vertical height with white representing highest features. The image shows a number of approximately circular pores ranging in diameter from 20 to 30 nm that are distributed among the electrochemically modified but intrinsic morphology of the 100 nm diameter Al grains. The pore population is also plotted in Figure A17 to allow for a comparison of the two populations. What is evident from these images and the population plot is that AFM is clearly detecting an increasing fraction of the voids as the void size increases from 12 to 50 nm diameter. We find a pore areal density of $4x10^9$ cm^{-2}, which is 5% of the void density indicating a significant conversion efficiency for voids to pores prior to pitting.

The lower diameter limit of 12 nm may reflect the minimum size pore throat where the cantilever first shows a deflection into the surface plane above the amplitude changes created by the background texture on the grain facets. The smallest feature might truly be smaller voids that have fully lost their capping oxide layer or they may be larger voids that have only lost the central portion of this oxide. In either case, these images and the resulting image analysis clearly demonstrate that voids transition to pores and that this transition takes place prior to the onset of stable pitting. The relevance of voids in this system and the probability of pore conversion suggest that void alone are not sufficient to drive stable pitting in the aqueous Cl^- - Al system.

A7.0 Conclusions

Two systems have been explored where a critical length scale applies to the corrosion mechanism and resulting stability of a nanocrystalline passive metal. Nanocrystalline W films were studied and shown to undergo uniform corrosion in immersed conditions at rates that are reasonable based on extrapolated data for bulk W. A Sandia developed selective CVD W was confirmed to be an oxynitride. Immersion of this material leads to the selective dissolution of an oxide sub-phase, porosity development and eventual corrosion of the underlying Si substrate. These immersed experiments set lower limits for the stability of these films under conditions of atmospheric water condensation. Both nanocrystalline metallic W and the selective oxynitride exhibit dissolution and redistribution of a tungstate species in surface water films. Redistribution leads to a smoothing of the surface morphology. The metallic films exhibit 10^2 nm diameter pore formation as a result of the development of regions of accentuated dissolution that appear to be driven by the wetting dynamics of the water overlayer. Nanocrystalline Al was a second passive metal system studied. The passive oxide on Al is shown to develop voids under benign electrochemical conditions that nucleate at the Al – oxide interface and grown into the oxide. These voids transition to pores below the critical pitting potential. AFM imaging allows for the determination of a 5% conversion efficiency for voids to pores. The prevalence of the voids and their ability to break through to solution suggests that the presence of a void itself is not sufficient alone to drive stable pitting in the aqueous Cl^- - Al system. The implication of this study is that the stable pitting process is distributed have several key mechanistic steps that act in a concerted fashion to lead to pitting.

A7.0 References

1. E.K. Broadbent and C.L. Ramiller, J. Electrochem. Soc. **131**(6), 1427-1433 (1984).
2. M.L. Green and R.A. Levy, J. Electrochem. Soc, **132**(5), 1243-1250 (1985).
3. S.S. Mani, J.G. Flemming and J.J. Sniegowski, Proc. SPIE **3874**, 150-157 (1999).
4. J.W. Klaus, S.J. Ferro and S.M. George, Appl. Surf. Sci. **162-163**, 479-491 (2000).
5. S.S. Perry, H.C. Galloway, P. Cao, E.J.R. Mitchell, D.C. Koeck, C.L. Smith and M.S. Lim, Appl. Surf. Sci. **180**, 6-13 (2001).
6. J.A. Walraven, S.S. Mani, J.G. Flemming, T.J. Headley, P.G. Kotula, A.A. Pimentel, M.J. Rye, D.M. Tanner, and N.F. Smith, Proc. SPIE **4180**, 49-57 (2000).
7. M. Pourbaix, “Atlas of Electrochemical Equilibria in Aqueous Solutions,” Pergamon Press, Oxford, 1966, p. 280-285.

8. W.L. Acherman, J.P. Carter, C.B. Kenehan and D. Schlain, “Corrosion Properties of Molybdenum, Tungsten, Vanadium and some Vanadium Alloys,” Bureau of Mines, RI 6715, 1966, p. 18.
9. E.A. Kneer, C. Raghunath, S. Raghavan, and J.S. Jeon, J. Electrochem. Soc. **143**(12), 4095-4100 (1996).
10. M.S. El-Basiouny and M.M. Hefny, *Br. Corros. J.*, **16**(1), 50-52 (1981).
11. Th. Heumann and N. Stolica, Eelectrochim. Acta, **16**, 1635-1646 (1971).
12. R.D. Armstrong, K. Edmondson and R.E. Firman, J. Electroanal. Chem. **40**, 19-28 (1972).
13. I.A. Ammar, S. Darwish and M.W. Khalil, Z. Werkstofftech. **13**, 163-167 (1982).
14. M.T. Dugger, S.S. Mani, D.E. Peebles, and G.A. Poulter, Fall 2000 MRS Meeting, Boston, MA, November 27 – December 1, 2000.
15. A. Sellidj and J.L. Erskine, Surf. Sci. **220**, 253-267 (1989).
16. R.S. Lillard, G.S. Kanner and D.P. Butt, J. Electrochem. Soc. **145**(8), 2718-2725 (1998).
17. M.T. Dugger, in Nanotribology: Critical Assesment and Research Needs, S.M. Hsu and Z.C. Ying, eds., Kluwer Academic, Norwall, MA, 2003, p. 123-137.
18. G.S. Frankel, J. Electrochem. Soc. **145**(6), 2186 (1998).
19. Z. SzKlarska-Smialowska, in Corrosion Science: A Retrospective and Current Status in Honor of Robert P. Frankenthal, G.S. Frankel, H.S. Isaacs, J.R. Scully and J.D. Sinclair, PV2002-13, , The Electrochemical Society Proceedings Series, Pennington, NJ, 2002, 251-265.
20. K.R. Zavadil, J.A. Ohlhausen and P.G. Kotula, in Corrosion and Protection of Light Metal Alloys, R. G. Buchheit, B. Shaw, R. Kelly, N. Missert, Editors, PV2003-23, The Electrochemical Society Inc, Pennington, NJ (2004).
21. K.R. Zavadil, J.A. Ohlhausen and P.G. Kotula, J. Electrochem. Soc., 2004, submitted.
22. J. Sikora, E. Sikora and D.D. Macdonald, Electrochim. Acta 45, 1875 (2000).
23. E. McCafferty, J. Electrochem. Soc. **146**(8), 2863 (1999).

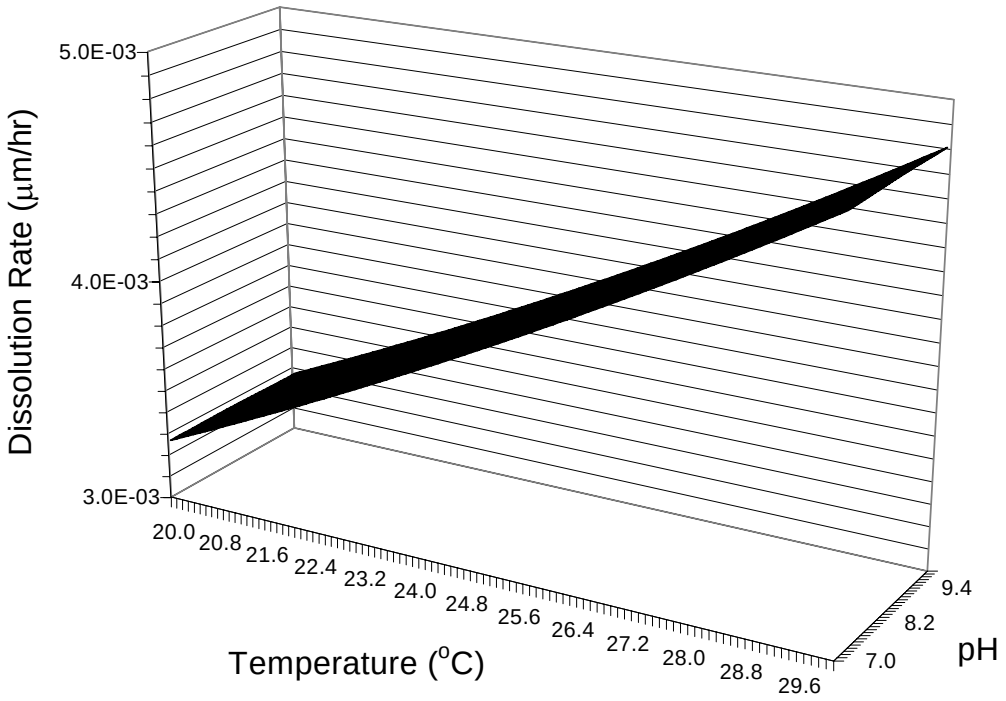

Figure A1: Variation in W dissolution rate produce by uniform corrosion as a function of pH and temperature under open circuit conditions (based on data of El-Basiouny and Hefny (A10)).

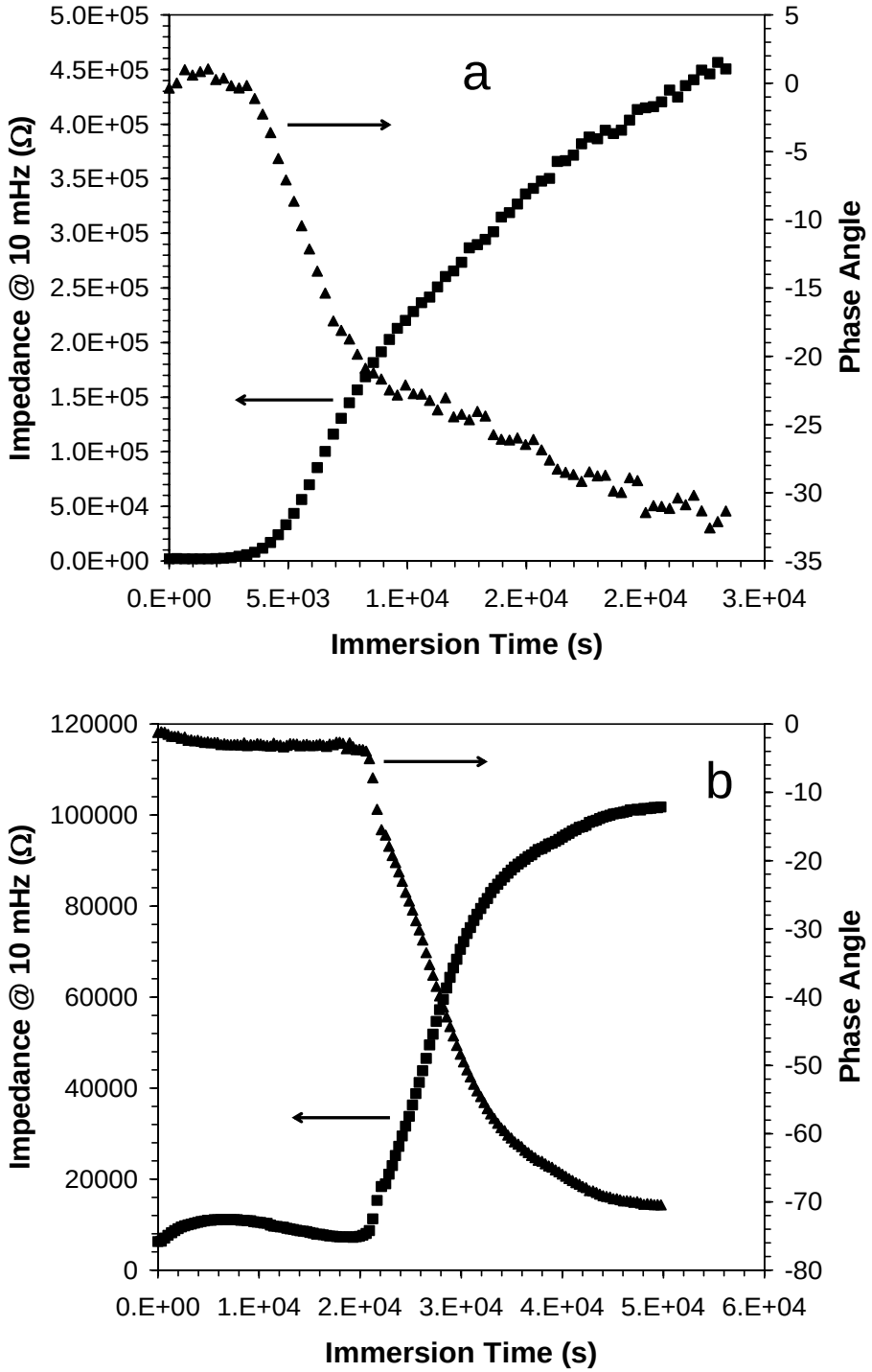

Figure A2: Time variant electrochemical impedance and phase angle signatures for a 10 nm thick sputter deposited W film on Si (a) and a 10 nm thick metallic CVD W film on TiN (b) in pH 7, 50 mM aqueous phosphate. The time at which a rapid signal change occurs is a measure of the uniform corrosion rate of each film.

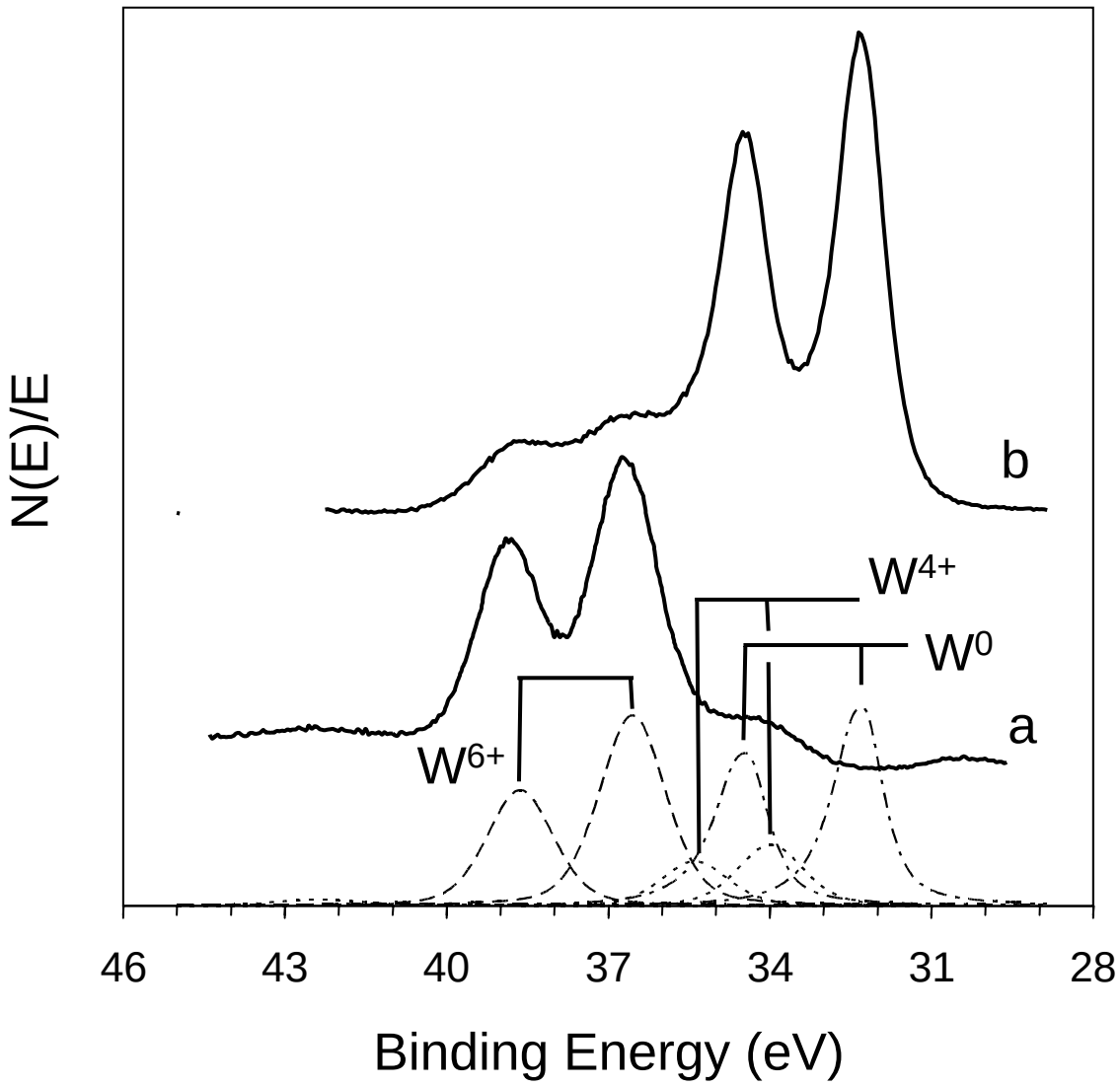

Figure A3: Comparison of the x-ray induced W(4f) lineshape for an as-deposited 10 nm thick selective CVD W film on Si(100) (a) and an as-deposited 10 nm thick metallic CVD W film on TiN (b). The dashed peaks represent fitting results for a W film comprised of 40% metallic W (W^0), 15% WN_x (W^{4+}) and 45% WO_3 (W^{6+}).

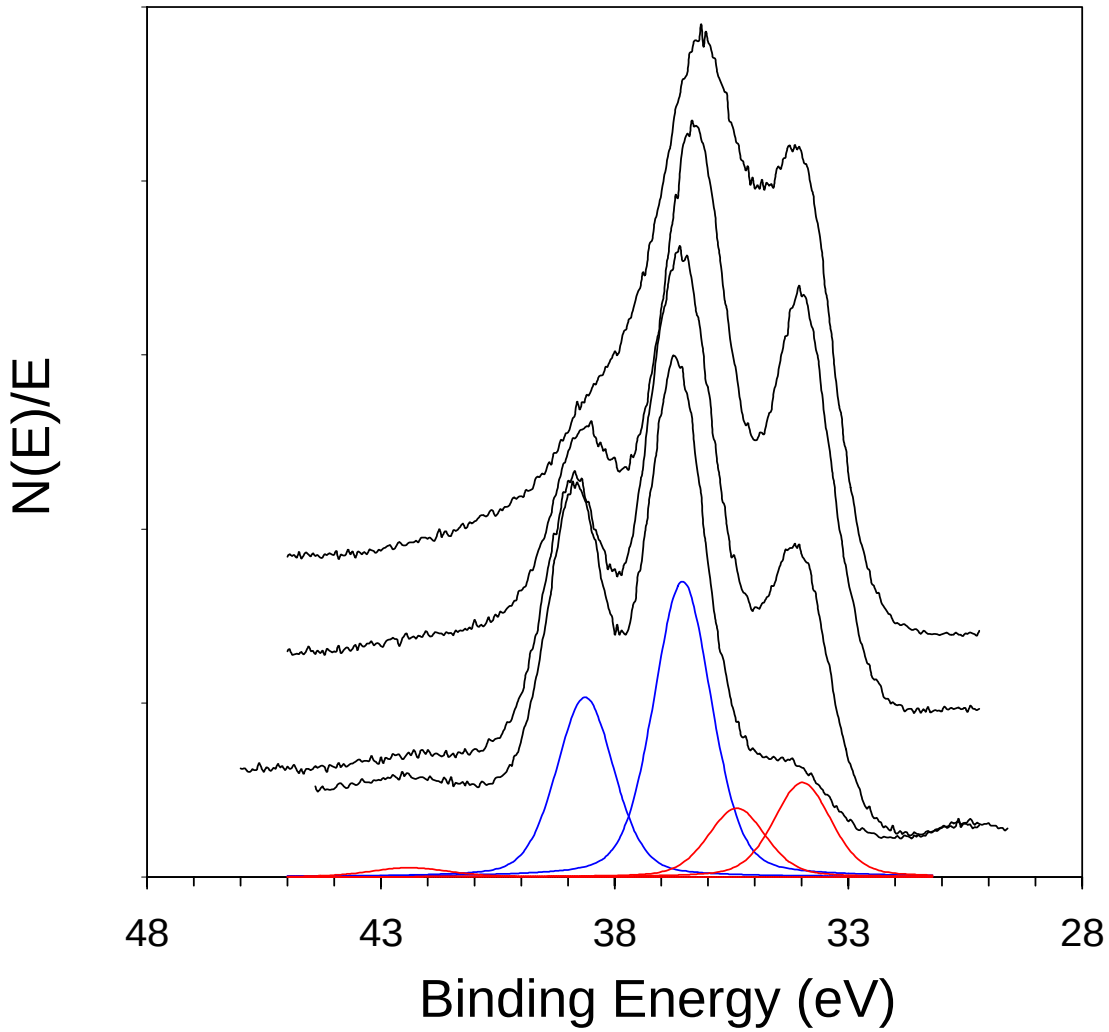

Figure A4: Changes in the x-ray induced W(4f) lineshape for a 10 nm thick selective CVD W film on Si(100) as a result of ambient atmosphere exposure (a), 11 hour immersion in de-ionized water (b), 27 hour immersion in de-ionized water (c) and after a 2 min 1M KOH etch (d). Red and blue curves represent the WN_x and WO_3 contributions to the ambient atmosphere lineshape, respectively. The relative increase in W^{4+} emission due to WN_x is evidence of selective dissolution of an oxide sub-phase in the film.

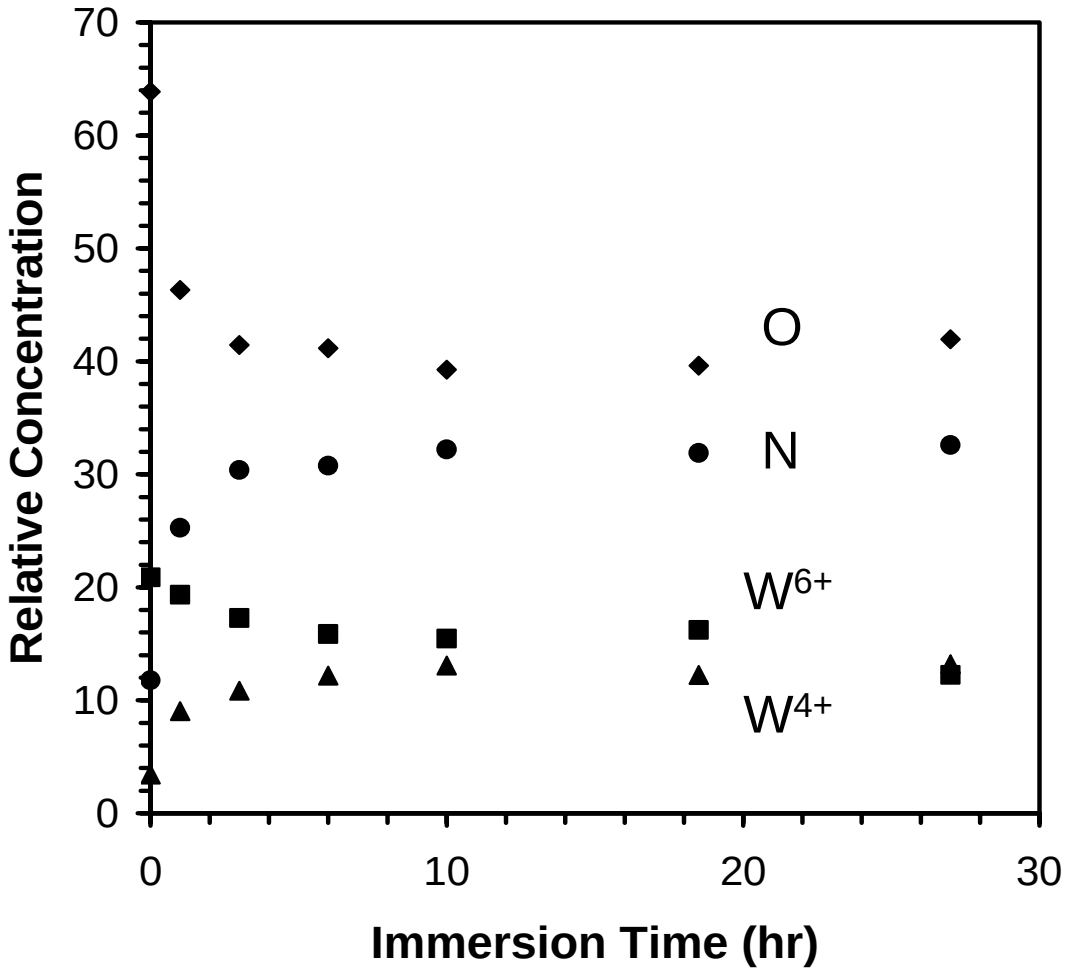

Figure A5: Variation in chemical content of a selective CVD W film on Si(100) as a function of immersion time in aerated, de-ionized water as measured by XPS. Results show selective dissolution of an oxide sub-phase.

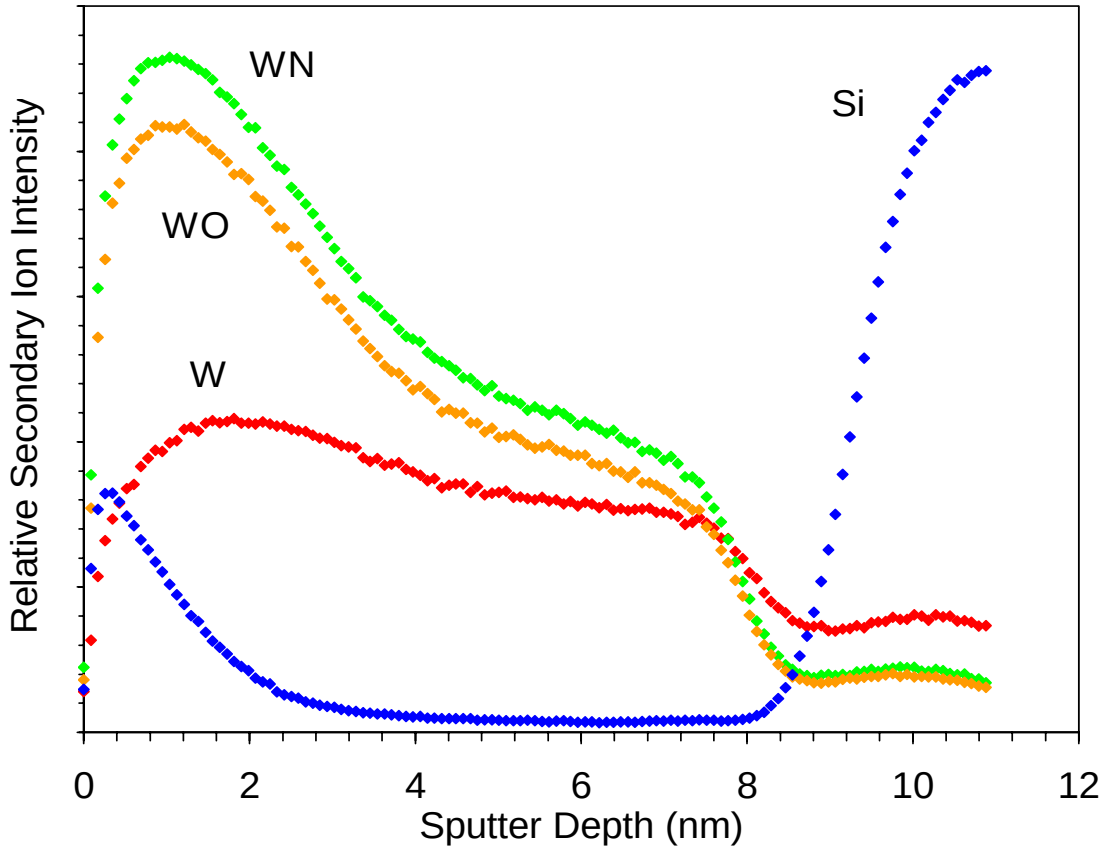

Figure A6: TOF-SIMS sputter depth profile in positive ion mode showing the uniform depth distribution of O and N in a 10 nm thick selective CVD W film on Si(100).

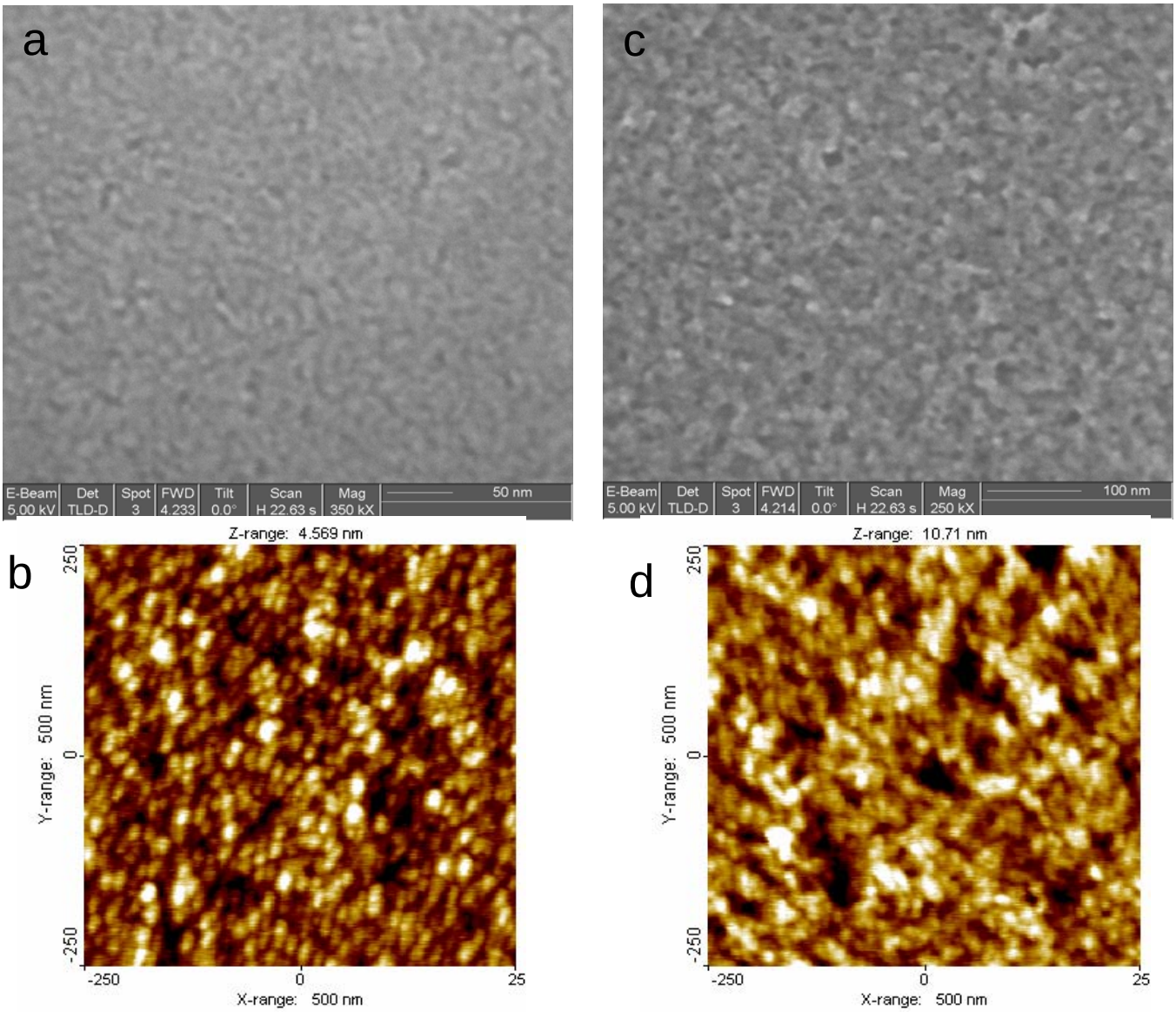

Figure A7: Comparison of FE-SEM and AFM images of a 10 nm thick selective CVD W film on Si(100) after 20 hours of immersion in de-ionized water – (a) SEM and (b) AFM images of as-deposited film, (c) SEM and (d) AFM images of immersed film.

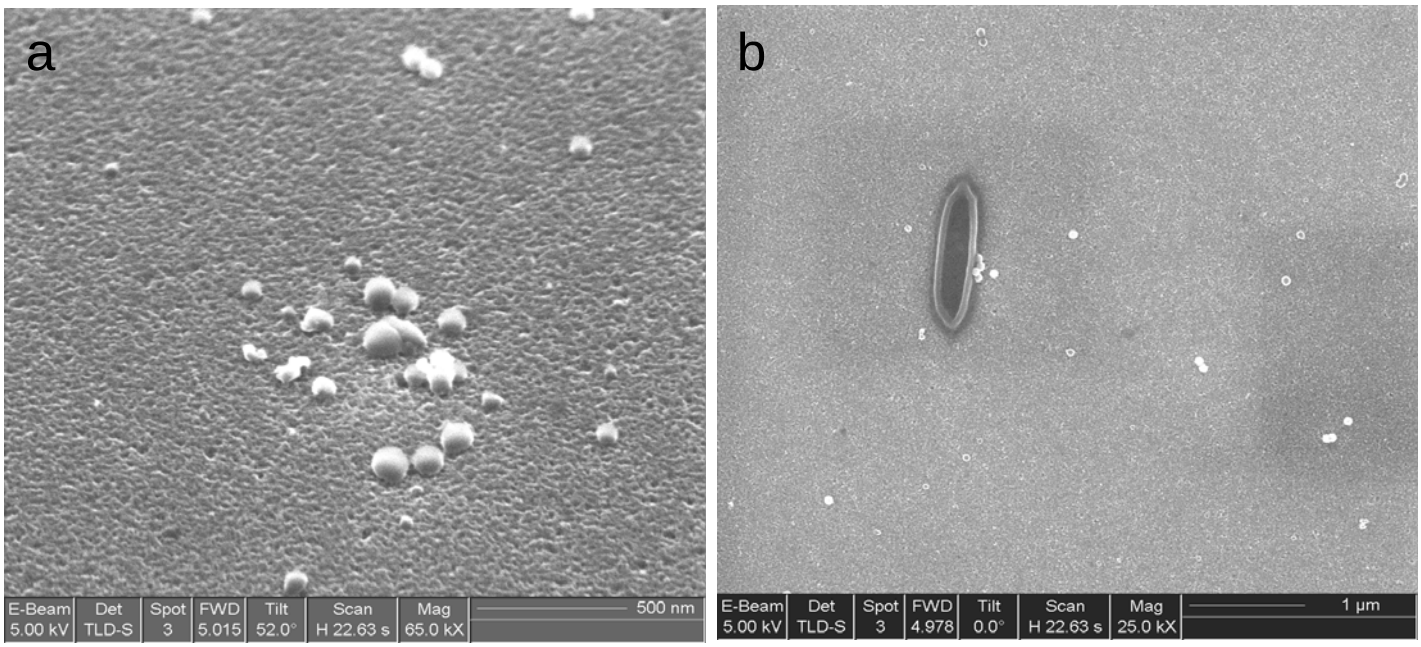

Figure A8: FE-SEM images of various silica-based morphologies that develop on a 10 nm thick selective CVD W film on Si(100) after 20 hours of immersion in de-ionized water. – (a) hydrous silica particles and (b) an elongated silica-based topographic feature. Chemical identities were determined using scanning Auger spectroscopy.

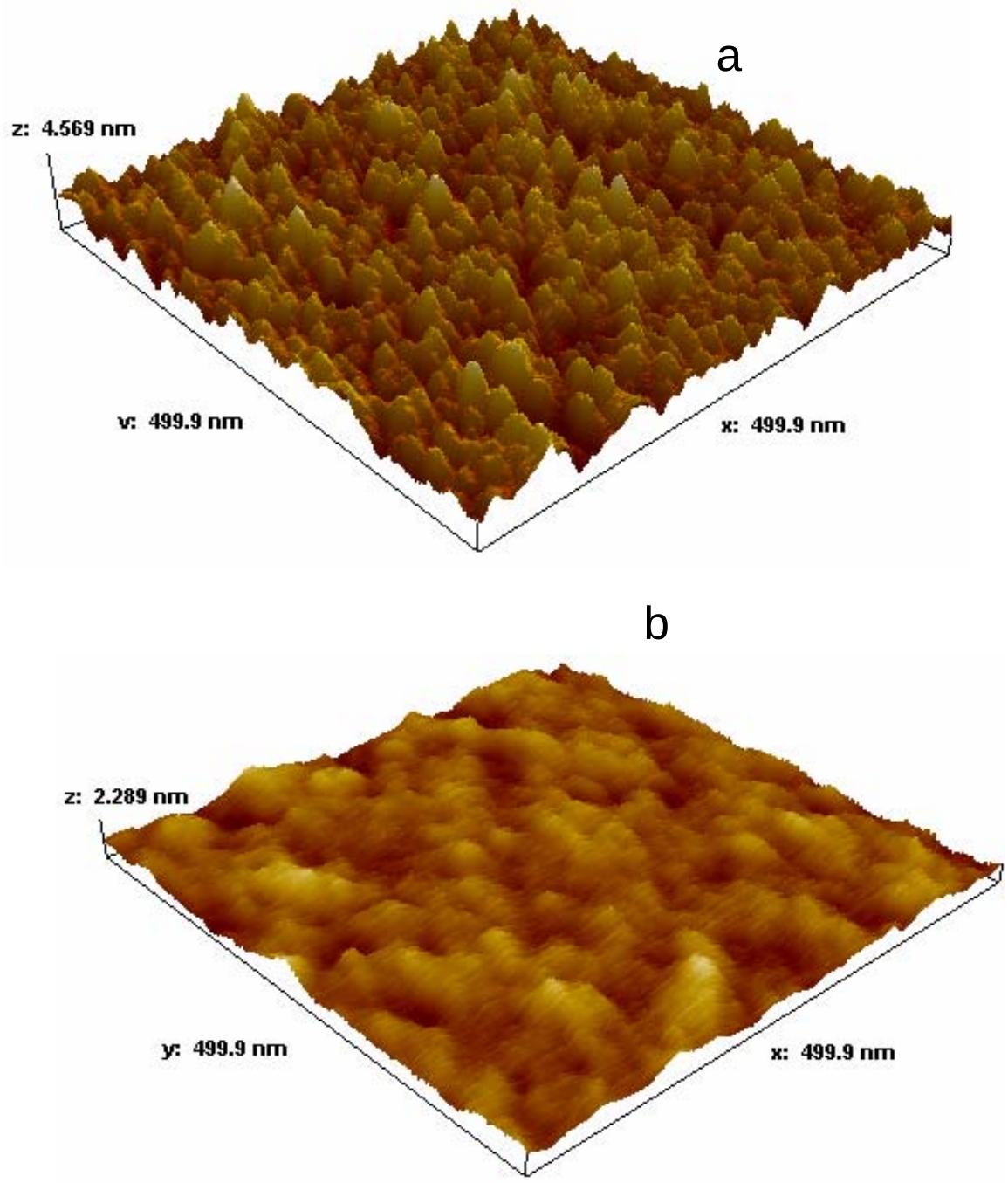

Figure A9: Comparison of the surface morphology for a 10 nm thick selective CVD W film on Si(100) – (a) as-deposited and (b) after 16 hours of 80% RH purified air exposure at 23ºC. Surface smoothing is a result of oxide dissolution and redistribution on the surface.

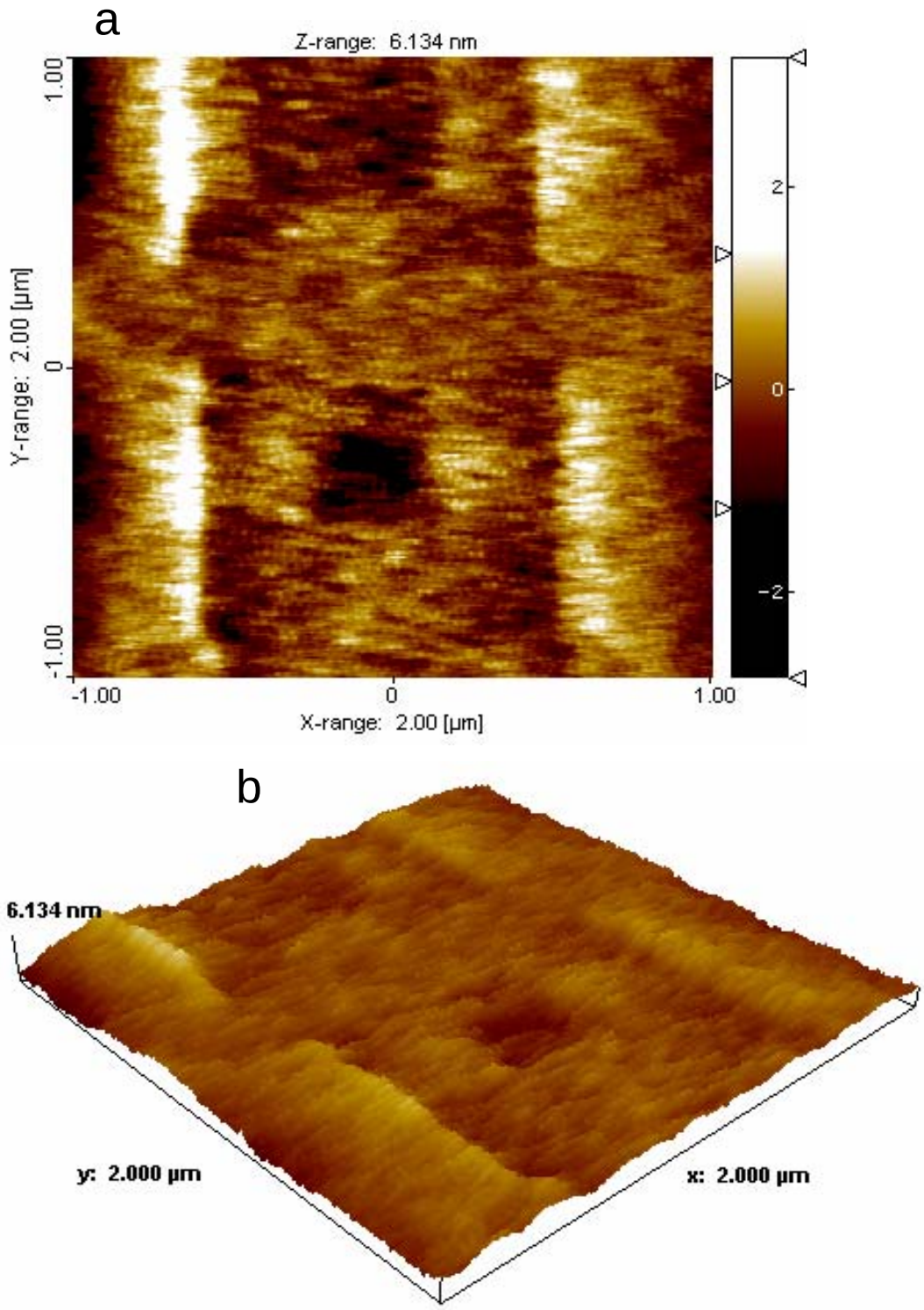

Figure A10: Wear regions on a 10 nm thick selective W film on Si(100) generated with a 0.6 Nm-1 Si_3N_4 cantilever during 80% RH purified air exposure at 23ºC – (a) plan view (b) tilted projection.

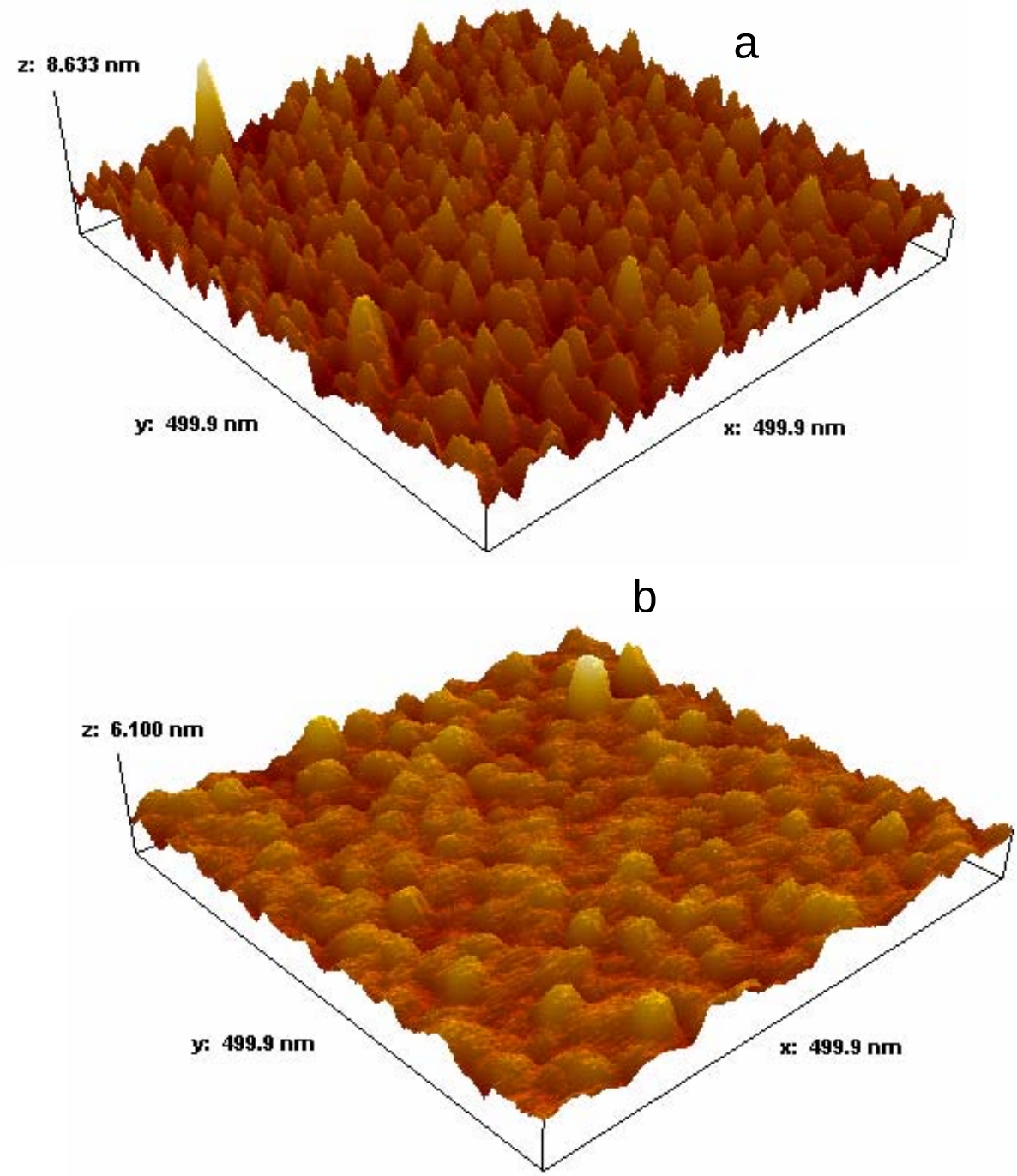

Figure A11: Comparison of the surface morphology for a 10 nm thick metallic CVD W film on TiN – (a) as-deposited and (b) after 15 hours of 80% RH purified air exposure at 23ºC. Surface smoothing is a result of oxide growth, dissolution and redistribution on the surface.

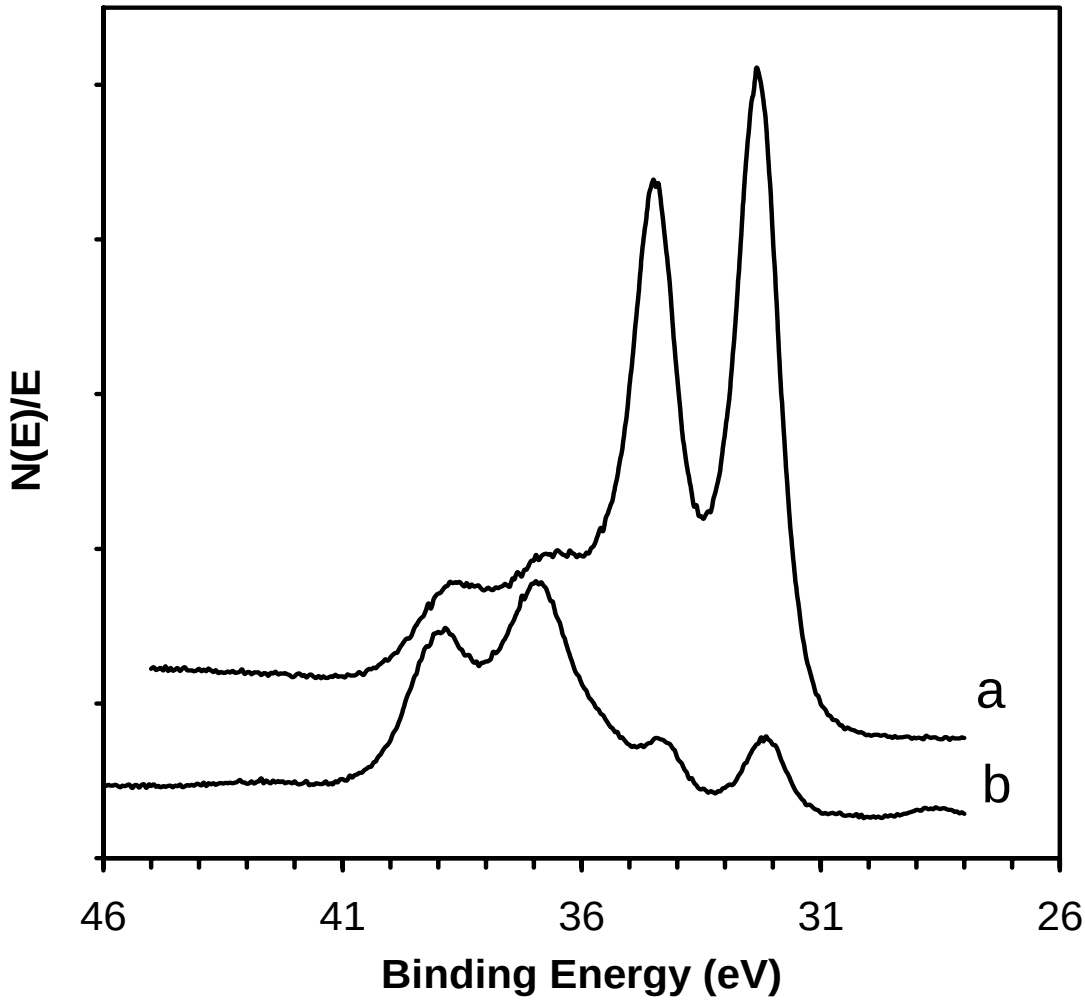

Figure A12: Comparison of the x-ray induced W(4f) lineshape for a 10 nm thick CVD W film on TiN – (a) as-deposited and (b) after 15 hours of 80% RH purified air exposure at 23ºC. The condensation of a surface water layer produces an oxide.

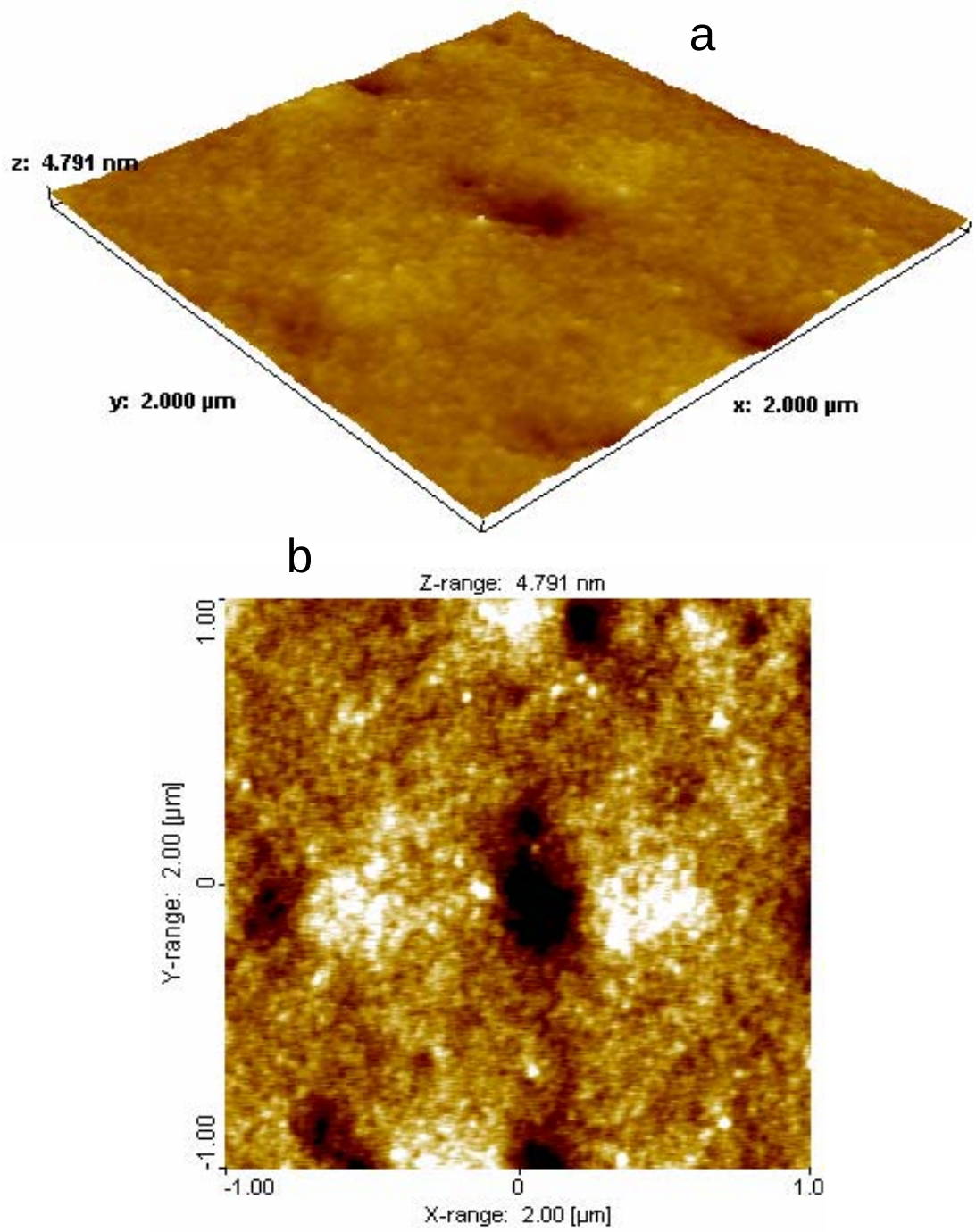

Figure A13: Contact mode AFM image of a 10 nm thick metallic CVD W film on TiN after exposure to 18 hours of 80% RH purified air exposure at 23ºC - (a) tilted projection and (b) plan view.

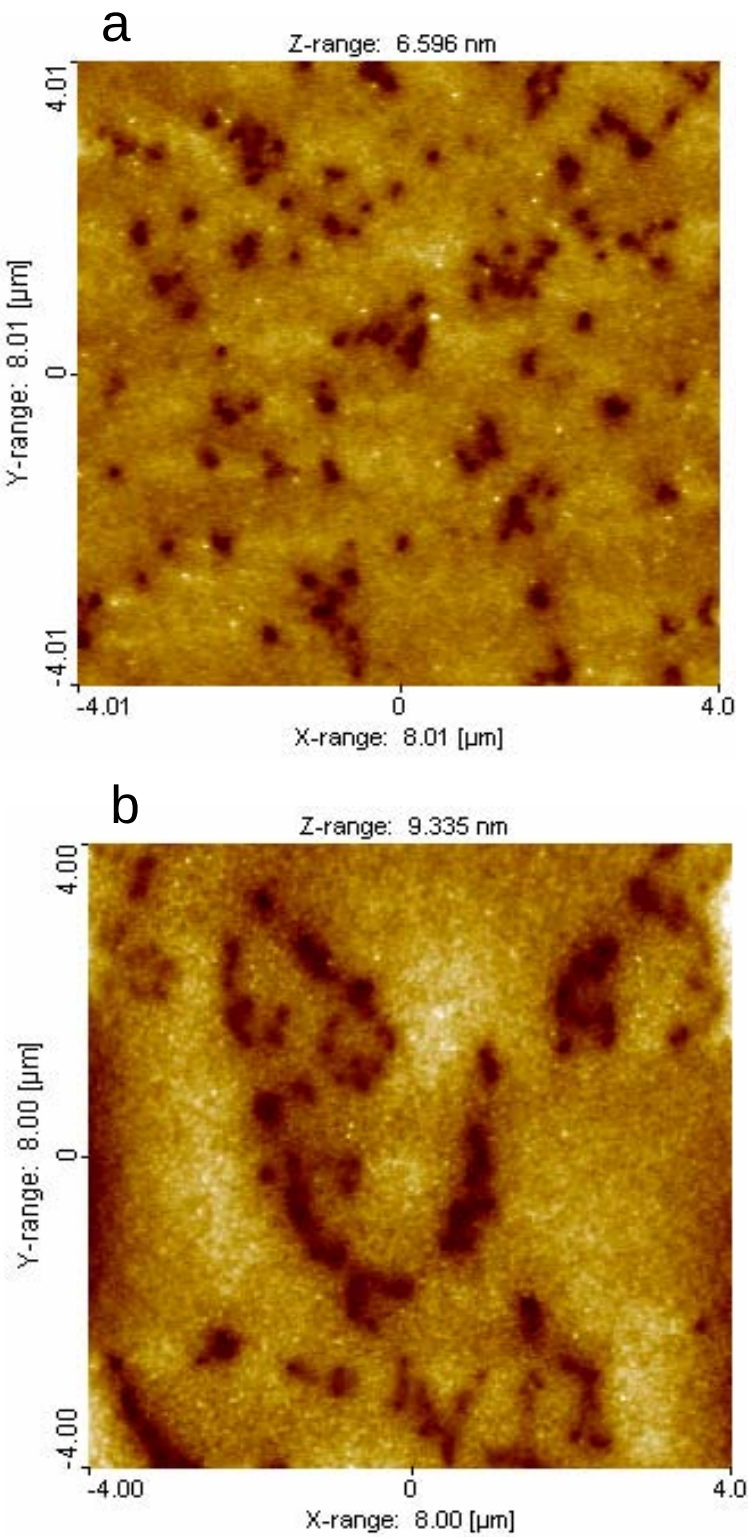

Figure A14: Contact mode AFM image of a 10 nm thick metallic CVD W film on TiN after exposure to 80% RH purified air exposure at 23ºC - (a) 18 hours (b) 42 hours.

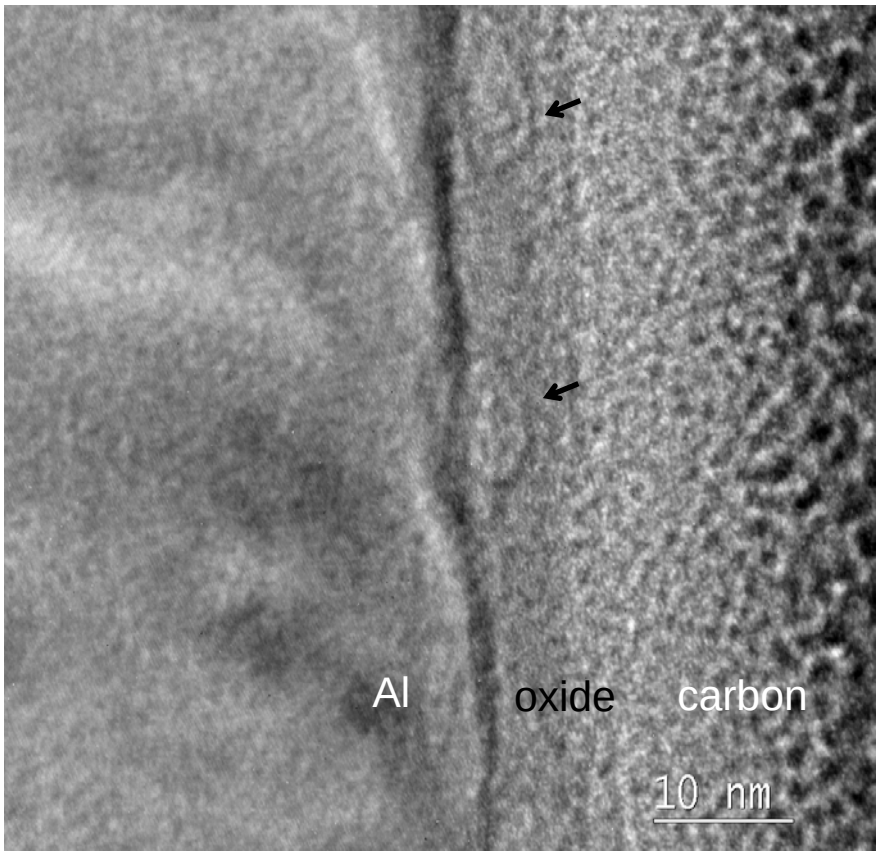

Figure A15: Transmission electron micrograph acquired from a cross-section focused ion beam cut of the passive oxide on an Al(110) crystal. The oxide comes form a site that was polarized to pitting in 50 mM NaCl at –518 mV vs. SCE generating 4.2 $mC \cdot cm^{-2}$ of charge density. Arrows indicate the location of two voids that extend from the Al - oxide interface into the oxide.

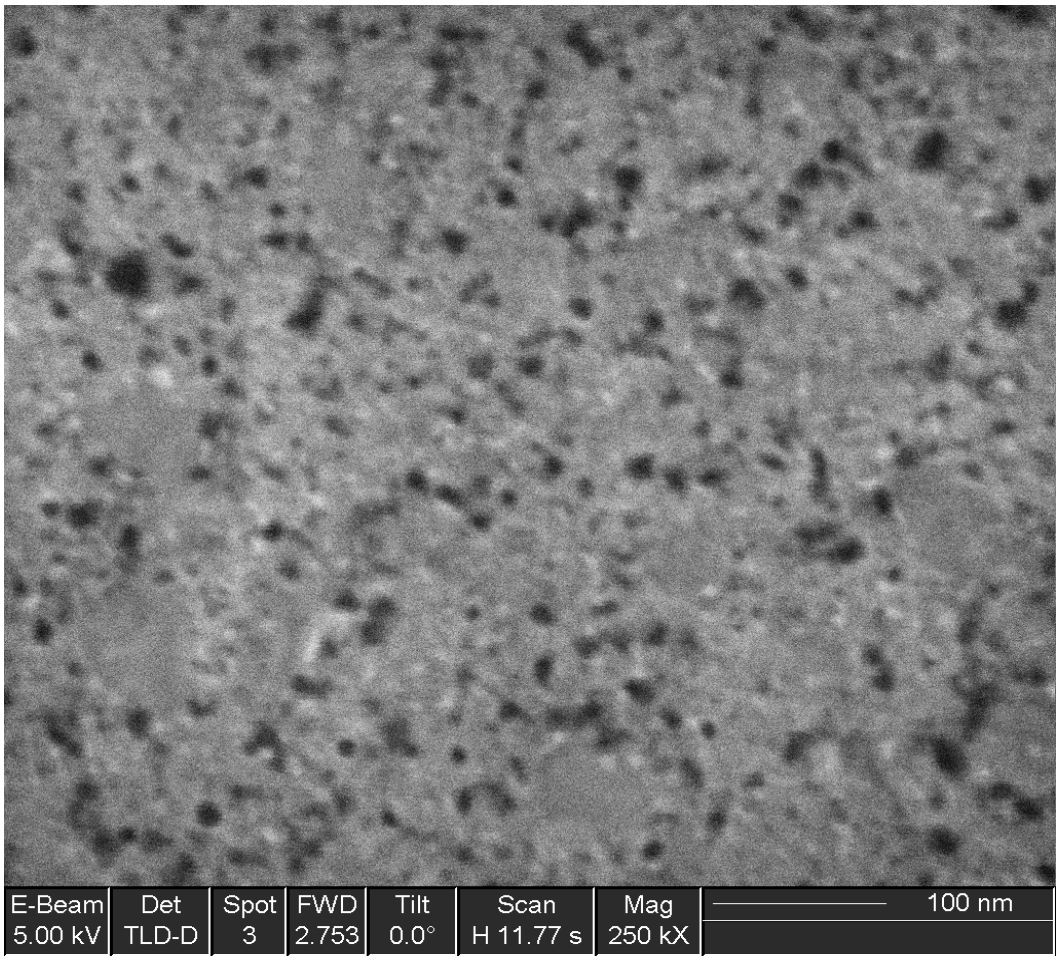

Figure A16: Field emission scanning electron micrograph acquired from a nanocrystalline Al thin film that was polarized to pitting in 50 mM NaCl at –330 mV vs. SCE generating 5.5 $mC \cdot cm^{-2}$ of charge density. The dark spots are voids (or pores) at a density of $9x10^{10}$ cm^{-2}.

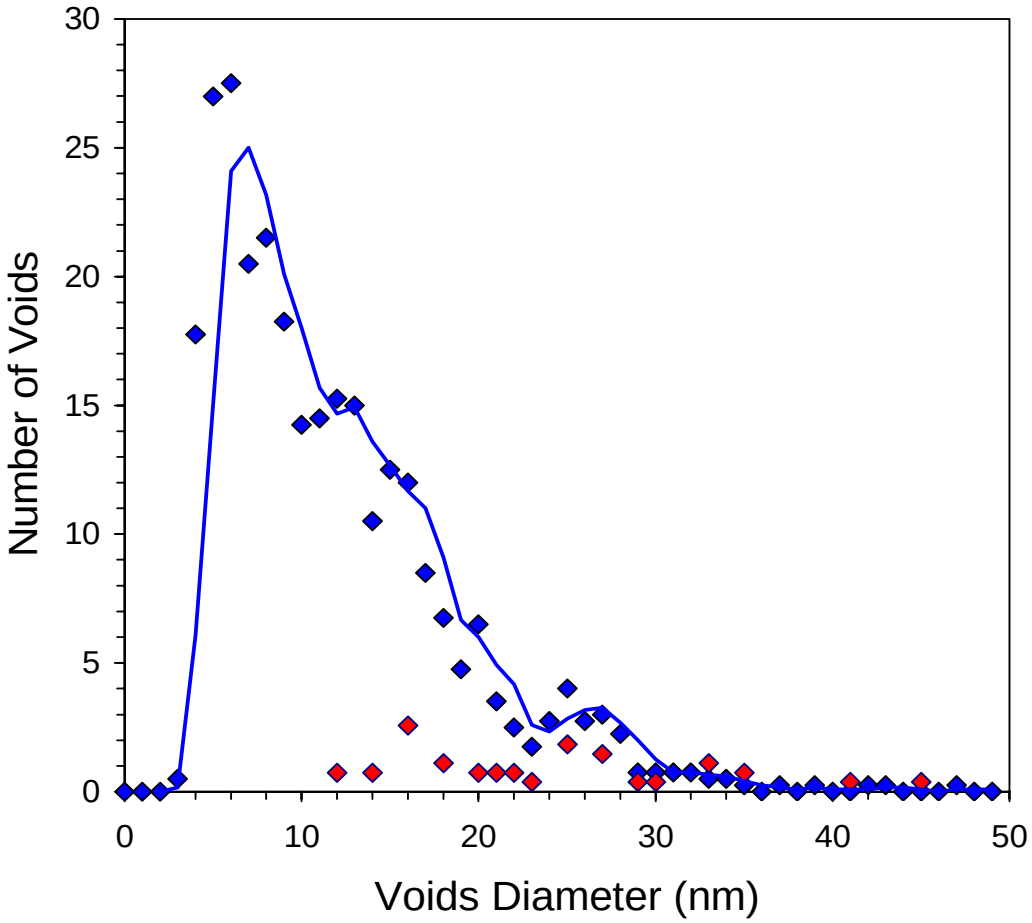

Figure A17: The SEM determined void diameter distribution (blue data) and the AFM determined pore diameter distribution (red data) for a nanocrystalline Al thin film that was polarized to pitting in 50 mM NaCl at –330 mV vs. SCE generating 5.5 mC·cm-2 of charge density.

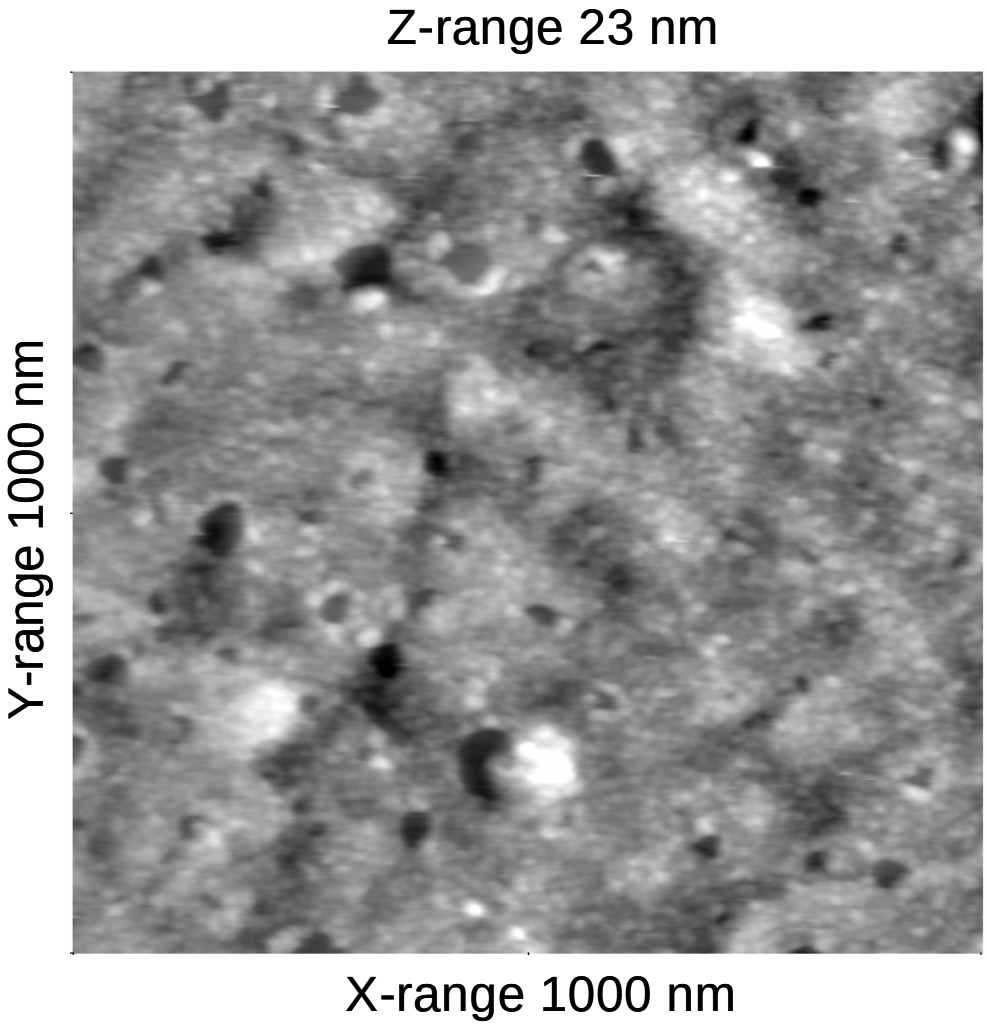

Figure A18: Atomic force micrograph acquired from a nanocrystalline Al thin film that was polarized to pitting in 50 mM NaCl at –330 mV vs. SCE generating 5.5 $mC \cdot cm^{-2}$ of charge density. The dark spots are pores at a density of $4x10^{9}$ cm^{-2}.

Section B:
A Statistics-Based Approach to Studying Aluminum Pit Initiation: Intrinsic and Defect-Driven Pit Initiation Phenomena

Summary

A statistical description of pit initiation in high purity Aluminum (99.99) is developed based on the statistical frameworks established by Shibata and Baroux. The statistical treatment is used to examine the dependency of pitting behavior on electrode area, scan rate and chloride concentration. It is shown that the average pitting potential is proportional to the log of the scan rate and the log of one over electrode area, implying an exponential dependence of pit germination rate on applied potential. The constants that describe pit germination rate are independent of area for electrodes of diameter 125 μm and smaller. However, the constants are area-dependent for larger electrodes. Based on these results a homogeneous pit nucleation process is proposed to account for pit initiation on 125 μm diameter and smaller electrodes, while a heterogeneous process is proposed to control the behavior of 500 μm diameter electrodes. The results from these studies also demonstrate the importance of correctly choosing experimental conditions when studying pitting behavior. The dependencies of pitting potential on scan rate and area are found to be sensitive to electrode size, scan rate and aggressiveness of the electrolyte.

B1. Background

B1.1. Introduction

Pitting of aluminum and aluminum alloys is often assumed to occur at locations that are physically distinct from the surrounding area. Furthermore, it is generally accepted that the sites of pitting attack represent locally weakened regions of the electrode/electrolyte interface. A contrasting viewpoint is that the location of pitting is randomly determined and cannot be identified a priori from knowledge of the material microstructure. At first, these two hypotheses may appear to be contrasting a deterministic vs. a stochastic description of pit initiation; however that is not the case. The distinction being made here is between heterogeneous and homogeneous pit nucleation. A theory of heterogeneous nucleation contends that specific sites will preferentially and reproducibly lead to pit initiation (e.g., sensitized grain boundaries in stainless steel). On the other hand, a theory of homogeneous nucleation suggests that each unit area of surface has an equal probability of pit initiation and the site that initiates first is randomly determined. However, even with a chance event leading to pit initiation, the mechanism by which the oxide breaks down can likely be described in a deterministic sense. Only the formation of a critical nucleus (e.g., locally elevated Cl in the Al oxide) would be determined randomly; the remainder of the process would follow a discrete chemical, electrochemical or mechanical pathway.

The objective of this work is to determine which mechanism of pit initiation best describes the behavior of 99.99 Al in neutral NaCl solutions during potentiodynamic polarization. To meet this objective, a statistical description of pitting behavior is developed based on the assumption that pitting is homogeneous; then experimental data are used to explore the conditions where the statistical description is valid. We present results that show how the mechanism changes from heterogeneous to homogeneous as

the electrode area is reduced. From analysis of the pitting behavior, we also discover criteria for determining the phase space in which pitting behavior can effectively be studied. We begin by reviewing the types of defects commonly attributed to pit initiation. Then a statistical description of pitting is developed based on the work of Baroux (1) and Shibata (2, 3). After the statistical framework is established, the pitting behavior of aluminum is discussed in detail as a function of scan-rate, chloride concentration and electrode area.

B1.2. Pitting in Al and Al Alloys

Heterogeneous pit nucleation is often attributed to the behavior of a local structure either in the material microstructure or in the protective metal oxide. In the case of impure aluminum or aluminum alloys, many studies have identified a propensity for pits to initiate at impurities or second phase particles. For example, noble phases such as Al_2Cu (in Al-Cu-X alloys (4-6)) and Al_3Fe (e.g., in Al 1100 (7, 8) and Al6061 (9-11)) can exacerbate corrosion at their periphery by acting as a source of cathodic current and by generating localized regions of high pH. Active phases such as Al_2CuLi (e.g, in AA2090 (12, 13)) can also serve as pit initiation sites due to locally accelerated corrosion rates. Evidence also exists to suggest that initially active particles (e.g, Al_2CuMg in AA2024) may de-alloy and then act as local cathodes (14). Grain boundaries can also offer sites for accelerated dissolution. Solute depletion along grain boundaries due to preferential precipitation can lead to active zones along the boundaries, as seen in Al-Cu binary alloys (4) and Al-Cu-X alloys (15).

Here, we are concerned with high purity aluminum, which lacks some of the common metallurgical features found in alloys. In this material, pit initiation has been attributed to flaws in the oxide. Wood *et al.* suggested that all aluminum electrodes, independent of purity or surface treatment, contain a high density of geometric surface flaws that serve as the sites for pit initiation (16, 17). More recently, White demonstrated a possible correlation between local oxide electroactivity and pit initiation on pure aluminum samples, although no specific oxide structure has been identified to account for the increased conductivity (18, 19). In the remainder of this paper, we will use the term defect to describe oxide defects in high purity aluminum (such as the geometric flaws described by Wood). Thus, in the current context, *defect* does not imply a secondary phase particle (as found in alloyed aluminum) but any structural, chemical, metallurgical or geometric heterogeneity that could serve to localize corrosion initiation on high purity aluminum.

If oxide defects do control pit initiation, then it seems reasonable that minimizing the defect content in an electrode should increase the pitting resistance. However, Yu carefully electropolished high purity Al single crystals but did not report markedly elevated pitting potentials compared to polycrystalline Al (20). Thus, in this specific case, efforts were made to reduce gross heterogeneities in the material (and oxide), yet pitting behavior was *not* shifted significantly from what is commonly observed on high-purity, polycrystalline, mechanically polished electrodes.

Because the identification of pit initiation sites on high-purity Al is not straightforward, it seems reasonable to ask a more basic question – does pit initiation in high-purity Al occur at discrete, distributed sites that can be identified by sufficient knowledge of the oxide structure, chemistry, etc., or does initiation occur at random sites on the oxide that cannot be identified a priori?

Our approach to answering this question is to define a model for pitting behavior that is only applicable to homogeneous nucleation and attempt to apply it to the pitting behavior of high-purity Al. Baroux developed a statistical model of pit initiation in which the pitting behavior of a macroscopic sample could be described in terms of an elementary pitting probability associated with a small area of material, with each small area of material acting independently (1). In any material system, sufficiently small sample sizes will not follow macroscopic pit initiation behavior. Thus, the model should break down when the sample does not contain a statistically significant population of pit initiation sites. For example, if pit initiation in an stainless steel is linked to the behavior MnS inclusions, then the elementary area would have to contain a statistically significant population of inclusions in order to predict the behavior of larger samples (a sample devoid of inclusions could not possibly be used to predict the behavior of a macroscopic sample containing a large distribution of such phases). For high-purity aluminum, the density of sites is apparently quite low (e.g., $10^3/cm^2$ (19)) and thus the statistical model would break down for samples that are relatively large (e.g., $10^{-2}cm^2$ to contain an average of 10 sites). Importantly, it should be noted that by testing a sufficiently large number of small-electrode samples it should be possible to recover the behavior for larger electrodes, independent of nucleation mechanism. However, in the present work, we only test a limited number of samples at each condition (nominally 10 electrodes). Additionally, no significant overlap in pitting potential distributions is observed for the various electrode areas tested.

B1.3. Statistics-Based Description of Pit Initiation

The use of statistics to describe pitting behavior has been addressed extensively in the literature (1-3, 21-30) and review articles are available (3, 21). The mathematical treatment used here is adopted primarily from the work performed on stainless steel by Shibata(2) and Baroux(1). The goal of this development is to incorporate the area dependency formulated by Baroux into the statistical framework developed by Shibata.

Consider an elementary pitting probability, π (μm^{-2}), which we define as the probability that an arbitrary, small area of material, δA (μm^2), will pit during a time interval δt. Given that all δA behave independently, it follows that:

$$P_{\delta t} = (1 - \pi \delta A)^{A/\delta A} \tag{B1}$$

$$\lim_{\delta A \to 0} (1 - \pi \delta A)^{A/\delta A} = \exp(-\pi A) \tag{B2}$$

$$\pi = -\frac{1}{A} \ln P_{\delta t} \tag{B3}$$

where $P_{\delta t}$ is the probability that a macroscopic sample of area A will survive without pitting during the time interval δt. From Shibata's work, we can define a pit germination rate, λ ($s^{-1}\mu m^{-2}$), as the rate of change in the pitting probability:

$$\lambda(t) = \frac{d\pi}{dt} \tag{B4}$$

$$\lambda(t) = -\frac{1}{A} \frac{d \ln(P_{\delta t})}{dt} \tag{B5}$$

Shibata originally designated λ(t) as the pit germination rate for an arbitrarily sized sample with the units of s^{-1} (2); here we have normalized the parameter by dividing by *A*. This normalization can only be valid if the same initiation phenomena control pitting independent of electrode area. To determine the probability of a sample surviving for a length of time, *t*, it is necessary to rearrange and integrate Equation B5, yielding:

$$P(t) = \exp\left\{ - A\int_0^t \lambda(t)dt \right\} \tag{B6}$$

Thus, if λ(t) is known, it is possible to predict the survival probability for an arbitrary sized sample. The usual manner in which λ(t) is determined is to plot the survival probability for a population of samples against the induction time, τ, at a constant electrode potential. If λ is independent of *t*, then it can be determined by taking the negative slope of the *ln(P)* vs. τ plot. In such experiments, the survival probability is estimated as:

$$P(t) = 1 - \frac{n}{N+1} \tag{B7}$$

where *n* is the number of pitted samples at time *t* and *N* is the total number of samples in the population. Shibata extended this statistical treatment of pitting behavior to include potentiodynamic data, e.g., pitting potentials, by utilizing the relationship between applied potential; E_a (V); scan rate, ν ($V \cdot s^{-1}$); and time:

$$E_a = \nu t + E_1 \tag{B8}$$

$$dt = \frac{1}{\nu} dE_a \tag{B9}$$

Substituting Equation B9 into Equation B6 and changing the variable of integration from time to potential yields:

$$P(E_{pit} > E_2) = \exp\left\{ - \frac{A}{\nu}\int_{E_1}^{E_2} \lambda(E)dE \right\} \tag{B10}$$

Equation B10 is the cumulative probability that a sample will survive when the potential is scanned from E_1 to E_2. Thus, we can derive a cumulative distribution function (CDF) and a probability density function (PDF) for the pitting potential, E_{PIT} (V), based on Equation B10.

$$CDF(E_{pit}) = 1 - \exp\left\{ - \frac{A}{\nu}\int_{E_1}^{E_2} \lambda(E)dE \right\} \tag{B11}$$

$$PDF(E_{pit}) = \frac{d}{dE} CDF(E_{pit}) = \frac{A}{\nu}\lambda(E)\exp\left\{ - \frac{A}{\nu}\int_{E1}^{E2} \lambda(E)dE \right\} \tag{B12}$$

In order to utilize Equations B11 and B12 it is necessary to know the relationship between germination rate and applied potential. Baroux(1) and Heusler(28) measured exponential dependencies while Shibata(2, 3) measured both exponential and linear

dependence of germination rate on potential. The forms for the exponential and linear dependencies are given in Equations B13 and B14 respectively.

$$\lambda(E) = A\alpha(E - E_o) \quad \text{(B13)}$$

$$\lambda(E) = A\beta\exp(\gamma E) \quad \text{(B14)}$$

The following constants appear in Equations B13 and B14: β ($s^{-1}\cdot\mu m^{-2}$), γ (V^{-1}), α ($s^{-1}\cdot\mu m^{-2}\cdot V^{-1}$) and E_0 (V). Equations B13 and B14 can be inserted into Equations B11 and B12 in order to define the probability distributions in terms of the aforementioned constants. Once this substitution is made, the equations can be solved for the average pitting potential ($\bar{E}_{pit}$) in terms of the scan rate and the sample area by setting $CDF(E_{pit}) = 0.5$:

$$\overline{E}_{pit} = \left(\frac{1.386\,\nu}{A\alpha}\right)^{1/2} + E_o \quad \text{(B15)}$$

$$\overline{E}_{pit} = \frac{1}{\gamma}\ln\left[\frac{0.693\nu\gamma}{A\beta} + \exp(\gamma_{E1})\right] \quad \text{(B16.a)}$$

$$\overline{E}_{pit} = \frac{1}{\gamma}\ln\left[\frac{0.693\nu\gamma}{A\beta} + \exp(\gamma_{E_{crit}})\right] \quad \text{(B16.b)}$$

Equation B15 predicts that $\bar{E}_{pit}$ varies as $\nu^{1/2}$ and $A^{-1/2}$ and results from assuming a linear dependence of λ on E. Equation B16 predicts that $\bar{E}_{pit}$ varies as $log(\nu)$ and $log(A^{-1})$ and results from assuming an exponential dependence of λ on E. In Equation B16.a, the E_1 term represents the lowest potential probed in a potential scan; however, at potentials below the pitting potential, the germination rate will be zero and Equation B16.a will have an error that is a function of the choice of E_1. Thus in Equation B16.b, E_1 is replaced with E_{crit} which is defined as a critical potential, below which the germination rate is zero, and above which the germination rate is given by Equation B14. E_{crit} can most simply be thought of as the minimum observable pitting potential. In Shibata's work (2), E_o was also defined as a minimum pitting potential. Here we differentiate these parameters, because different values can be obtained for E_o and E_{crit} by fitting a data set with Equations B15 and B16.b, respectively.

Shibata also derived relationships for $\bar{E}_{pit}$, but made the simplifying assumption that the probability function (Equation 12) is symmetric. Such an assumption leads to Equations B17 and B18 rather than Equations B15 and B16, respectively.

$$\overline{E}_{pit} = \left(\frac{\nu}{A\alpha}\right)^{1/2} + E_o \quad \text{(B17)}$$

$$\overline{E}_{pit} = \frac{1}{\gamma}\ln\left(\frac{\nu\gamma}{A\beta}\right) \quad \text{(B18)}$$

Equations B15 and B17 differ only by the constant 1.386 which can be accommodated by the α parameter when the equation is fit to experimental data and thus should not impact analysis. Equations B16 and B18 differ by the constant 0.693, which can similarly be accommodated by the β parameter. However, Equation B16 also

contains the term $exp(\gamma E_{crit})$ which does not appear in Equation B18. In Shibata's work (2), E_1 is defined as the starting potential in the potentiodynamic scan experiment. If the germination rate at E_1 is effectively zero, then this term will drop out of the equation. However, here we replace E_1 with E_{crit}, and the term cannot be dropped without significantly altering the form of the probability distribution. The impact of this distinction will become clear when experimental data are fit to these equations later in this paper.

B2. Experimental

Aluminum electrodes were prepared from Al wires ranging from 5 μm to 500 μm in diameter. All of the wires were purchased from Alfa Aesar and have a reported purity of 99.99% except for the 5 μm wire, which is 99.95% pure. The wires were coated with a cathodic electrophoretic paint (PPG part #ED5050B) by polarizing the wire in the paint at a potential of –15 V to –20 V vs. a platinized niobium mesh counter electrode for 120 seconds. The coating was cured in an oven at approximately 77°C for 1800 seconds. The electrophoretic paint is used because of its excellent adhesion to the metal surface, which minimized crevice corrosion at the wire edge. The coated wires were mounted in epoxy to provide mechanical support for subsequent polishing and testing. Both single wire electrodes and 10-wire electrode arrays were constructed. Each electrode was wet polished mechanically to 4000 grit SiC followed by 0.3 μm alumina. Mechanical polishing was followed by washing with a mild laboratory soap (Liquinox™) and copious rinsing in deionized H_2O.

The last electrode preparation step was electropolishing in a perchloric-acid/methanol bath. The procedure was adopted from similar procedures found in the literature that have been used to prepare aluminum electrodes (20, 31). In this work, polishing parameters were adjusted to give a reproducibly flat and featureless (under optical microscopy) surface finish on wires with minimal removal of material. In general, only a few microns of material were removed during the electropolish. This is a critical factor when using small wire diameters to avoid generating a high aspect ratio electrode geometry. The electropolish bath was a mixture of 75% methanol, 20% perchloric acid and 5% glycerol and had a total volume of 125 ml. The bath was cooled to 0°C using a secondary bath of dry ice and methanol and the temperatures of both baths were monitored during electropolishing. Samples were polarized to 10 V vs. a platinum wire counter electrode for 120 seconds to 210 seconds depending on the electrode size. In general, smaller electrodes were polished for shorter times in order to minimize the amount of material loss and subsequent development of a recessed geometry. Larger electrodes tended to retain more embedded polishing media from the mechanical polishing step and required longer polishing times to effectively remove these contaminants. Electropolished samples were rinsed in room temperature deionized water, blown dry with N_2, then stored under ambient conditions for at least 24 hours prior to testing.

Electrochemical testing was performed in a 5-neck glass flask at a constant temperature of 25±0.2°C that was maintained using a temperature controlled water bath. The sample was immersed into 1 liter of deionized water and the open circuit was monitored. After 1800 seconds, 100 ml of concentrated NaCl solution was added to the flask to bring the Cl^- concentration to the desired level and the open circuit potential was monitored for an additional 1800 seconds. For the experiments performed in 5 M NaCl,

the sample was transferred from deionized H_2O to 1 liter of 5 M NaCl after 1800 seconds instead of using a NaCl concentrate solution. After the 3600 seconds (total) of open circuit exposure, the potential was ramped from the open circuit potential (E_{oc}) towards more noble potentials at a constant scan rate until the sample pitted and the current exceeded a threshold value. The threshold current was typically set to 0.2 μA, although the threshold was raised to 0.5 μA for some experiments (e.g., large area, high chloride concentration) due to high passive currents. A saturated calomel electrode (SCE) was used in all experiments and was contained in a glass lugin that terminated at a Vicor™ tip. Single wires were tested using a Gamry Instruments FAS-1 potentiostat. Multi-wire electrodes were tested using a Scribner Associates Model 900 Multi-Microelectrode Analyzer or a Perkin Elmer Model VMP Multi-Potentiostat.

B3. Results

In this work, the pitting behavior of the aluminum electrodes is quantified in terms of E_{pit} distributions and $\bar{E}_{pit}$ values. Ideally, we would like E_{pit} to represent the potential where a pit first initiates. However, some extent of pit growth must occur before the pitting current becomes resolvable. The threshold current used in this work, 0.2 μA, provides one metric for judging when a pit has initiated. A second metric is the first resolvable deviation from passive behavior. However, several experimental limitations make this an inconsistent metric. Firstly, the minimal resolvable current spike is a function of the passive current density and thus the sample area. It is not possible to examine the data from a 500 μm diameter wire with the same resolution obtained from a 5 μm diameter wire (passive current differs by a factor of 10^4). Secondly, the scan rates used in the testing cover 4 orders of magnitude, and, consequently, the data acquisition rates differ significantly from experiment to experiment. Thus, the choice of experimental parameters may dictate the time-scale of detectable events. Using the first detectable peak and the threshold current as bounds on E_{pit}, a comparison can be made to determine if the choice of analysis technique affects the $\bar{E}_{pit}$ values. Figure B1 shows a plot of $\bar{E}_{pit}$ values from the two techniques. If the values were identical, a straight line with a slope of 1 could be drawn through the points. The actual data fall very close to the ideal case, indicating that the values reported in this work are not overly sensitive to the analysis technique used. Based on this result, all subsequent E_{pit} values reported here were determined using the threshold current to identify pit initiation.

The effect of electrode area on $\bar{E}_{pit}$ was measured in 50 mM NaCl at 25°C and at a scan rate of 1.67e-4 $V \cdot s^{-1}$. The resulting average pitting potentials are plotted in Figure B2. Attempts were made to fit the $\bar{E}_{pit}$ data to an $A^{-1/2}$ relationship (Equation B15) and to a $log(A^{-1})$ relationship (Equations B16.b and B18). The $log(A^{-1})$ relationship appears to be a better fit to the experimental data. A $log(A^{-1})$ relationship was reported by Burnstein (32) for pitting of stainless steel and, similarly, the data from Böhni's work on stainless steels (33) can be fit to a $log(A^{-1})$ equation. In contrast, Shibata presents data from 304 stainless steel that shows a good fit to the $A^{-1/2}$ relationship (2). This apparent discrepancy will be addressed further in the discussion section of this paper.

The pitting behavior of 99.99 Al as a function of chloride concentration and scan rate was examined in detail only for the 125 μm and 500 μm diameter wires (1.2e-4 and 2.0e-3 cm^2 respectively). The average pitting potentials are shown versus scan rate for Cl^- concentrations of 0.005 M, 0.05 M and 0.5 M in Figures B3 and B4. Efforts were made to determine if any of the relationships (Equations B15-B18) could provide a

consistent fit to these data. The fit of the inverse square root relationship (Equation B15) to the 125 μm wire data appears to be very poor (Figure B3.a.) while the fit to the 500 μm wire data is quite good (Figure B4.a.). In contrast, the fit of Shibata's logarithmic relationship (Equation B18) to the 125 μm wire data appears satisfactory (Figure B3.b.) although the fit to the 500 μm wire data is poor (Figure B4.b.). Finally, the fit of the logarithmic relationship derived here (Equation B16.b) to both the 125 μm data (Figure B3.c.) and the 500 μm data (Figure B4.c.) is very good. Figure B4.c. also shows data points for the 500 μm wire tested in 5 M NaCl. No equations were fit to these data because $\bar{E}_{pit}$ appeared to be relatively independent of scan rate for this concentration of chloride. The 500 μm wires were also tested in 0.001 M and 5e-4 M NaCl (Figure B5). There was significant scatter in the $\bar{E}_{pit}$ values recorded in these dilute environments; such that only the simple form of the logarithmic relationship (Equation B18) could sensibly be fit to these data. The constants determined from all of the data fitting are given in Table I.

B4. Discussion

B4.1. Defining the Scan Rate and Area Dependencies of $\bar{E}_{pit}$

The data sets measured in this work (and fit to Equation B16.b) show that $\bar{E}_{pit}$ varies as *log* (ν) and *log* (A^{-1}) (Figures B3.c and B4.c). These relationships result from assuming that λ is an exponential function of *E* (Equation B14). Baroux reported an exponential dependence of λ on *E* for stainless steel (1), although Shibata concluded that λ is linearly dependent on *E* for a similar material system (2, 3). A linear dependence of λ on *E* results in a $\nu^{1/2}$ dependence of $\bar{E}_{pit}$ (Equation B17) (3).

Independent of the material system under study, the relationship between λ and *E* must be consistent with the pit initiation mechanism. Chemical and electrochemical mechanisms (i.e., activated processes) such as field assisted adsorption of Cl^- (34) can be invoked to rationalize an exponential relationship (i.e., Equation B14). In contrast, non-electrochemical mechanisms such as breakdown due to mechanical stress (35, 36) or electrostriction pressure (37) have been invoked to explain a linear relationship (i.e., Equation B13). Interestingly, MacDonald provided theoretical support for $\nu^{1/2}$ dependence of $\bar{E}_{pit}$ based on the point defect model for pit initiation (38). In his derivation, however, the condition of slow scan rate (which implies pitting potentials close to E_{crit}) was imposed in order to simplify an exponential relationship to a square root relationship. This model, therefore, applies to experimental conditions that could generate the appearance of a $\nu^{1/2}$ relationship when in fact the relationship is actually *log* (ν) (*see below*).

We propose that the reported square root dependence of $\bar{E}_{pit}$ on scan rate may be due to the choice of experimental conditions (e.g., slow scan rate or large surface area) where *log*(ν) behavior can be incorrectly fit to a $\nu^{1/2}$ relationship. In terms of germination rate, the observed behavior would be the result of measuring an exponential process over a small potential range that is close to E_{crit}, making the germination dependency appear to be linear. We can test this proposition by using Equation B16.b to simulate relationships between $\bar{E}_{pit}$, ν and *A* as we vary ν and *A*. Constants extracted from the pitting behavior of 125 μm wires in 0.05 M NaCl were used in running the simulations.

Figure B6 shows the effect of electrode area on the relationship between $\bar{E}_{pit}$ and ν. In Figure B6.a, the data are fit to Equation B18 and good fits are obtained when the surface area is less than about 10^4 μm^2. For larger areas, a good fit is not obtained. Thus, although a logarithmic dependence of $\bar{E}_{pit}$ on ν (Equation B16.b) was used to generate the plots, the logarithmic relationship (as formulated by Shibata) fails to accurately fit the data. In Figure B6.b, the data are plotted vs. $\nu^{1/2}$ and fit to Equation B15. Good fits are obtained for electrode areas larger than about 10^6 μm^2 and poor fits for smaller areas. Thus, the square root relationship (Equation B15) provides a better fit than the logarithmic relationship (Equation B18) for large area electrodes.

Figure B7 shows the effect of scan rate on the relationship between $\bar{E}_{pit}$ and A. A good fit to a $log(A^{-1})$ relationship (i.e., Equation B18) is obtained for very fast scan rates (e.g., 10 to 100 $mV \cdot s^{-1}$) but slower scan rates result in a poor fit (Figure B7.a). In contrast, a good fit to a $A^{-1/2}$ relationship is obtained at slow scan rates (i.e., less than 10 $mV \cdot s^{-1}$) with faster scan rates yielding a poor fit (Figure B7.b).

The preceding analyses show that slow scan rates and large electrode areas tend to result in $\bar{E}_{pit}$ data that vary as $\nu^{1/2}$ and $A^{-1/2}$ (Equation B15). Fast scan rates and small electrode areas tend to result in $\bar{E}_{pit}$ data that vary as $log(\nu)$ and $log(A^{-1})$ (Equation B18). It is the absence of a critical potential term in Equation B18 that leads to the poor fits for large A and slow ν. For all of the simulations, the relative goodness of these fits is an artifact from the choice of the simulated experimental conditions –clearly all of the simulated responses actually have $log(\nu)$ and $log(A^{-1})$ dependencies on $\bar{E}_{pit}$, since they were generated using Equation B16.b. This exercise is intended to demonstrate how incorrect relationships could possibly be assigned to experimental data. Thus, we suggest that the literature data could be reconciled with Equation B16.b, implying an exponential dependence of λ on E for all of the systems reviewed. It should be noted that the specific ranges of ν and A that lead to incorrectly fitting the $\bar{E}_{pit}$ data will be sensitive to the system under study. As α (Equation B13) or β (Equation B14) increases, smaller A and larger ν will be required to observe the purely logarithmic behavior.

B4.2. Testing the Homogeneous Nucleation Hypothesis: Predicting area dependence of $\bar{E}_{pit}$

If the relationship between $\bar{E}_{pit}$ and A is a continuous, smooth function, then the same features of the metal/metal oxide system responsible for pit initiation must be represented on all of the electrodes, independent of area. The increase in $\bar{E}_{pit}$ with decreasing area would not be due to the decreased likelihood of sampling specific, distributed defect structures as the sample size decreases. The $\bar{E}_{pit}$ vs. A data shown in Figure B2 can be fit to a continuous smooth function (Equation B16.b), supporting the notion that the same features control pit initiation on electrodes ranging from 10^5 down to 20 μm^2. This implies that within 20 μm^2 a statistically significant population of initiation sites exists. Furthermore, the locations of pits on the larger samples are randomly determined, because there are no microstructural or chemical variations that pin pitting behavior with a density less than one site every few square microns. These notions are at odds with the "weak link" concept of pit initiation, in which a pit initiates at a specific site having properties that enhance its susceptibility.

The opposite conclusion was reached by Burstein when a similar trend was observed between $\bar{E}_{pit}$ and $\log(A^{-1})$ on 316 stainless steel (32). Originally, the increase in $\bar{E}_{pit}$ was attributed to the drawing process used to generate fine wire stainless steel

specimens. It was hypothesized that the drawing process tended to crush MnS inclusions resulting in decreasing particle size as area was decreased. Later, specialized specimens were prepared by machining which maintained the original sulfide distribution. Again, $\bar{E}_{pit}$ was observed to scale with $A^{-1/2}$. In the latter study, it was postulated that the probability of encountering a large inclusion decreased with sample size and that the propensity for initiation scaled with particle size. This argument makes intuitive sense when the metal contains discrete flaws, e.g., 316SS. However, this theory requires that the E_{pit} vs. particle size relationship and the particle distribution combine to yield the well-defined relationship between $\bar{E}_{pit}$ and $\log(A^{-1})$. While this is possible, it has not been conclusively demonstrated.

A better test of our original hypothesis than simply measuring the area dependence of pitting potential is to attempt to predict the area dependence using data from a single electrode size. If the behavior of a larger electrode can be used to predict the behavior of smaller electrodes, then the same initiation sites should be operative on both. If the large electrode behavior is pinned because it, on average, contains a certain population of defects, then it should not be possible to predict the behavior of a smaller electrode that does not contain the same defects. Equation 16 was fit to data from the 125 μm wires, then was used in an attempt to predict the trend in $\bar{E}_{pit}$ vs. A (Figure B8). In these analyses, both the $A^{-1/2}$ and the $log(A^{-1})$ dependencies of $\bar{E}_{pit}$ were used. The $A^{-1/2}$ relationship does not yield a good prediction. The $log(A^{-1})$ relationship, however, does yield good agreement between predicted and measured $\bar{E}_{pit}$ values. This result supports the homogeneous nucleation hypothesis and adds credence to the conclusion that λ varies exponentially with E.

A similar test of the hypothesis was performed using data from the 500 μm wires (Figure B9). Here, neither the $A^{-1/2}$ nor the $log\,(A^{-1})$ dependence of $\bar{E}_{pit}$ yielded a good prediction of $\bar{E}_{pit}$ vs. A. This result indicates that there are processes occurring on the 500 μm electrodes that are not controlling behavior on the smaller electrodes. According to our original hypothesis, pit initiation on 500 μm electrodes is, therefore, heterogeneous. From these data alone, it is not possible to know if the manufacturing processes used on the various diameter wires is responsible for the enhanced susceptibility on the larger electrodes. To address this concern, future experiments will be performed where the behavior of aluminum single crystals will be characterized as a function of exposure area.

B4.3. Intrinsic and defect-driven pitting on Al wires

The preceding discussion supports the notion that pit initiation on 99.99 Al wires has both homogeneous and heterogeneous contributions; with the caveat that homogeneous refers to a size scale of several square microns. Pit initiation on electrodes between 5 μm and 125 μm in diameter (19 μm^2 to12,300 μm^2) is governed by a homogeneous nucleation process. All of the behavior over this size range can be adequately described by Equations B14 and B16 with a single set of values for the parameters γ and β; that is γ,β ≠ f(A). Thus, on these samples there cannot be heterogeneous features that control pitting behavior that have a density less than about 0.2 μm^{-2} – arbitrarily assuming an average of 4 defects on the smallest electrode tested, 19 μm^2. Otherwise, there would be a discontinuity in the data over this size range. Okada suggested a possible homogeneous nucleation process that is based on local solution perturbations in ionic concentration and electric field that autocatalytically grow and lead to local oxide breakdown (39). The location of the breakdown is randomly

determined and not correlated with a specific weakness in the oxide film. We can also envision nucleation processes that are tied to a local critical concentration of some species at the film/solution interface (e.g., Cl^-), within the film (e.g., Cl^-, metal vacancies), or at the metal/film interface (e.g., Cl^-, vacancies, H_2). The formation of the nucleus may be a statistically unlikely event that requires overcoming either a large energy barrier or a series of energy barriers.

A potential source of pit localization that has not been addressed to this point is grain boundaries. It is likely that the grain size is different on all of the electrodes used in this work. It is even conceivable that the average grain misorientation could be a function of the electrode size. While these parameters were not quantified in this study, all of the wires are polycrystalline and do contain boundaries. If the pitting behavior of microelectrodes is due to differences in grain boundary susceptibility, then it might be expected that macroscopic single crystals of aluminum would have elevated pitting potentials compared to polycrystalline samples of the same purity. However, Yu and Natishan reported E_{pit} of electropolished Al single crystals to be in the range of -0.6 V_{SCE} to -0.7 V_{SCE}, depending on crystallographic orientation (20). These pitting potentials are similar to what we observe for our large (500 μm) polycrystalline electrodes, and are quite dissimilar from the elevated values that we observe for microelectrodes. Furthermore, if grain boundaries were responsible for pit nucleation on the microelectrodes studied here, then the relationship between $\bar{E}_{pit}$ and A would be a fortuitous result of grain boundary susceptibility being coupled in a systematic way to electrode area. Although such a relationship is not likely, the current data set cannot completely rule out such a coincidence. Ongoing work on single crystals will be used to resolve this issue.

Although pit nucleation appears to be homogeneous for electrodes smaller than 125 μm, a heterogeneous mechanism appears to be operative on 500 μm electrodes. Our inability to reconcile the germination behavior on 125 μm and 500 μm electrodes by area normalization indicates the presence of a defect distribution on larger electrodes that is absent on smaller electrodes. This observation forms the basis for making a prediction of a defect density that controls pitting behavior on macroscopic 99.99 Al electrodes. If we define the density of a particular defect type to be χ (sites-μm^{-2}), then the probability that a sample of area A (μm^2) contains at least one defect is given by:

$$P(\textit{defect in } A) = 1 - \exp(-A\chi) \qquad \text{(B19)}$$

Equation B19 was used to predict the probability of both 125 μm and 500 μm electrodes containing a defect as a function of defect density (Figure B10). There is a range of defect density in which the probability of the 125 μm electrode containing a defect is low and the probability of the 500 μm electrode containing a defect is high. If we assume that having a defect on 80% of the large electrodes will dominate their behavior, but having a defect on only 20% of the small electrodes will not dominate their behavior, then the defect density can be estimated using Figure B10. These bounds lead to a defect density ranging from 8e-6 μm^{-2} to 2e-5 μm^{-2} (800 to 2000 defects per cm^2). This defect density is on the same order of magnitude reported by White for electroactive sites on 99.95 and 99.9995 Al (19). Although such agreement does not conclusively identify electroactive sites as the defect type responsible for pit initiaiton on macroscopic studies, it is

compelling that the same defect density can be reached by two studies taking entirely different approaches.

B4.4. Cl dependence of $\bar{E}_{pit}$

A logarithmic relationship between Cl^- and E_{pit} has been reported in the literature and often is described by the following equation.

$$E_{pit} = A - B\log[Cl^-], \tag{B20}$$

where *A* and *B* are constants. Typical literature values for *B* range from 0.05V to 0.13V (40). The data from Figures 3 through 5 were used to generate plots of $\bar{E}_{pit}$ vs. [Cl^-] for both 125 μm and 500 μm electrodes (see Figures 11 and 12, respectively). In Figure B12, the relationship is plotted for $\bar{E}_{pit}$ determined at 1.67e-4 $V \cdot s^{-1}$ (B12.a) and 1.67e-3 $V \cdot s^{-1}$ (B12.b). At the slower scan rate the *log* [Cl^-] fit does not accommodate the highest Cl^- concentration, demonstrating the scan rate sensitivity of this relationship. Nevertheless, *B* values were calculated for both electrode sizes for ν=1.67e-4 $V \cdot s^{-1}$. The 125 μm wires yielded a value of 0.36 V_{SCE}; the 500 μm wires yielded values of 0.51 V_{SCE} for [Cl^-] ≤ 0.005 M and 0.11 for [Cl^-] ≥ 0.005 M. The 500 μm data may indicate a change in the pitting mechanism as a function of the Cl^- concentration. At lower concentrations, the *B* value is similar to that found on the 125 μm electrodes, whereas at higher concentrations the *B* value is considerably lower. This may be an indication that the heterogeneous pit initiation process on the 500 μm electrode is only operative over a specific range of Cl^- concentrations, although this conjecture remains speculative barring further investigation. Also of note, the *B* value for the 500 μm electrodes in higher Cl^- is more aligned with literature values than those found in low Cl^- or from the 125 μm data.

Another metric that has been used to describe the [Cl^-] dependence of pit initiation behavior is induction time, τ. Plots of *log* (τ^{-1}) vs. *log* [Cl^-] have been used to generate estimates of a reaction order for pit initiation in aluminum (41-44). If τ is taken to be inversely proportional to the rate of reaction, then the following rate equation can be written:

$$\frac{1}{\tau} = k[Al]^m[Cl^-]^n \tag{B21}$$

where *k*, *m* and *n* are constants. Rearranging yields:

$$\ln\frac{1}{\tau} = \ln k + m\ln[Al] + n\ln[Cl^-]. \tag{B22}$$

Thus, the slope of the *log* (τ^{-1}) vs. *log* [Cl^-] plot is the reaction order in [Cl^-]. Although τ vs. [Cl^-] was not measured in the present work, we can calculate this relationship from the knowledge of λ vs. *E* (Equation B14). In Equation B6, *P(t)* will equal 0.5 when the integration range is from 0 to τ_{ave} (the average induction time for those conditions). Thus, substituting Equation B14 into Equation B6 leads to the following relationship between τ_{ave} and *E*:

$$\tau_{ave} = \frac{\ln 0.5}{\beta \exp(\gamma E)}. \qquad \text{(B23)}$$

Because β and γ are known for various [Cl^-] (Table I), it is possible to calculate τ for a range of [Cl^-] and *E*. The calculated relationships are shown in Figures B13 and B14 for 125 μm and 500 μm electrodes respectively. A significant result from this exercise is the observed dependence of *n* on *E* (Figure B14), implying that the values reported for *n* in the literature could be an artifact of the potential at which the induction time testing was performed. This raises a serious concern with ascribing physical significance to the value of *n*. There may also be cases, however, where *n* is not a strong function of applied potential. Figure B14.b suggests the possibility that *n* is somewhat independent of *E* for high Cl^- concentrations, though the low density of data makes such a conclusion tenuous. Indeed, the same data can be used to reach the opposite conclusion (Figure 14.a).

Independent of *E*, the 500 μm data do show a transition in *n* as a function of Cl^- concentration. At approximately 0.005 M the slope of the *log* (τ^{-1}) vs. *log* [Cl^-] plot changes abruptly, possibly indicating a change in pitting mechanism. Not surprisingly, this discontinuity is observed at the same Cl^- concentration where the $\bar{E}_{pit}$ vs. *log* [Cl^-] plot changes slope (Figure B12). Similarly, the relationship between τ and [Cl^-] has been observed to be a strong function of chloride concentration by both Foroulis (42) and Bogar (44). Literature values of *n* for pure Al (42) and Al 1199 (44) have been reported in the range of 0.1 to 2.5 respectively. Here we calculate values ranging from about 0 to 2. Values greater than 2 can be calculated by allowing pitting to occur at very low potentials (e.g., -1 V_{SCE}) and values less than 0 can be calculated for very high potentials (e.g., 1.5 V_{SCE}). Despite the limitations on the interpretation of *n*, the reported values and those found here appear to fall within a consistent range.

B4.5. Bounding Epit values

Although E_{pit} for pure aluminum is a strong function of *A* (Figure 2), ν (Figures 3-5) and [Cl^-] (Figures B11 and B12), it is worthwhile to consider not only how $\bar{E}_{pit}$ varies over this phase space but how $\bar{E}_{pit}$ may be bounded. In this section, we suggest experimental conditions that should coincide with either minimum or maximum pitting potentials.

The 500 μm wire data (Figure B4) indicate that for each Cl^- concentration the curves asymptotically approach a limiting value as ν is reduced. This behavior suggests that the lower limit on E_{pit} will be reached at sufficiently slow ν at which E_{pit} becomes independent of ν. Such behavior was demonstrated by measuring the E_{pit} behavior in 5 M NaCl (Figure B4.c). Here $\bar{E}_{pit}$ does not increase with increasing ν. In theory, the same behavior would be observed for other electrolyte concentrations at very low ν. However, very small values of ν may lead to oxide aging during the potential scan and yield inconsistent pitting behavior. Thus, for a given electrode size and electrolyte combination, observing the asymptotic behavior may not be possible. For low concentrations, therefore, it seems that larger electrodes may be needed to observe the minimum pitting potential. It may also be necessary to invoke induction time testing at constant potential in order to avoid the oxide aging during the potential scan.

A maximum value on E_{pit} should be observed when the germination rate is infinite – i.e., when the oxide becomes uniformly unstable. This implies that the instability condition must occur independent of specific interactions with the environment, since any

interaction would require a finite time to occur. Thus, the maximum should occur when E_{pit} becomes independent of electrolyte concentration. Earlier, we discussed the apparent reaction order, *n*, for pit initiation (Equations B21 and B22). Independent of mechanistic interpretations, *n* is a measure of the magnitude of the dependence of E_{pit} on $[Cl^-]$. Thus, if *n* is a function of potential and if a potential exists where $n = 0$, then this potential should be an upper bound on E_{pit}. The relationship between *n* and *E* for 125 μm wires (Figure B13) predicts an upper limit of 1.33 V_{SCE} for $\bar{E}_{pit}$. It should be noted that the average values of pitting potential were used in this analysis; a true maximum E_{pit} would have to be determined through an analysis of maximum pitting potentials observed as a function of $[Cl^-]$. A limiting E_{pit} value in the 1+ V range could indicate that dielectric breakdown of the oxide is the limiting germination mechanism (45).

B4.6. Implications of Experimental Conditions When Characterizing Pitting Behavior

The mapping out of the *A*, $[Cl^-]$ and ν phase space for pit initiation behavior in this work suggests that careful selection of these parameters is critical when undertaking a study of pit initiation processes. If the objective is to find a lower bound on E_{pit}, then classical, large area (e.g., 1 cm^2) electrodes may be appropriate. Even in this case, though, care should be taken to understand the dependence of E_{pit} on ν such that a true minimum can be estimated.

The study of pitting mechanisms (in particular, potential-dependent rate phenomena) may require making measurements of E_{pit} significantly removed from E_{crit}. It would appear that this could be done for any reasonable combination of electrode area and electrolyte aggressiveness by choosing an appropriate ν. Unfortunately, practical bounds exist for the values of ν that can be used. At very low ν the sample behavior may change as a function of test duration. In an extreme case a negative slope between E_{pit} and ν could result and such a phenomenon has been reported in the literature (1). Very high values of ν require changing the applied potential very rapidly. Because most modern potentiostats are digital, high ν can result in large potential steps during the scan. When a digital potential step is applied, the metal/oxide/electrolyte system experiences a non-equilibrium condition and failure may follow a different mechanism than in the equilibrium case. An additional problem with very high ramp rates is detecting pit initiation. Besides the obvious issue with accurately measuring E_{pit}, high ramp rates can increase the capacitive charging current and thus limit the ability to resolve pitting current. Another approach to resolving potential-dependent rate phenomena is changing the aggressiveness of the electrolyte. However, as demonstrated in this work (Figures B12 and B14), pitting mechanisms can be dependent on electrolyte concentration. Finally, it is possible to carefully select an electrode area such that pitting phenomena can be appropriately studied. This may be the most straightforward approach for studying homogeneous systems. If a system is heterogeneous, however, the number of data points to accurately quantify pitting behavior may become unmanageable as the area is decreased.

The appropriate choice of phase space for studying pit initiation will be highly dependent on the relationship between germination rate and potential. The best approach may be to parametrically determine the relationship between E_{pit} and *A*, electrolyte concentration and ν, and identify the ranges that are best suited to the particular study. When such an approach is not feasible, the data should be carefully examined to ensure

that artifacts from the choice of these parameters are not obscuring the relationships being sought.

B5. Conclusions

The pit initiation behavior observed on 99.99 Al in this study has been described by an area-independent statistical treatment for electrodes having diameters between 5 μm and 125 μm. The nucleation behavior appears to be homogeneous (as defined in this paper) for these electrode sizes. If discrete defects are causally linked to initiation on these electrodes then they must have a density of at least 0.2 μm^{-2} (i.e., 1 defect per 5 μm^2).

There exists a discontinuity in the area dependence of pitting potential for electrodes between 125 μm and 500 μm in diameter, implying that local, discrete structures contribute to the initiation behavior on the 500 μm electrodes. Based on this discontinuity, the density of defect sites is estimated to be between 8e-6 μm^{-2} and 2e-5 μm^{-2} (i.e., 1 defect per 10^5 μm^2) on 99.99Al.

An exponential dependence of germination rate on applied potential is consistent with all of the pitting potential data collected in this study and corresponds to $\bar{E}_{pit}$ varying as *log* (A^{-1}) and *log* (ν). The apparent $A^{-1/2}$ and $\nu^{1/2}$ dependencies of E_{pit} reported in the literature *may* be an artifact of making E_{pit} measurements that are close in value to a limiting or minimum E_{crit}.

Evidence has been found that the pitting potentials on 99.99 Al are bounded. A lower bound is observed when E_{pit} becomes independent of scan rate. An upper bound corresponds to the potential where pit initiation becomes independent of chloride concentration. A plausible explanation for an upper bound is dielectric breakdown of the oxide.

Small diameter Al electrodes appear to be a suitable platform for studying intentionally introduced defects. Because spatially discrete sites do not appear to be driving pit initiation, the opportunity exists to engineer defects and observe their behavior.

B6. References

1. B. Baroux, *Corrosion Science* **28**, 969-986 (1988).
2. T. Shibata, T. Takeyama, *Corrosion* **33**, 243-251 (1977).
3. T. Shibata, *Corrosion* **52**, 813-830 (1996).
4. J. R. Galvele, S. M. D. Micheli, Mechanism of Intergranular Corrosion of Aluminum-Copper Alloys, N. E. Hammer, Ed., 4th International Congress on Metallic Corrosion (NACE, 1972).
5. J. R. Scully, in *Critical Factors in Localized Corrosion, ECS PV 92-9* G. S. Frankel, R. C. Newman, Eds. (The Electrochemical Society, 1992) pp. 144-156.
6. C. Blanc, B. Lavelle, G. Mankowski, *Corrosion Science* **39**, 495-510 (1997).
7. J. Zahavi, A. Zangvil, M. Metzger, *Journal of the Electrochemical Society* **125**, 438-444 (1978).
8. K. Nisancioglu, K. Y. Davanger, Ø. Strandmyr, *Journal of the Electrochemical Society* **128**, 1523-1526 (1981).
9. R. M. Rynders, C.-H. Paik, R. Ke, R. C. Alkire, *Journal of the Electrochemical Society* **141**, 1439-1445 (1994).
10. J. O. Park, C. H. Paik, Y. H. Huang, R. C. Alkire, *Journal of the Electrochemical Society* **146**, 517-523 (1999).
11. M. A. Alodan, W. H. Smyrl, *Journal of the Electrochemical Society* **145**, 1571-1577 (1998).
12. R. G. Buchheit, J. P. Moran, G. E. Stoner, *Corrosion* **50**, 120-130 (1994).
13. R. G. Buchheit, J. P. Moran, F. D. Wall, *Corrosion* **51**, 417-428 (1995).
14. R. G. Buchheit, R. P. Grant, P. F. Hlava, B. Mckenzie, G. L. Zender, *Journal of the Electrochemical Society* **144**, 2621-2628 (1997).
15. F. D. Wall, G. E. Stoner, *Corrosion Science* **39**, 835-853 (1997).
16. G. C. Wood, W. H. Sutton, J. A. Richardson, T. N. K. Riley, A. G. Malherbe, in *NACE III* Brown, Kruger, Stahle, Argawal, Eds. (NACE, Houston, 1971) pp. 526-545.
17. G. M. Brown, K. Shimizu, K. Kobayashi, G. E. Thompson, G. C. Wood, *Corrosion Science* **34**, 2099-2104 (1993).
18. I. Serebrennikova, H. S. White, *Electrochemical and Solid-State Letters* **4**, B4-B6 (2001).
19. H. S. White, "SECM Investigations of Native Aluminum Oxide Films" (University of Utah, 2001).
20. S. Y. Yu, P. M. Natishan, in *Critical Factors in Localized Corrosion III* R. G. Kelly, G. S. Frankel, P. M. Natishan, R. C. Newman, Eds. (The Electrochemical Society, INC, Pennington, 1999), vol. 98-17, pp. 256-264.
21. C. Gabrielli, F. Huet, M. Keddam, R. Oltra, *Corrosion* **46**, 266-278 (1990).
22. N. Sato, *Journal of the Electrochemical Society* **123**, 1197-1199 (1976).
23. D. E. Williams, C. Westcott, M. Fleischmann, A Stochastic Approach to the Study of Localized Corrosion, Metallic Corrosion Vol. 2, Proc. 9th ICMC, Toronto (National Research Council of Canada, 1984).
24. D. E. Williams, C. Westcott, M. Fleischmann, *Journal of the Electrochemical Society* **132**, 1796-1804 (1985).
25. B. Wu, J. R. Scully, J. L. Hudson, A. S. Mikhailov, *Journal of the Electrochemical Society* **144**, 1614-1620 (1997).

26. T. T. Lunt, S. T. Pride, J. R. Scully, J. L. Hudson, A. S. Mikhailov, *Journal of the Electrochemical Society* **144**, 1620-1629 (1997).
27. S. T. Pride, J. R. Scully, J. L. Hudson, *Journal of the Electrochemical Society* **141**, 3028-3040 (1994).
28. R. Doelling, K. E. Heusler, *Z. Physik. Chem. NF* **139**, 39-58 (1984).
29. D. E. Williams, C. Westcott, A New Electrochemical Technique for Evaluation of Susceptibility to Pitting Corrosion, Metallic Corrosion Vol. 4, Proc. 9th ICMC, Toronto (1984).
30. D. E. Williams, C. Westcott, M. Fleischmann, *Journal of the Electrochemical Society* **132**, 1804-1811 (1985).
31. S. Murali, M. Ramachandra, K. S. S. Murthy, K. S. Raman, *Materials Characterization* **38**, 273-286 (1997).
32. G. T. Burstein, G. O. Ilevbare, *Corrosion Science* **38**, 2257-2265 (1996).
33. H. Böhni, T. Suter, A. Schreyer, *Electrochimica Acta* **40**, 1361-1368 (1995).
34. K. Videm, in *Proc. 5th International Congress on Metallic Corrosion* . (NACE, 1974) pp. 264-268.
35. D. A. Vermilyea, *Journal of the Electrochemical Society* **110**, 345-346 (1963).
36. D. H. Bradhurst, J. S. Llewelyn Leach, *Journal of the Electrochemical Society* **118**, 485-491 (1966).
37. N. Sato, *Electrochimica Acta* **16**, 1683 (1971).
38. D. D. Macdonald, *Journal of the Electrochemical Society* **144**, 1574-1581 (1997).
39. T. Okada, *Journal of the Electrochemical Society* **132**, 537-544 (1985).
40. Szklarska-Smialowska, *Pitting Corrosion of Metals* (NACE, Houston, 1986).
41. S. Dallek, R. T. Foley, *Journal of the Electrochemical Society* **123**, 1775-1778 (1976).
42. Z. A. Foroulis, M. J. Thubrikar, *Journal of the Electrochemical Society* **122**, 1296-1301 (1975).
43. T. H. Nguyen, R. T. Foley, *Journal of the Electrochemical Society* **126**, 1855-1860 (1979).
44. F. D. Bogar, R. T. Foley, *Journal of the Electrochemical Society* **119**, 462-464 (1972).
45. J. P. Sullivan, et al., in *Oxide Films* K. R. Hebert, R. S. Lillard, B. R. MacDougall, Eds. (The Electrochemical Society, Pennington, 2000) pp. 24-35.

	Equation 15		Equation 18		Equation 16		
	$\bar{E}_{pit} = \left(\frac{1.386\,\nu}{A\alpha}\right)^{1/2} + E_o$		$\bar{E}_{pit} = \frac{1}{\gamma}\ln\left(\frac{\nu\gamma}{A\beta}\right)$		$\bar{E}_{pit} = \frac{1}{\gamma}\ln\left[\frac{0.693\nu\gamma}{A\beta} + \exp\left(\gamma E_0\right)\right]$		
Experimental Conditions	α ($s^{-1}\mu m^{-2}V^{-1}$)	E_o (V)	γ (V^{-1})	β ($s^{-1}\mu m^{-2}$)	γ (V^{-1})	β ($s^{-1}\mu m^{-2}$)	E_o (V)
Epit vs. A 0.05M NaCl 0.167mV/s	4.99e-6	-0.175	--	--	5.36	1.17e-7	-0.950
Epit vs. ν 125μm 0.005M NaCl	2.12e-6	0.016	7.66	2.19e-6	7.63	2.22e-8	-0.610
Epit vs. ν 125μm 0.05M NaCl	2.67e-7	-0.486	6.66	1.70e-7	6.35	1.67e-7	-0.757
Epit vs. ν 125μm 0.5M NaCl	1.64e-6	-0.640	7.56	2.36e-6	4.47	1.47e-6	-0.679
Epit vs. ν 500μm 5e-4M NaCl	--	--	7.55	5.79e-9	--	--	--
Epit vs. ν 500μm 0.001M NaCl	--	--	9.16	2.51e-8	--	--	--
Epit vs. ν 500μm 0.005M NaCl	7.05e-8	-0.646	15.0	1.22e-5	4.79	1.50e-7	-0.610
Epit vs. ν 500μm 0.05M NaCl	1.82e-7	-0.746	22.6	0.027	17.5	1.24e-3	-0.757
Epit vs. ν 500μm 0.5M NaCl	3.50e-7	-0.817	29.1	31.0	18.9	0.032	-0.813

Table BI. Constant determined from fitting $\bar{E}_{pit}$ data.

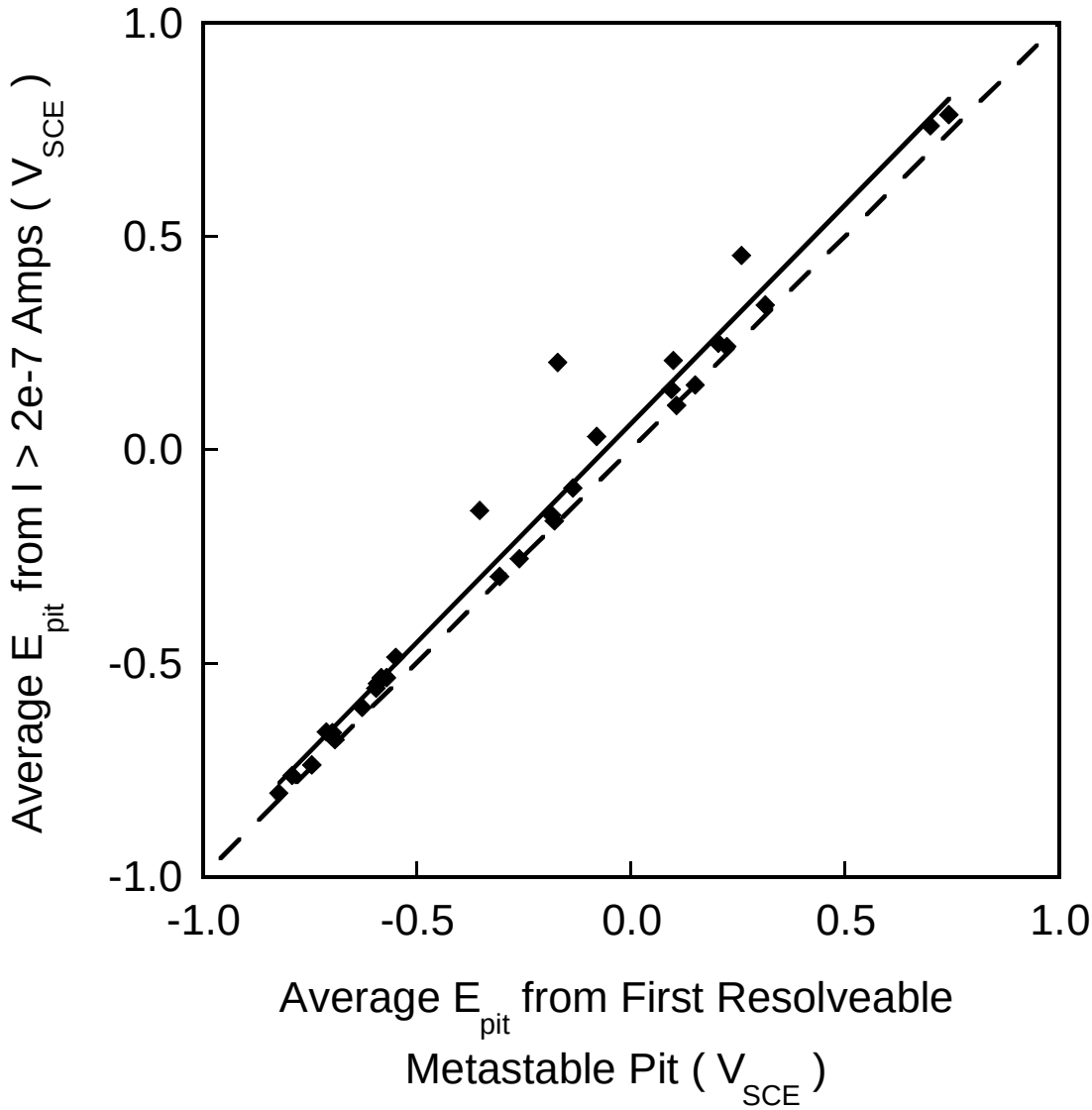

Figure B1. Comparison of *Ēpit* values determined using two analysis techniques. ◆ data values, ─ linear fit to data values, -- ideal relationship for *Ēpit* independent of analysis technique.

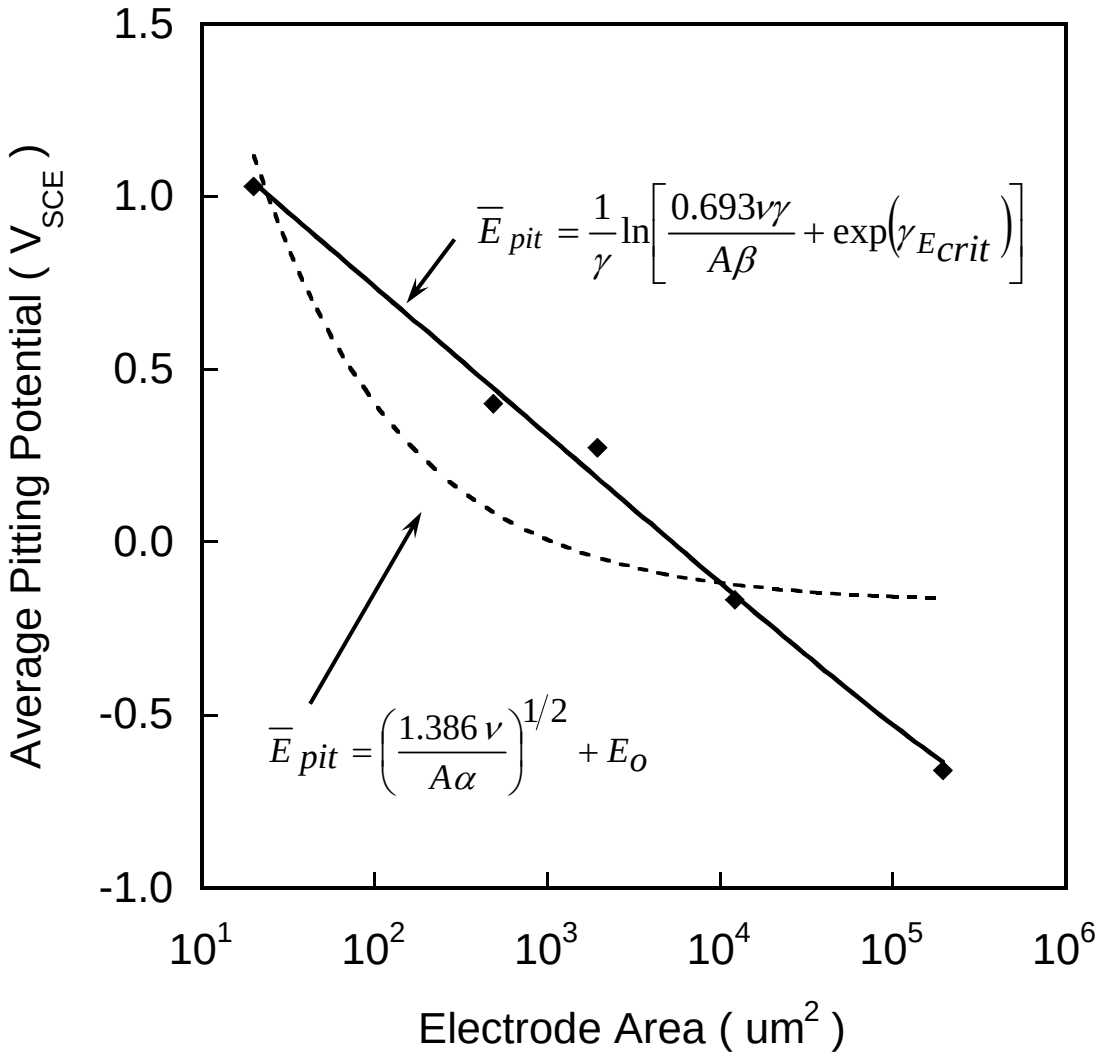

Figure B2. Pitting behavior of 99.99Al as a function of electrode area. *Ēpit* measured at a scan rate of 0.167mV/s in 50mMol NaCl, 25°C. ─ fit to Equation B16 (log A-1 dependence of *Ēpit*), ┈ fit to Equation B15 (A-1/2 dependence of *Ēpit*).

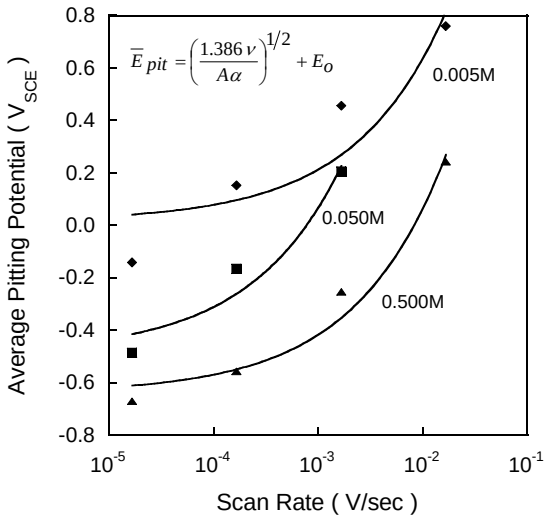

Figure B3.a

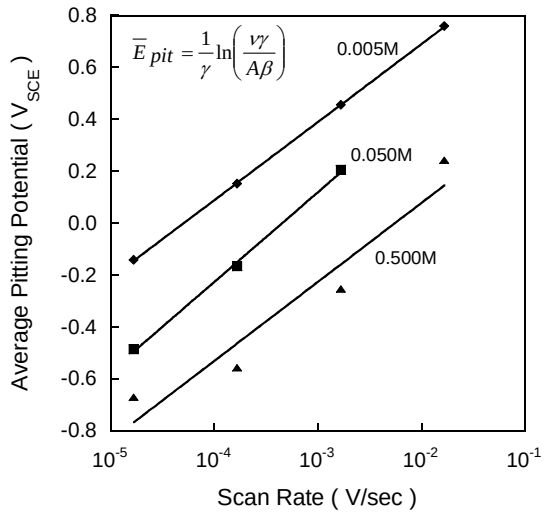

Figure B3.b

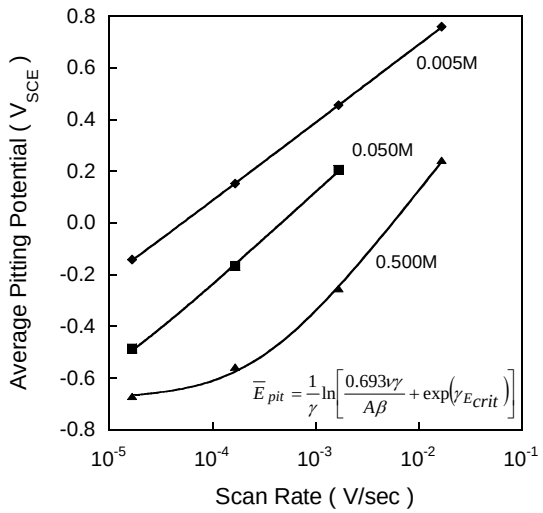

Figure B3.c

Figure B3. Pitting behavior of 125μm diameter 99.99Al electrodes as a function of scan rate and chloride concentration at 25ºC. (a) Fit to Equation B15 (A-1/2 dependence of *Ēpit*), (b) Fit to Equation B18 (log ν dependence of *Ēpit*), (c) Fit to Equation B16 (log ν dependence of *Ēpit* above critical potential, Eo). ◆ 0.005M NaCl, ■ 0.05M NaCl, ▲ 0.5M NaCl.

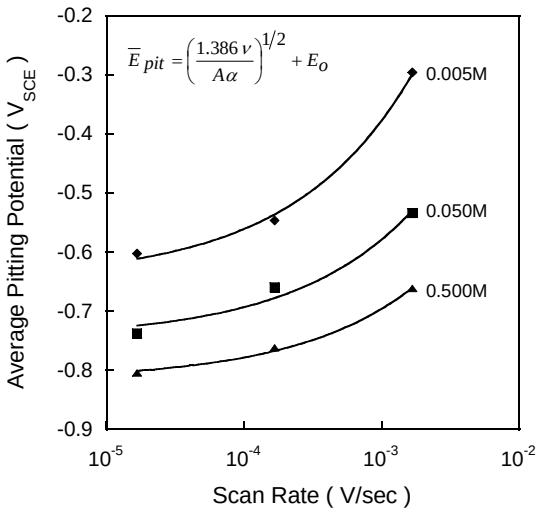

Figure B4.a

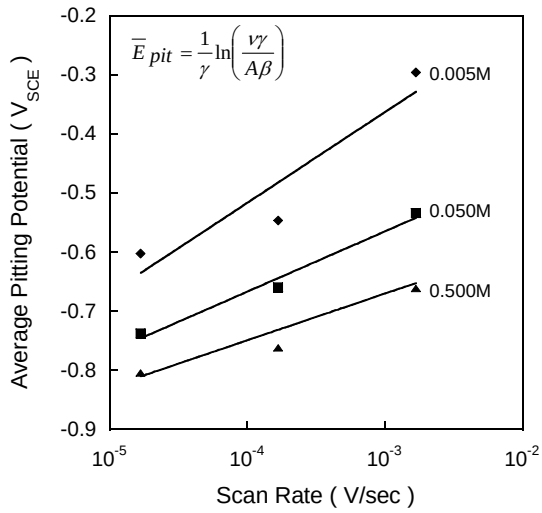

Figure B4.b

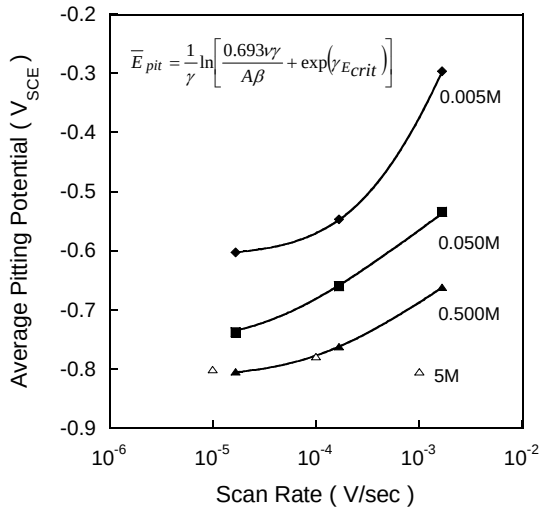

Figure B4.c

Figure B4. Pitting behavior of 500μm diameter 99.99Al electrodes as a function of scan rate and chloride concentration at 25ºC. (a) Fit to Equation B15 (A-1/2 dependence of *Ēpit*), (b) Fit to Equation B18 (log ν dependence of *Ēpit*), (c) Fit to Equation B16 (log ν dependence of *Ēpit* above critical potential, Eo). ◆ 0.005M NaCl, ■ 0.05M NaCl, ▲ 0.5M NaCl, △ 5M NaCl (Figure 4.d, only).

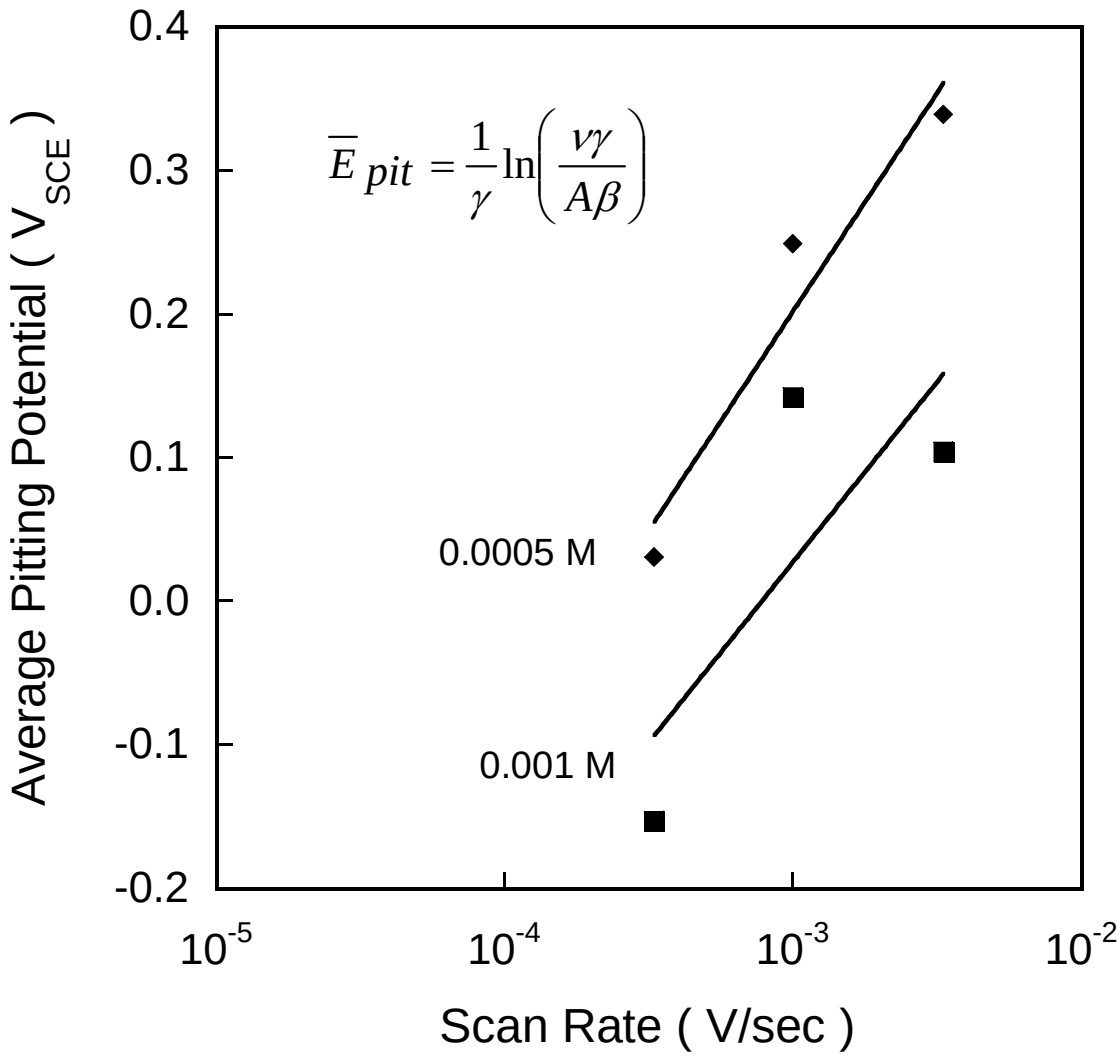

Figure B5. Pitting behavior of 500μm diameter 99.99Al electrodes as a function of scan rate in dilute chloride solutions at 25°C. Data were fit to Equation B18 (log ν dependence of *Ēpit*). ◆ 5e-4M NaCl, ■ 0.001M NaCl.

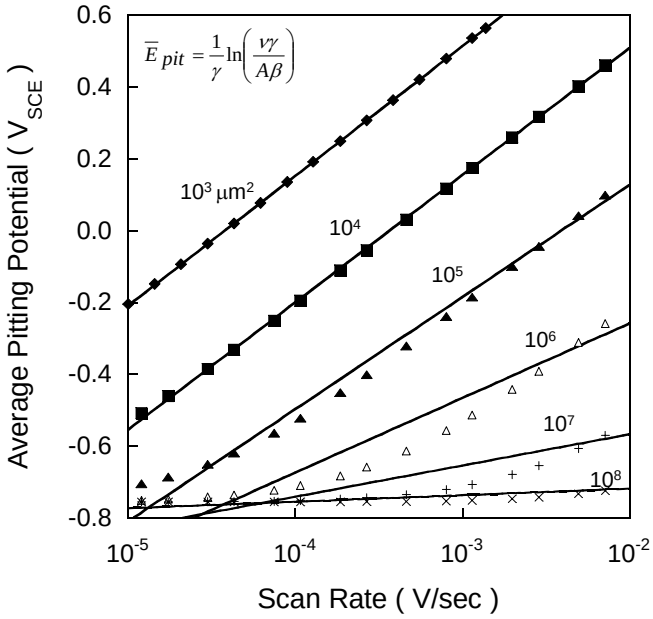

Figure B6.a

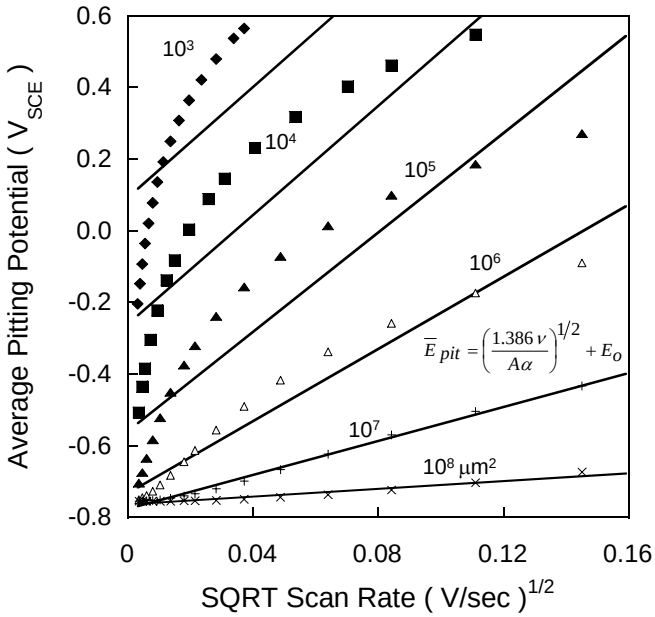

Figure B6.b

Figure B6. Calculated relationships between *Ēpit* and ν for various electrode areas generated using Equation B16 and constants from 125μm wires in 0.05M NaCl (see Table I). (a) *Ēpit* vs. log(ν) with logarithmic fits to data, (b) *Ēpit* vs. ν1/2 with square-root fits to data. Electrode areas in μm2: ◆ 103, ■ 104, ▲ 105, △ 106, + 107, ╳ 108.

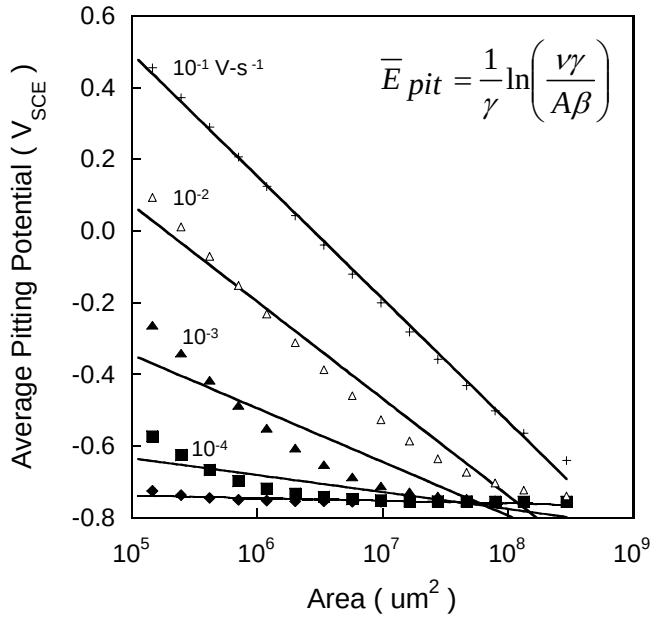

Figure B7.a

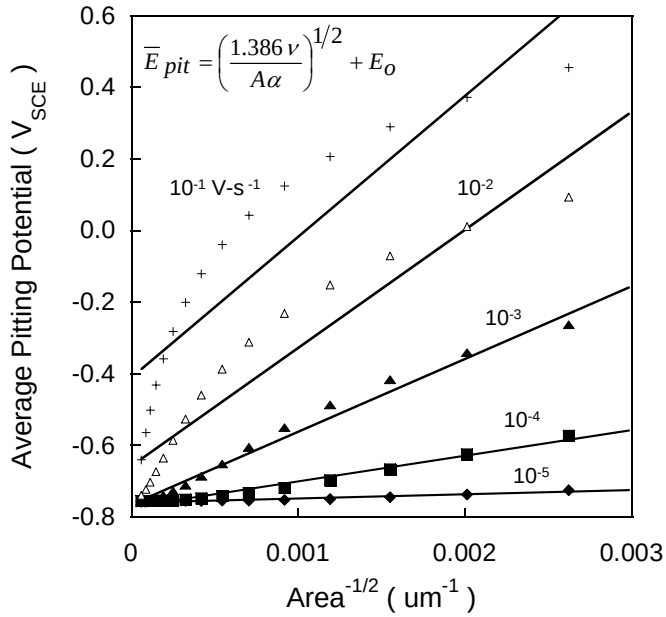

Figure B7.b

Figure B7. Calculated relationships between *Ēpit* and electrode area for various scan rates generated using Equation B16 and constants from 125μm wires in 0.05M NaCl (see Table I). (a) *Ēpit* vs. log(A) with log A-1 fits to data, (b) *Ēpit* vs. A-1/2 with inverse square-root fits to data. Scan rates in V·s-1: ◆ 10-5, ■ 10-4, ▲ 10-3, △ 10-2, + 10-1.

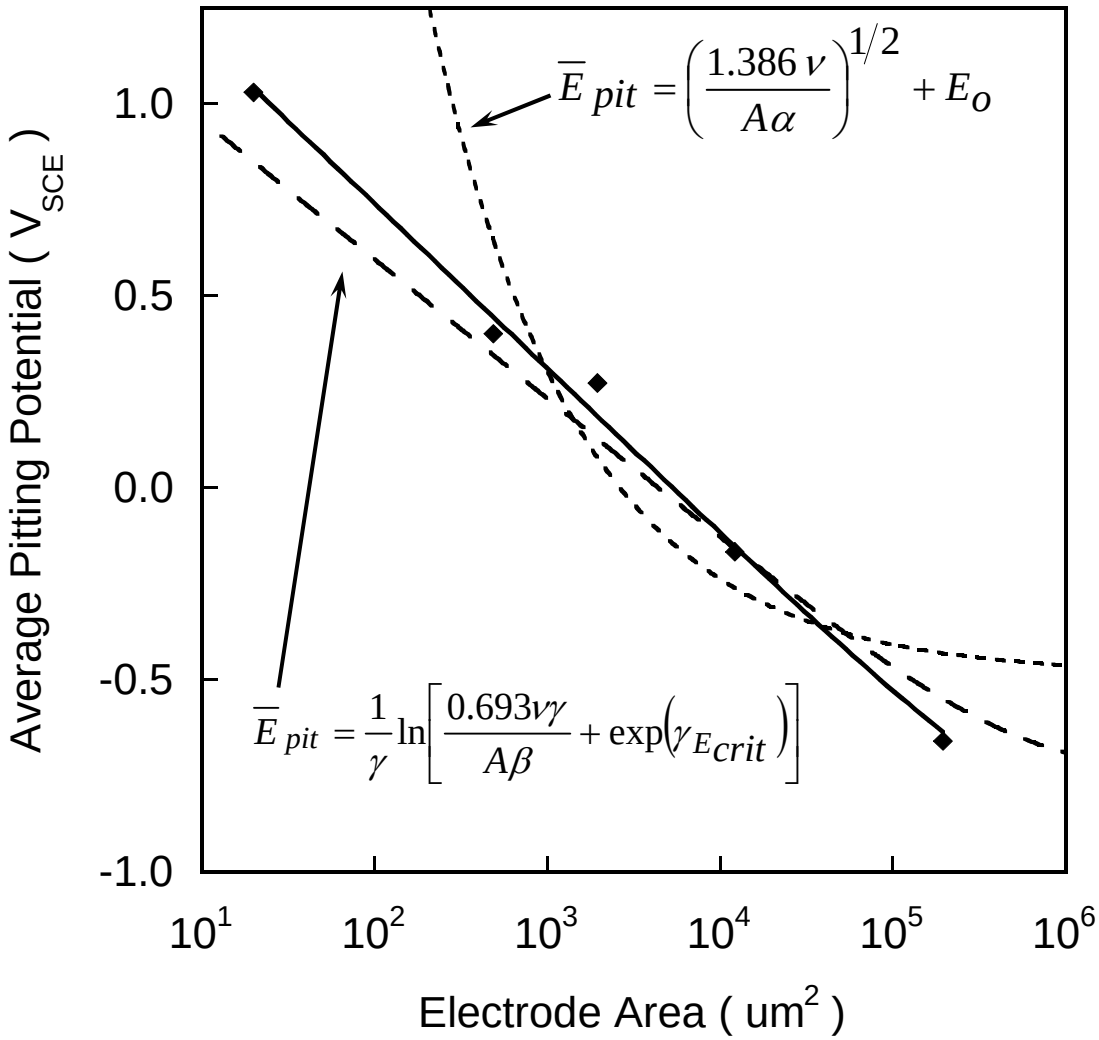

Figure B8. Comparison of observed trend in *Ēpit* vs. area data and predictions using constants from *Ēpit* vs. ν for 125μm wires in 0.05M NaCl (see Table BI). ◆ *Ēpit* vs. A data, ─ fit of Equation B16 to *Ēpit* vs. A data, -- prediction using Equation B16 and constants from 125μm data, ··· prediction using Equation B15 and 125μm data.

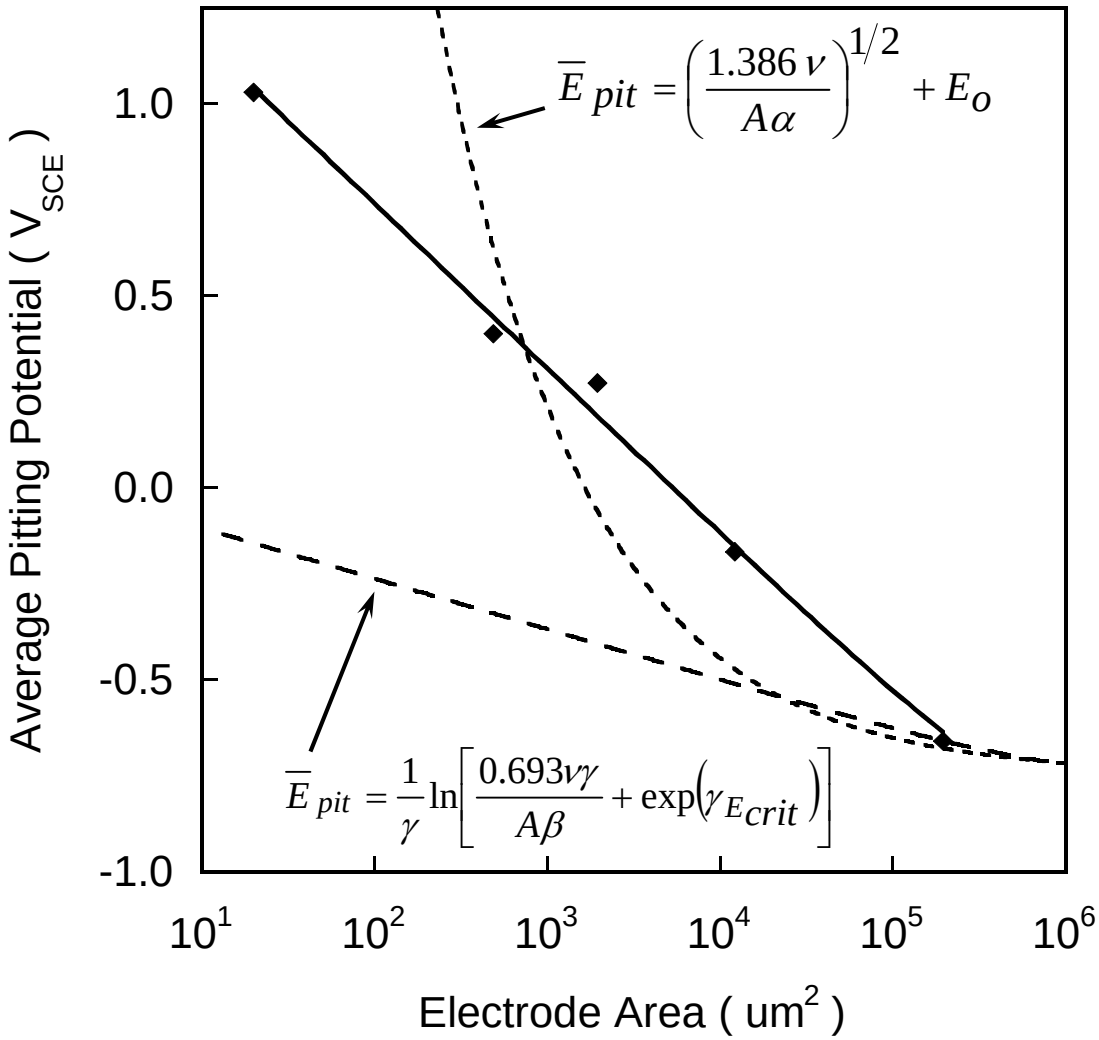

Figure B9. Comparison of observed trend in *Ēpit* vs. area data and predictions using constants from *Ēpit* vs. ν for 500μm wires in 0.05M NaCl (see Table BI). ◆ *Ēpit* vs. A data, ─ fit of Equation B16 to *Ēpit* vs. A data, -- prediction using Equation B16 and constants from 500μm data, ··· prediction using Equation B15 and 500μm data.

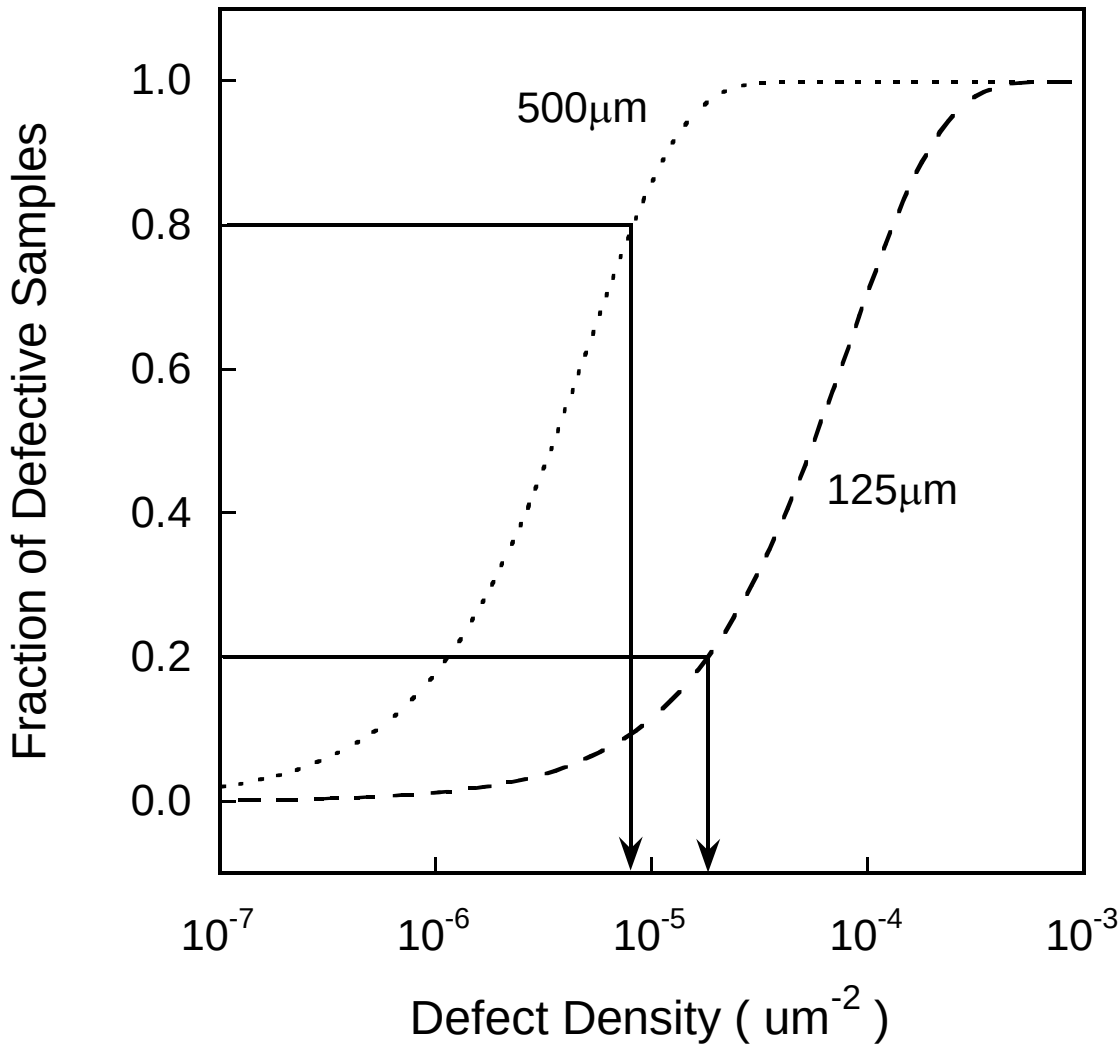

Figure B10. Probability that a sample contains at least one defect as a function of defect density (based on Equation B19), and prediction of a defect density that controls initiation on 500μm electrodes. -- prediction for 125μm electrodes, ··· prediction for 500μm electrodes, ─ bounds on defect densities that can dominate the pitting behavior of 500μm electrodes but not strongly influence 125μm electrodes.

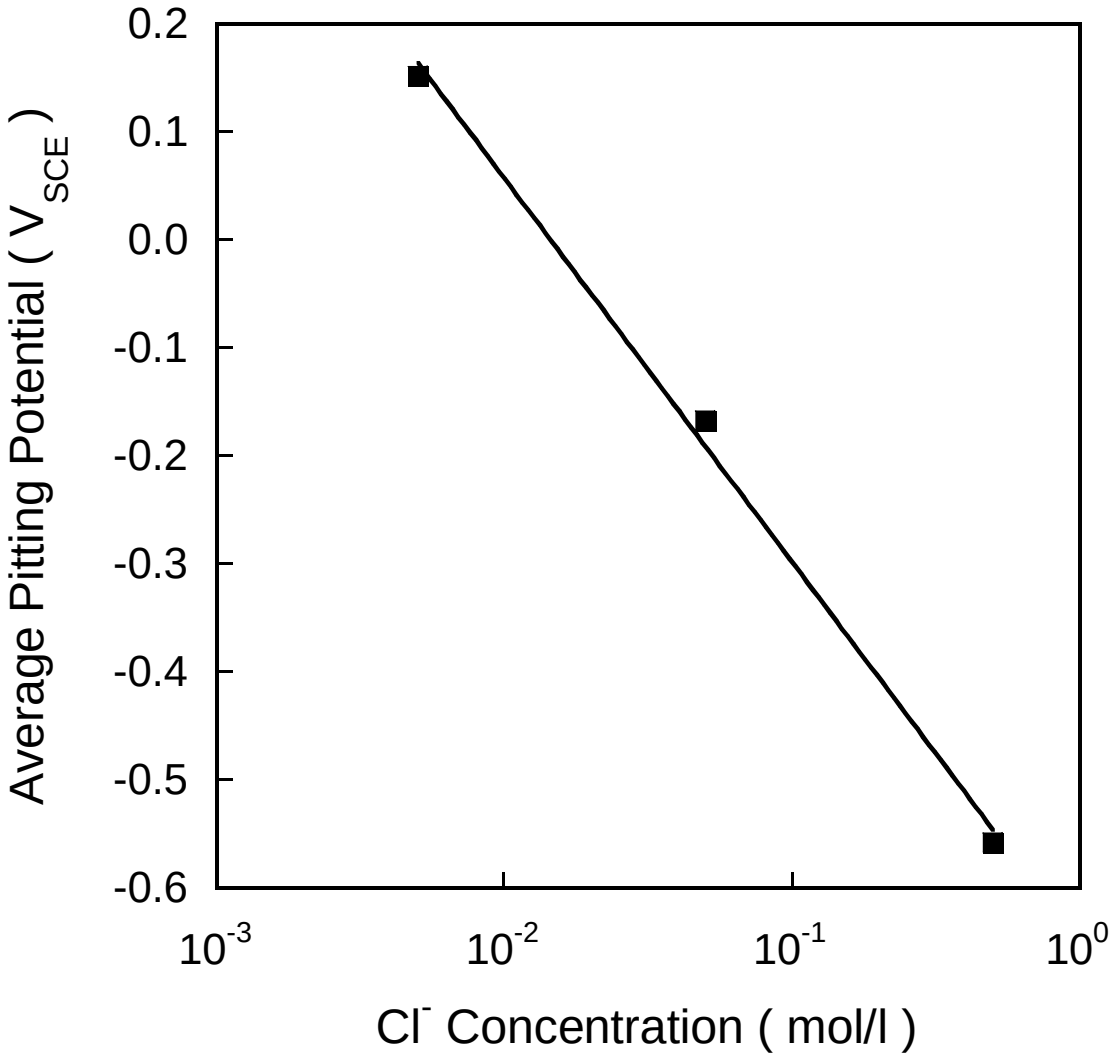

Figure B11. Dependence of *Ēpit* on chloride ion concentration for 125μm electrodes, 25°C, 1,67e-4V·s-1. ■ measured *Ēpit* values, ─ fit to Equation B20.

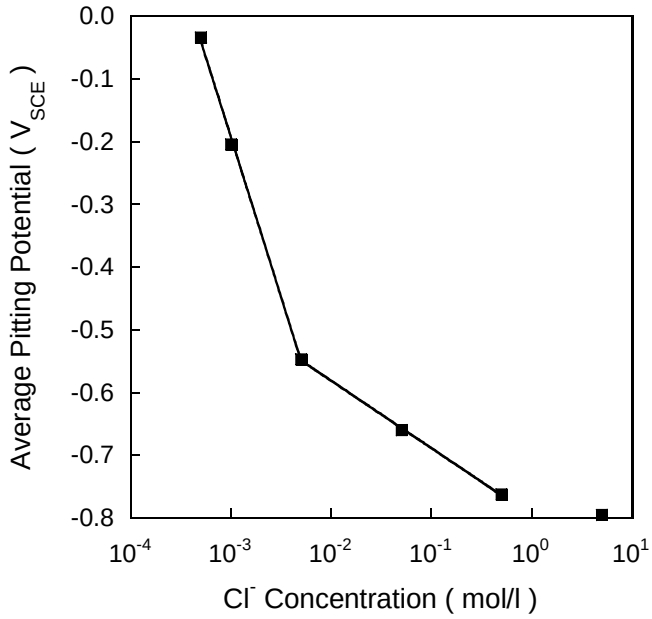

Figure B12.a

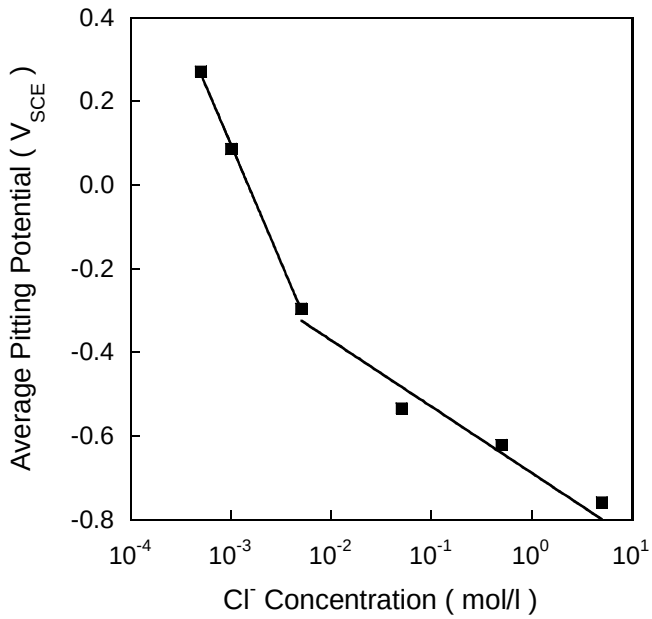

Figure B12.b

Figure B12. Dependence of *Ēpit* on chloride ion concentration for 500μm electrodes, 25°C. (a) ν = 1.67e-4V·s-1, (b) ν = 1.67e-3V·s-1. ■ measured *Ēpit* values, ─ fit to Equation B20.

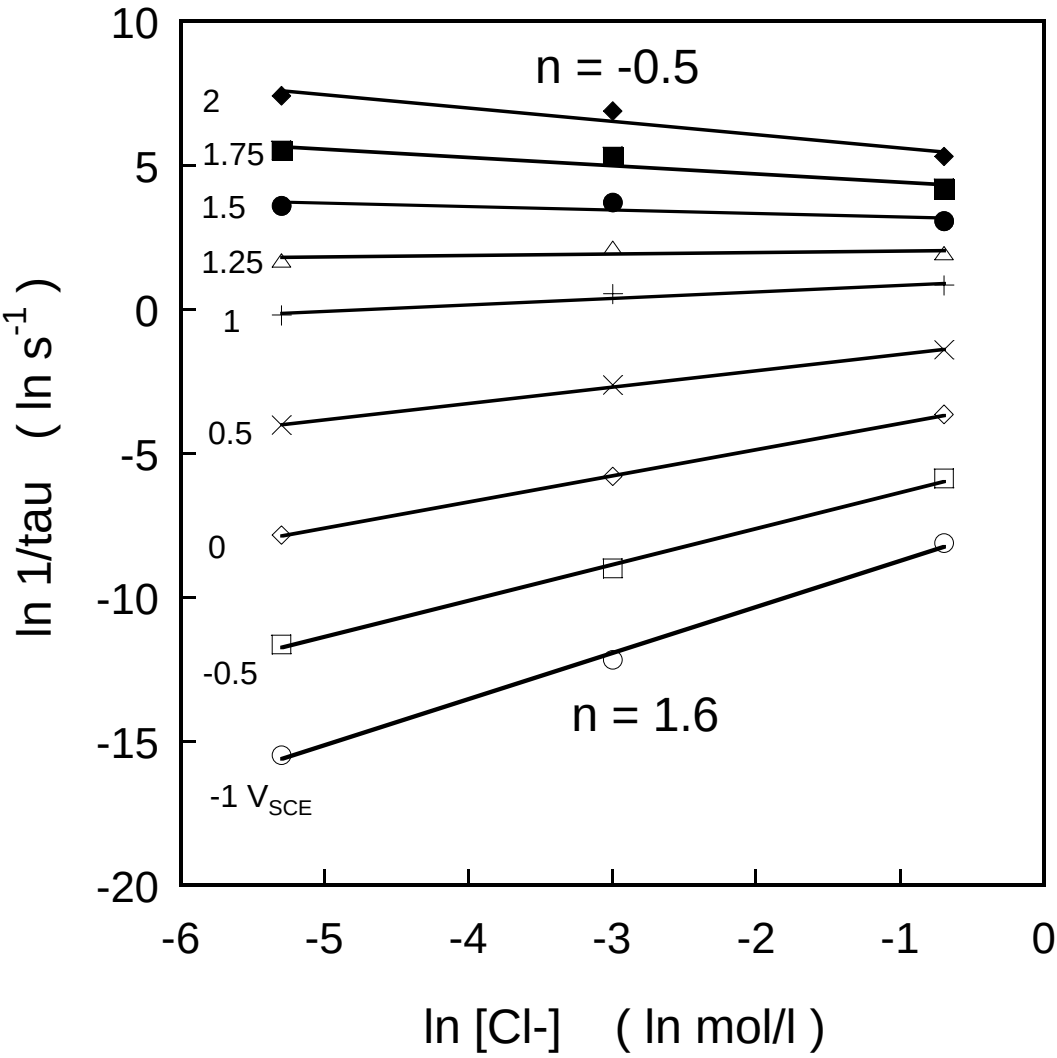

Figure B13. Calculated relationship between τ and chloride concentration for 125μm electrodes (Equation 23). Applied potentials (VSCE): ○ -1, □ -0.5, ◇ 0, ╳ 0.5, ┼ 1, △ 1.25, ● 1.5, ■ 1.75, ◆ 2. ─ fits to equation B22.

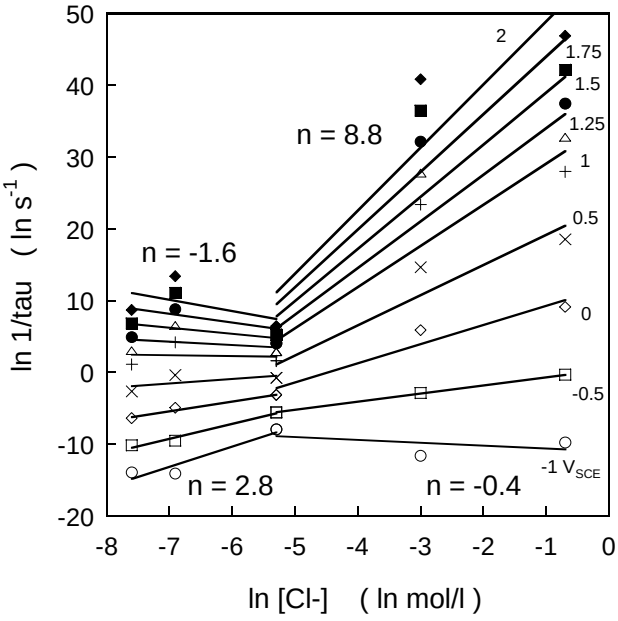

Figure B14.a

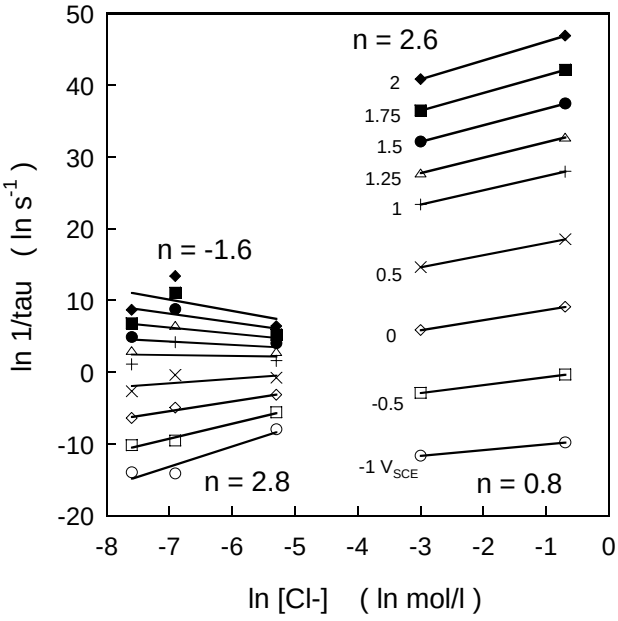

Figure B14.b

Figure B14. Calculated relationship between τ and chloride concentration for 500μm electrodes (Equation B23). (a) Lines drawn through data such that *n* is a function of applied potential for all [Cl-], (b) Lines drawn through data such that *n* is independent of applied potential at high [Cl-]. Applied potentials (VSCE): ○ -1, □ -0.5, ◇ 0, ╳ 0.5, ┼ 1, △ 1.25, ● 1.5, ■ 1.75, ◆ 2. ─ fits to equation B22.

Section C:

The Relationship Between Induction Time for Pitting and Pitting Potential for High Purity Aluminum

Summary

The objective of this study was to determine if a distribution of pit induction times (from potentiostatic experiments) could be used to predict a distribution of pitting potentials (from potentiodynamic experiments) for high purity aluminum. Pit induction times were measured for 99.99 Al in 50 mMol NaCl at potentials of –0.35, -0.3, -0.25 and –0.2 V_{SCE}. Analysis of the data showed that, in general, pit germination rate was an exponential function of the applied potential; however, a subset of the germination rate data appeared to be mostly potential-insensitive. The germination rate behavior was used as an input into a mathematical relationship that provided a prediction of pitting potential distribution. Good general agreement was found between the predicted distribution and an experimentally determined pitting potential distribution, suggesting that the relationships presented here provide a suitable means for quantitatively describing pit germination rate.

C1. Introduction

The objective of this work is to determine if pit induction time data can be used to predict the potentiodynamic pitting data for pure aluminum: i.e., if the experimental conditions are carefully chosen, are induction time (τ) and pitting potential (E_{pit}) data mathematically interdependent? Equilibrium models, such as MacDonald's point defect model(1), would suggest that the two parameters are linked and the scanning of potential in the potentiodynamic case does not alter the mechanism by which pitting occurs. In contrast, experimental evidence exists that suggests a complex influence of scan rate on pitting behavior. For example, Baroux reported that decreasing scan rate could result in an increase in pitting potential for sufficiently slow scan rates(2). In the present work, we have attempted to determine if τ and E_{pit} are relatable for pure aluminum under carefully controlled experimental conditions.

In order to test the link between τ and E_{pit} it is necessary to have a mathematical model that relates these parameters. Recently, we reviewed the derivation of such a model and the details can be found elsewhere(3). Here we will briefly summarize the equations necessary to calculate the pitting potential distribution from parameters that can be extracted from induction time data.

In the mid 1970's Shibata developed a statistical treatment of pit nucleation in stainless steel that expressed both E_{pit} and τ in terms of a germination rate, λ (s^{-1}) (4). More recently, we applied this treatment to the pitting behavior of aluminum and found that λ could best be described by an exponential dependence on potential (3):

$$\lambda(E) = A\beta \exp(\gamma E) \qquad \text{(C1)}$$

where A is the area of the electrode (μm^2), E the potential (V), and β ($\mu m^{-2}s^{-1}$) and γ (V^{-1}) are constants. At a particular potential, λ can be experimentally determined by taking the negative of the slope of log(survival probability) vs. τ:

$$\lambda = -\frac{d\log(P_s)}{d\tau} \qquad \text{(C2)}$$

where P_s is the probability that a sample survives for a given time and is calculated from:

$$P_S(n) = \frac{n}{N+1} \qquad \text{(C3)}$$

where *n* is the n^{th} sample to pit out of a total population of *N* values. Thus a value for λ can be experimentally determined by making N induction time measurements. Performing induction time testing at various *E* will yield λ(E) data that can be fit to Equation C1. The cumulative distribution function (CDF) for E_{pit} can also be expressed in terms of λ(E):

$$CDF(E_{pit}) = P(E_{pit} \le E_2) = 1 - \exp\left\{-\frac{1}{\nu}\int_{E_1}^{E_2}\lambda(E)dE\right\} \qquad \text{(C4)}$$

where ν is scan rate ($V \cdot s^{-1}$), E_1 is the starting potential (V) for the potential scan and E_2 is the potential (V) at which the CDF is being evaluated. Substituting Equation C1 into Equation C4 leads to:

$$CDF(E_{pit}) = P(E_{pit} \le E_2) = 1 - \exp\left\{-\frac{A\beta}{\nu}\left[\exp(\gamma E_2) - \exp(\gamma E_1)\right]\right\} \qquad \text{(C5)}$$

To summarize, if we determine λ(E) by measuring distributions of τ at various potentials (Equations C2 and C3) then a prediction of the pitting potential distribution can be made using Equation C5. We can compare this prediction to an experimentally determined distribution to determine if τ can be used to generate an E_{pit} distribution.

C2. Experimental

C2.1 Materials

The material used in this work was 99.99 Al wire with a diameter of 125 μm. Wires were coated with an electrophoretic paint (PPG part #ED5050B), and then assembled into arrays of 10 wires each in epoxy molds. Following a mechanical polish to 4000 grit SiC, the samples were electropolished in 75% methanol, 20% perchloric acid and 5% glycerol at 0^oC, 10VDC for 120 sec. The details of the electropolish procedure have been previously reported(3). The polished array was etched for 120 s in 50% HNO_3, rinsed in deionized (DI) water, dried in an N_2 gas stream and allowed to sit at ambient conditions for 24 hours before the experiment was started.

C2.2 Electrochemical Testing

Electrochemical testing was performed using a Princeton Applied Research Versatile Multipotentiostat (VMP) to test 10 electrodes simultaneously, enabling a large dataset to be constructed. A saturated calomel reference electrode (SCE) was used as a common reference electrode and a Pt wire was used as a common counter electrode. The SCE was contained in a glass jacket filled with 5 mMol NaCl that terminated in a Vycor™ tip. 1100 ml of test solution was used in each experiment. The test cell was kept in a temperature-controlled bath at 25°C for all experiments.

The protocol for performing the induction-time and potentiodynamic polarization experiments was carefully chosen such that the electrodes underwent a consistent conditioning sequence immediately preceding the experiment. The electrode array was placed in 1000 ml of DI water at open circuit for 1 hour. The potential of the sample was then ramped at 1 $mV \cdot s^{-1}$ to either –0.350 V_{SCE} for potentiodynamic experiments or to a target potential (-0.35, -0.3, -0.25 or -0.2 V_{SCE}) for induction time testing. These potentials were selected based on previous experiments that suggested that the induction times would be easily differentiable under these conditions but not be so long that the experimental matrix would require excessive time to complete. The potential was held constant at the target potential for 1 hour, and then 100 ml of 0.55 M NaCl was added to the solution to yield 1100 ml of 0.05 M NaCl. An air bubbler was used to agitate the solution while the NaCl concentrate was being added. At this point the potential was held constant for induction time testing or ramped anodically at 0.1 $mV \cdot s^{-1}$ for potentiodynamic testing. Each channel was disconnected from the control circuit (e.g., returned to open circuit conditions) when the current for that channel reached 0.5 μA (corresponding to an average current density of 4 $mA \cdot cm^{-2}$). These experimental sequences are shown in Figure C1.

By using the procedure described above, pit nucleation below the potential range of interest is avoided due to the absence of a halogen species. In essence, this protocol pins E_1 in Equations C4 and C5 and enables a comparison to be made between the potential-dependent germination behaviors measured during potentiodynamic and potentiostatic experiments. Although starting the potentiodynamic experiments at E_{OC} would not preclude such a comparison, it would require experimental determination of the E_1 parameter, possibly introducing additional error into the analysis.

C3. Results

The induction time data are plotted in Figure C2.a as log (P_s) vs. τ. Two distinct slopes can be identified in the P_s vs. τ data for each applied potential. An approximately linear region exists for $P_s > 0.3$ (Figure C2.b). A second slope exists for $P_s < 0.1$. The data between $P_s = 0.1$ and $P_s = 0.3$ cannot be sensibly fit to a straight line. A higher density of data points is likely required before the data in this range can be fit to a simple mathematical function. Thus the remainder of this discussion will be based on analysis of data for $P_s > 0.3$ and $P_s < 0.1$, and the assumption is made that these ranges of data are a reasonable representation of pit nucleation rate behavior.

Values for λ were determined using Equation C2 for each potential by fitting a straight line to the log(P_s) vs. τ data over regions where $d\log(P_s)/d\tau$ is constant. Examples of fits to the data for $P_s > 0.3$ are shown in Figure C2.b. Fits were also performed for the data ranges $P_s > 0.8$ and $P_s < 0.1$. The fit to the first 20% of the data

(i.e., $P_s > 0.8$) was performed to determine if there was an additional slope for short τ (this will be discussed further later in this paper).

λ vs. *E* for each of these probability ranges is plotted in Figure C3. These data were fit to Equation C1 in order to generate values for the constants β and γ for each probability range and a summary of the results appears in Table CI.

C4. Discussion

C4.1. Prediction of E_{pit} CDF from Induction Time Testing

A pitting potential CDF was calculated from the data in Table CI by application of Equation C5. The first 90% of the CDF is calculated based on the initial steep slopes of the survival probability data (Figure C2.a); whereas, the last 10% of the CDF is based on the slope calculated for $P_S < 0.1$. This procedure ensures that the two experimentally observed distinct ranges of induction time behavior are captured in the calculated E_{pit} CDF. The results of this calculation along with the experimentally determined CDF are shown in Figure C4. The calculated distribution matches the general shape of the measured distribution and does an adequate job of predicting the 50th percentile pitting potential (-0.222 V_{SCE} predicted vs. –0.244 V_{SCE} measured). There are discrepancies between the two distributions, however, most notably an overestimation of E_{pit} values for $P < 0.5$ and an underestimation for $0.5 < P < 0.9$.

The discrepancy in the range $0.5 < P < 0.9$ may be due to an oversimplified fit of the induction time data. Shibata reported three slopes for Log (P_s) vs. τ for stainless steel with the middle slope being steeper than the other two (4). The scatter in the induction time data determined here for aluminum with $0.3 > P_s > 0.1$ prevents the estimation of an additional slope in this range. It may be possible to improve the prediction with a higher data density for the induction time experiments.

In the beginning portion of the E_{pit} CDF, the predicted E_{pit} values are higher than those measured. Intuitively, it seems that the predicted CDF should show the best agreement for the data near -0.35 V_{SCE}. Because one set of induction time experiments was run at this potential and the potentiodynamic polarization experiments were also started at this potential, the same germination rate should be expressed in both cases. A possible explanation for the discrepancy would be if a subset of the electrode population had significantly different pitting behavior than the average behavior. In previous work, we estimated that approximately 20% of 125 μm diameter Al electrodes tested in a potentiodynamic experiment had pitting behavior that was different from the remaining 80% of the electrodes, possibly due to a sparsely occurring defect (3).

If 20% of the electrodes have a greater pitting susceptibility than the rest of the population, then restricting a fit of the induction time data to $P_S > 0.8$ should lead to improved agreement with experiment. However, from Figure C3 and Table CI it can be seen that restricting the fit to the first 20% of the data does not significantly change the values for β and γ, and, consequently, no significant improvement was observed when the fit was compared to the experimentally determined CDF (comparison not shown).

In contrast to the above results, when the lowest 20% of the experimentally determined pitting potentials are removed from the E_{pit} CDF, very good agreement is seen for $0 < P < 0.5$ and for $0.9 < P < 1$ (Figure C5). Thus, the overestimation of E_{pit} values for $P < 0.5$ may be indicative of a fundamental difference between the pitting processes that occur during potentiostatic vs. potentiodynamic polarization.

When the potential is swept, oxide growth can occur and thus enhance ionic transport in the oxide(5). A consequence of dynamic oxide growth vs. equilibrium conditions may be an increase in the pit germination rate, possibly due to a higher vacancy flux or a greater achievable concentration of Cl^- in the oxide. However, there is no clear agreement in the literature as to a relationship between polarization conditions and chloride content of the oxide. For example, Shimizu(6) and Skeldon(5) observed Cl^- migration in aluminum oxide only under conditions of oxide growth, whereas, Yu and Natishan reported Cl incorporation into the oxide under potentiostatic conditions(7).

A final possibility is that there may be an inherent experimental error in the measurement of the E_{pit} values that manifests itself as a deviation from the prediction from the induction time data. Even taking these errors into consideration, the overall agreement between the induction time data and the pitting potential data is fairly good and suggests that the mathematical model described in this work is appropriate for quantifying the relationship between pit germination behavior and potential.

C4.2. Comparison to Previous Work

It is possible to calculate β and γ by measuring average pitting potential ($\bar{E}_{pit}$) as a function of scan rate, then fitting the data with the following relationship (3):

$$\overline{E}_{pit} = \frac{1}{\gamma}\ln\left[\frac{0.693\nu\gamma}{A\beta} + \exp\left(\gamma_{E_{crit}}\right)\right] \qquad \text{(C6)}$$

where E_{crit} is the potential below which λ = 0 and above which λ is given by Equation 1. The other parameters, ν, γ, *A* and β, were defined in the *Introduction*. In a previous study(3), Equation C6 was used to determine β and γ for the exact same electrode arrays used in this work, using nominally the same mechanical and electropolishing surface preparation. However, in the prior study, polarization testing was performed using a more traditional procedure: the applied potential was ramped anodically from E_{oc} until pitting occurred. The values of β and γ calculated from those variable scan rate experiments were used here to calculate an E_{pit} CDF using the same procedure described above (*Section 4.1*). The tail end of the distribution (P > 0.9) was taken from the induction time data. The calculated CDF appears in Figure C6 along with the measured E_{pit} CDF and the calculated CDF from the induction time data. This relatively good agreement between all three curves lends confidence to the use of the mathematical model for quantifying pit germination behavior. All three curves show essentially the same behavior, although the manner in which the data was collected and/or analyzed in each case was significantly different.

C4.3. Potential Independent Germination Rates

The plot of germination rate versus applied potential (Figure C3) clearly shows an exponential relationship for the first 70% of samples that pit in an induction time experiment. The relationship for the last 10% of samples that pit (i.e., $P_s < 0.1$), however, appears to be strikingly different. For the limited data available for this subset of the sample population, the pit germination rate appears to be either independent of, or, at a minimum, mostly insensitive to the applied potential. This behavior is consistent with the results of the potentiodynamic polarization testing, which showed a tail in the

distribution for the last 10% of the population (Figure C4). There are two candidate theories to account for this bimodal behavior: (1) there exists a specific area density of defects for this material such that 9 out of 10 electrodes sampled will contain such a defect, (2) changes occur in the oxide during polarization that alter the pitting behavior.

The areal density necessary for a specific defect type to be present on 90% of the population of 125 μm diameter electrodes can be calculated using the following relationship:

$$P(defect\ in\ A) = 1 - \exp(-A\chi) \qquad \text{(C7)}$$

where A is the area of the electrode (μm^2) and χ is the areal density of defects (μm^{-2}) corresponding to probability, P, of finding a defect on a given electrode. For P=0.9 and A = 1.2e4 μm^2, χ is calculated to be approximately 1.9e-4 defects·μm^{-2} (or 19000 defects per cm^2). Although such a distributed defect could theoretically account for the bimodal behavior, other evidence suggests that this is not the case. In our previous work, we found that the area-corrected germination rate on smaller electrodes (e.g., 1.9e3, 4.9e2 and 19 μm^2) was approximately the same as the first 70% of the population studied here, rather than the last 10% of the population(3). If the defect density on the aluminum electrodes is 1.9e-4 μm^{-2}, as calculated here, then the probability of finding such a defect on the smaller electrodes would be 0.3, 0.09 and 0.004 respectively. Clearly, these probabilities are inconsistent with the same defect structure determining the average pitting behavior for all of these electrode areas.

The alternative hypothesis is that the several competing processes, of which pitting is one, are occurring as a function of time on the electrode surface. If the oxide has not undergone significant modification (e.g., growth, ion incorporation, hydroxylation, etc.), then the pit germination rate is an exponential function of applied potential. On the other hand, if the sample does not pit before some critical oxide modification has occurred, then the pit germination behavior becomes dependant on the properties of the new system. At this time, the specific nature of the modification that results in a shift in behavior has not been determined. A mechanism such as this can also help to explain the difficulty with measuring the induction time data for $0.3 > P_s > 0.1$. If the time for oxide modification (under a specific condition) is a distributed parameter, then the surface area fraction of the sample that follows the pre- and post-modification behavior will be a function of the time of exposure and the applied potential. This transition period will impose significant error on the apparent germination rate because the data are normalized to the total sample area whereas the actual participating area can range from 0 to 100% of the sample area.

C5. Summary and Conclusions

1. The mathematical relationships used in this work to link E_{pit} and τ (Equations C1-C3) is in reasonably good agreement with experimental data, suggesting that these relationships provide a means of quantifying and parameterizing germination rate that is generically applicable to a variety of experimental conditions.

2. Differences between a predicted E_{pit} distribution (from induction time data) and a measured distribution (from potentiodynamic polarization testing) suggest that pit germination rate may be influenced (i.e., accelerated) by the dynamic potential scanning as opposed to a static potential hold.
3. The results of this study indicate that the pitting behavior of the aluminum-aluminum oxide system is not only a function of the applied potential but is dependent on the time-potential history of the sample.
4. Induction time testing suggests that once a sample survives past some critical period of time, possibly corresponding to a critical modification of the oxide, the germination rate may become independent of applied potential. This result is qualified to the present data set.

C6. References

1. D.D. Macdonald, Journal of the Electrochemical Society, **144**, 5, 1574-1581 (1997).
2. B. Baroux, Corrosion Science, **28**, 10, 969-986 (1988).
3. F.D. Wall and M.A. Martinez, Journal of the Electrochemical Society, **150**, 4, B146-B157 (2003).
4. T. Shibata and T. Takeyama, Corrosion, **33**, 7, 243-251 (1977).
5. M. Skeldon, K. Shimizu, P. Skeldon, G. E. Thompson, G. C. Wood, Corrosion Science, **37**, 9, 1473-1488 (1995).
6. K. Shimizu, G. M. Brown, K. Kobayashi, P. Skeldon, G. E. Thompson, G. C. Wood, Corrosion Science, **41**, 1835-1847 (1999).
7. S.Y. Yu, W. E. O'Grady, D. E. Ramaker, P. M. Natishan, J. Electrochemical Society, **147**, 8, 2952-2958 (2000).

$\lambda(E) = A\beta\exp(\gamma E)$		
Survival Probability Range	β ($s^{-1}\cdot\mu m^{-2}$)	γ (V^{-1})
$P_s > 0.8$	1.9×10^{-6}	12.269
$P_s > 0.3$	9.4×10^{-7}	10.713
$P_s < 0.1$	7.4×10^{-10}	0

Table CI. Constants from the fit of Equation C1 to the data in Figure C3.

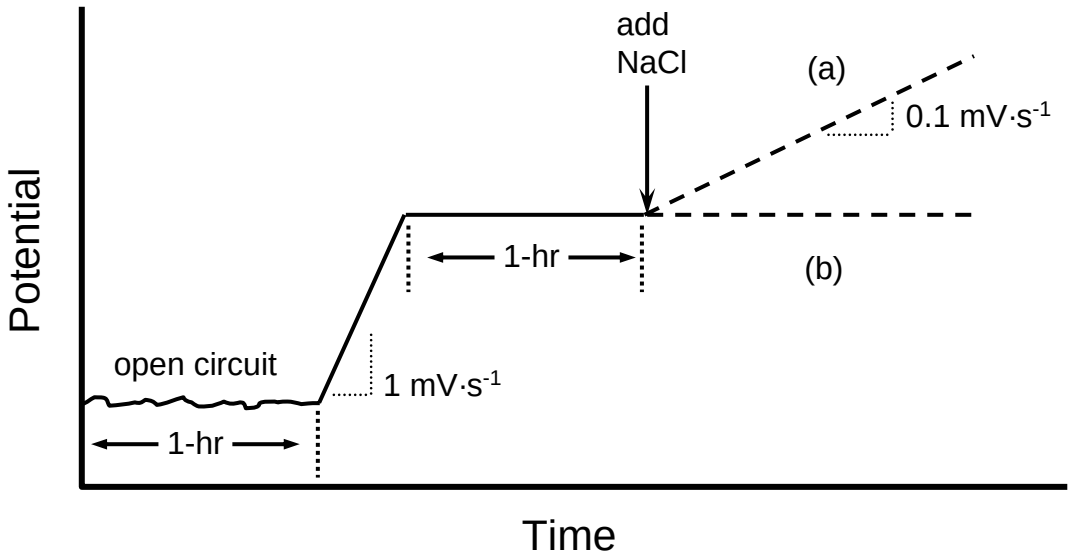

Fig. C1. Potential-time profile for potentiodynamic polarization testing (curve *a*) and induction time testing (curve *b*).

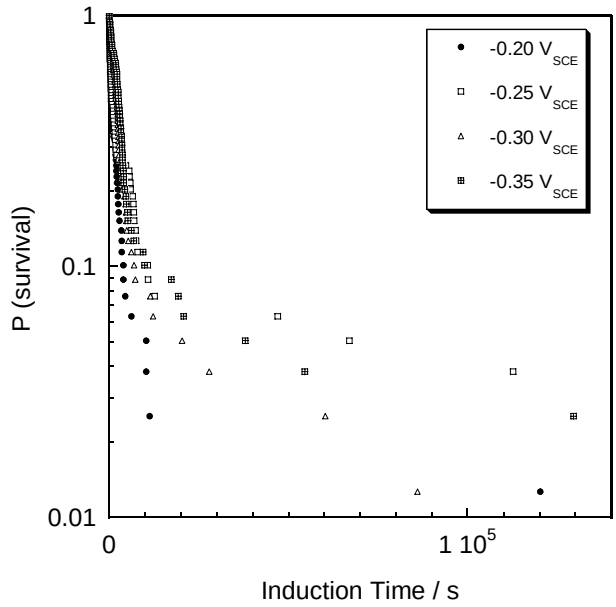

Figure C2.a

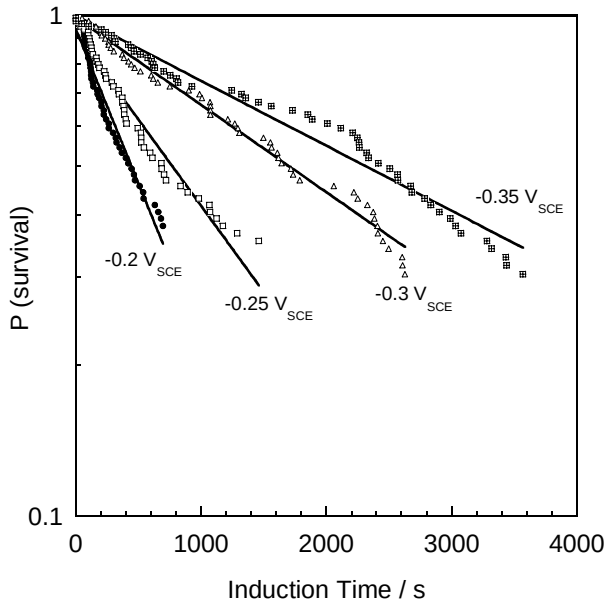

Figure C2.b

Fig. C2. Survival probability vs. induction time (τ) for 99.99 Al immersed in 50-mMol NaCl. (a) all data, (b) first 70% of population (Ps > 0.3) with fits to Equation C2. ● -0.2VSCE, □ –0.25VSCE, △ –0.3VSCE, ⊞ -0.35VSCE.

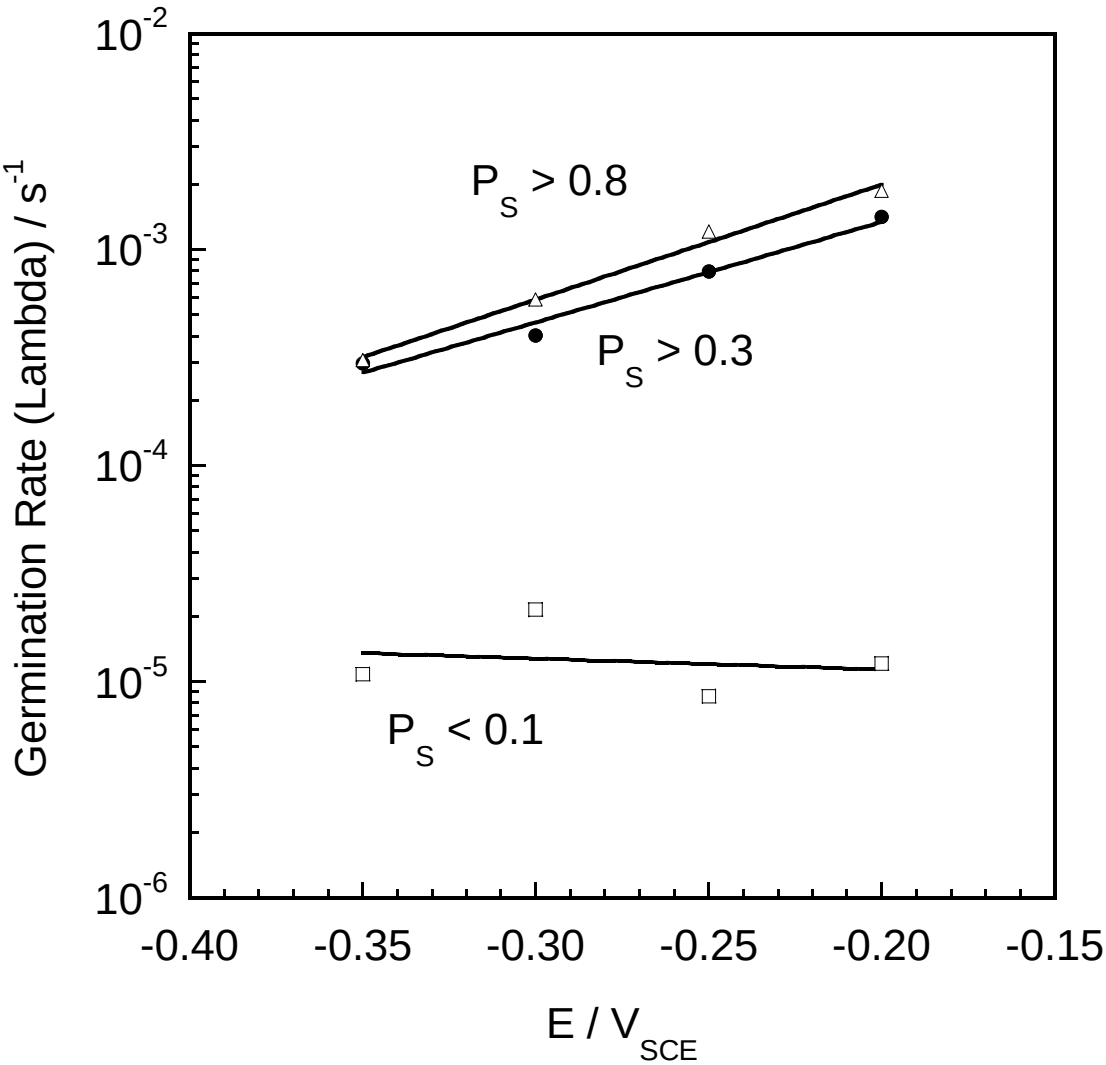

Fig C3. Germination rate (λ) as a function of applied potential (values taken from fits of Equation 2 to data in Figure C2). Lines correspond to fits of Equation 1 to the data (values for constants are tabulated in Table CI). △ Ps > 0.8, ● Ps > 0.3, □ Ps < 0.1.

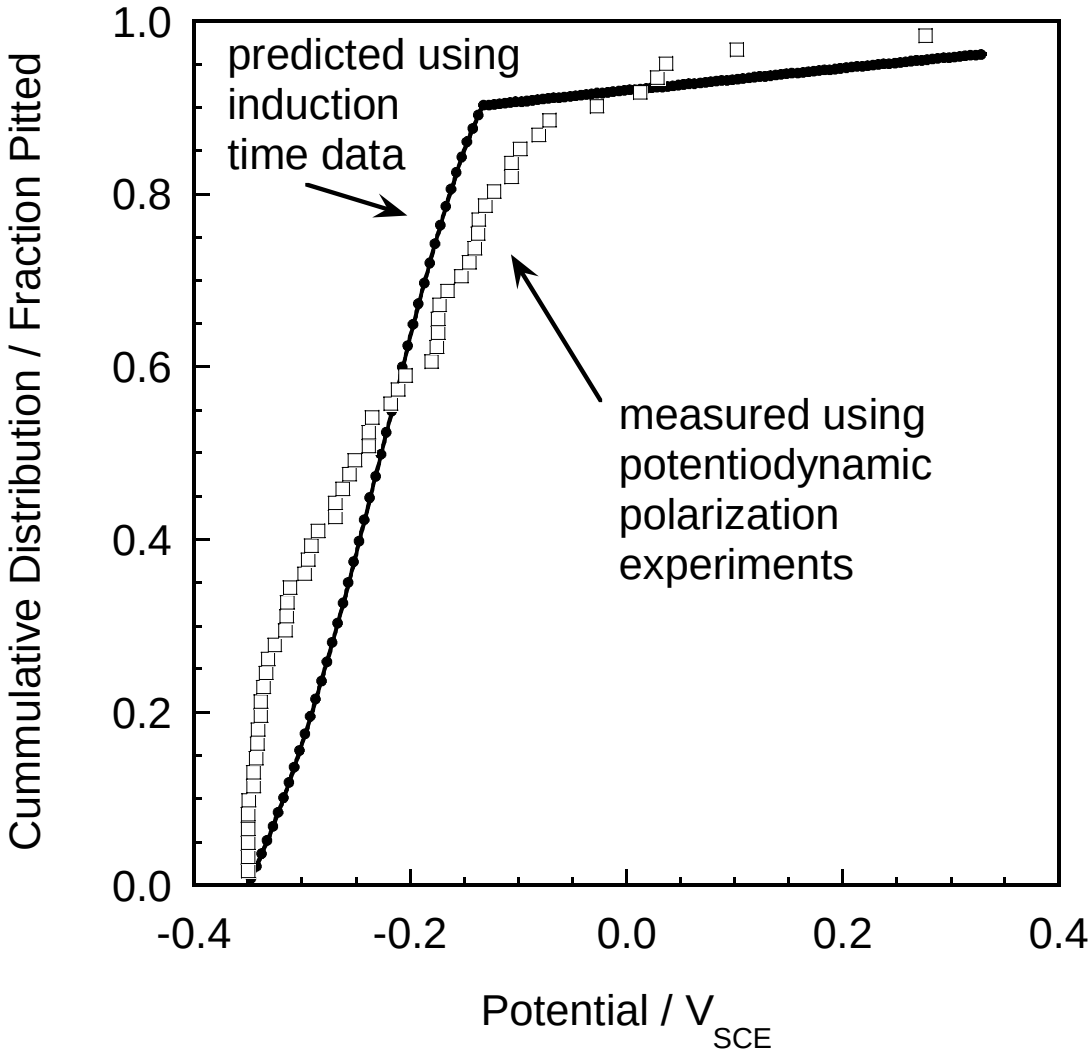

Fig C4. Comparison of predicted (Equation C5) and measured Epit distributions.

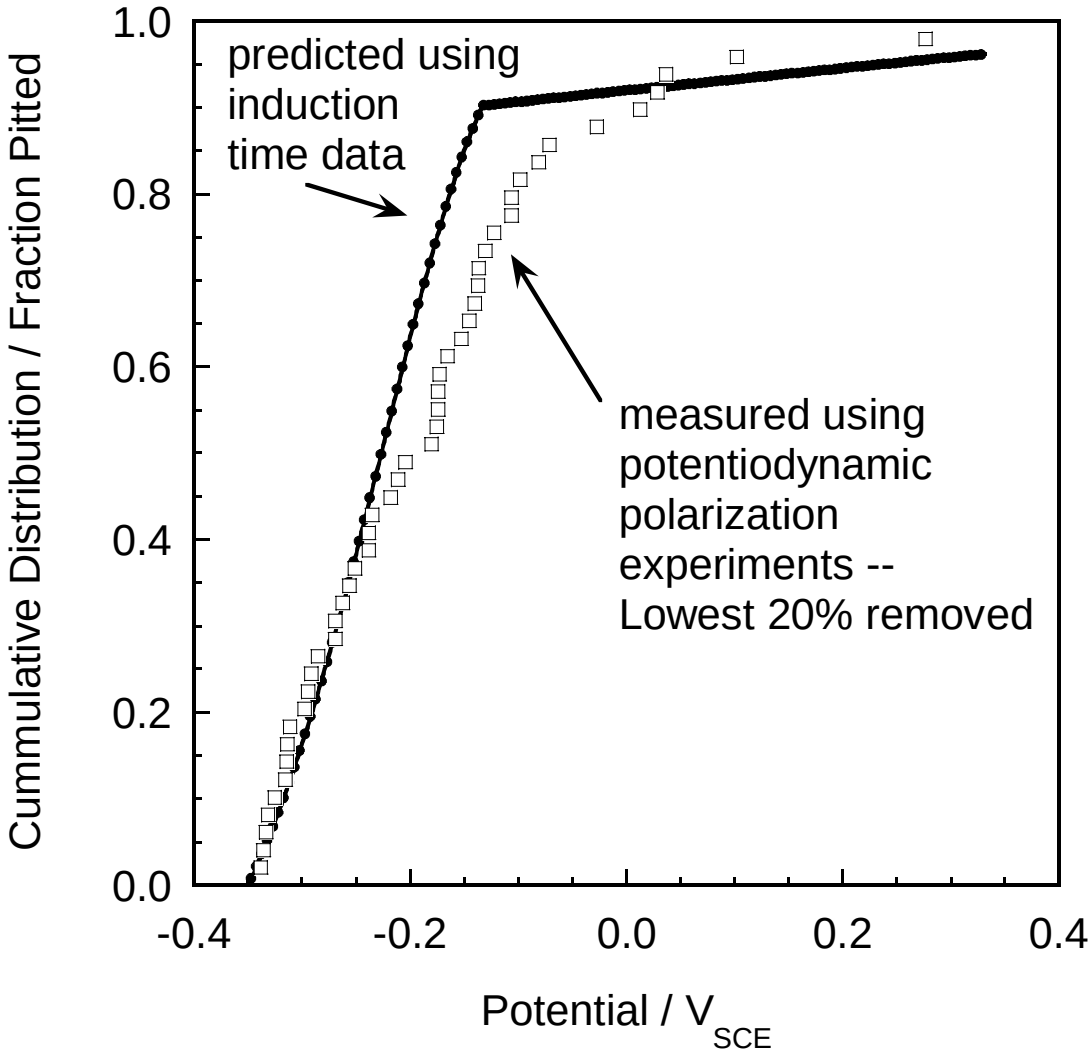

Fig C5. Comparison of predicted Epit distribution to the experimental distribution with the lowest 20% of the pitting potentials removed from the experimental distribution.

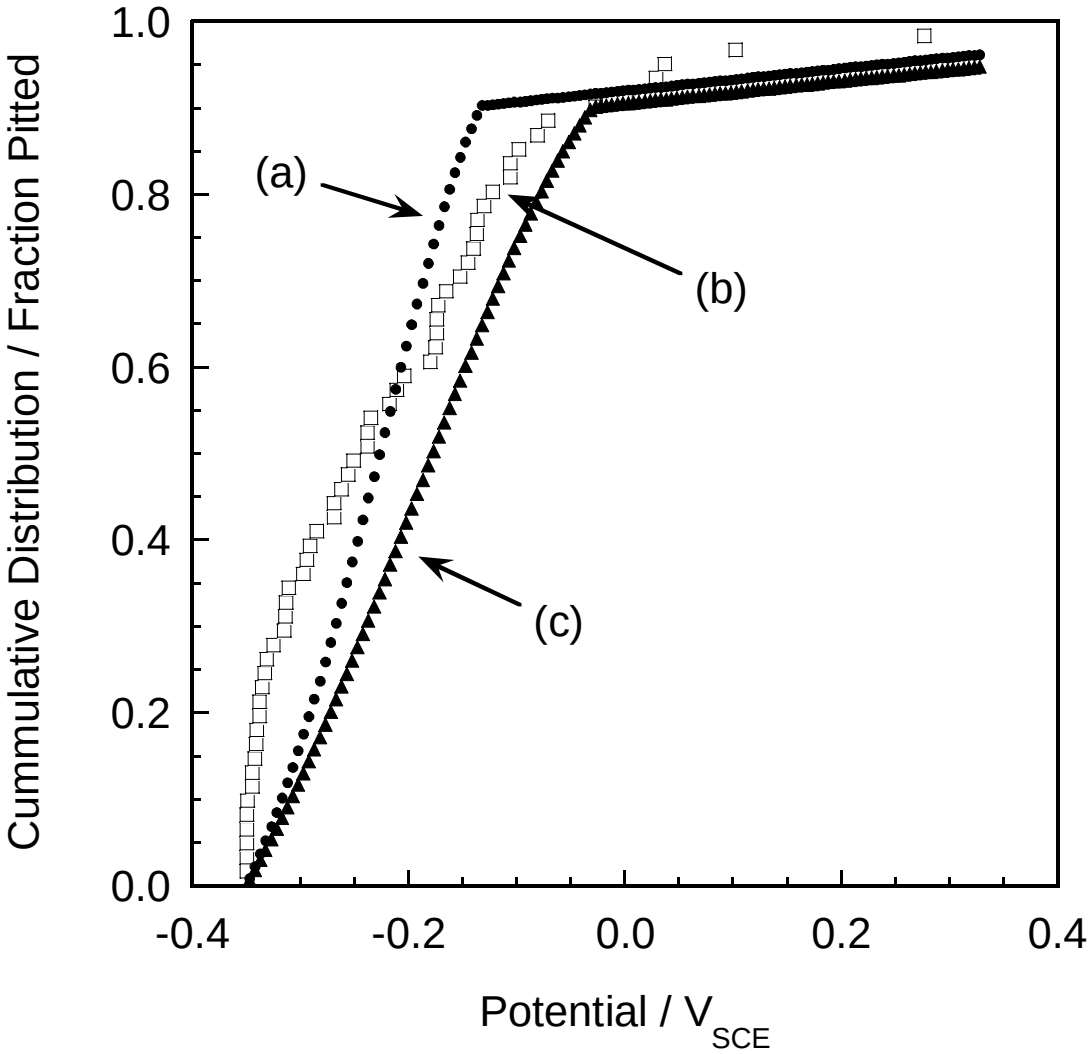

Fig C6. Comparison of (a) the measured Epit distribution, (b) the distribution calculated from analysis of the induction time data and (c) the distribution calculated from measuring the relationship between average pitting potential and scan rate(3).

Distribution

4	MS0888	Kevin R. Zavadil	1832
4	MS0888	Frederick D. Wall	1832
1	MS9018	Central Technical Library	8945-1
2	MS0899	Technical Library	9616
1	MS0188	D. Chavez, LDRD Office	1030